

Thèse

Présentée devant

L'Institut National des Sciences Appliquées de Lyon

Ecole doctoral

MECANIQUE – ENERGETIQUE – GENIE CIVIL – ACOUSTIQUE (MEGA)

Spécialité: MECANIQUE

Pour obtenir

Le grade de docteur

Par

DUAN FANGFANG

NUMERICAL TRIBOLOGY OF THE WHEEL-RAIL CONTACT:
APPLICATION TO CORRUGATION DEFECT

Soutenue le 09 Mars 2015 devant la commission d'examen composée de MM.

BERTHIER Yves	Directeur de Recherche CNRS, LaMCoS, INSA, Lyon
SAULOT Aurélien	Maitre de Conférences HDR, LaMCoS, INSA, Lyon
POZZOLINI Cédric	Dr, Institut Notre Dame des Minimes, Lyon
DENAPE Jean	Professeur, Ecole Nationale d'Ingénieurs, Tarbes
ELEOD Andras	Professeur, Université Technique Budapest, Hongrie
DUFRENOY Philippe	Professeur, Laboratoire de Mécanique de Lille, Lille
QUOST Xavier	Dr, RATP, Paris

INSA Direction de la Recherche - Ecoles Doctorales – Quinquennal 2011-2015

SIGLE	ECOLE DOCTORALE	NOM ET COORDONNEES DU RESPONSABLE
CHIMIE	<p align="center">CHIMIE DE LYON http://www.edchimie-lyon.fr Sec : Renée EL MELHEM Bat Blaise Pascal 3^e etage 04 72 43 80 46 Insa : R. GOURDON secretariat@edchimie-lyon.fr</p>	<p align="center">M. Jean Marc LANCELIN Université de Lyon – Collège Doctoral Bât ESCPE 43 bd du 11 novembre 1918 69622 VILLEURBANNE Cedex Tél : 04.72.43 13 95 directeur@edchimie-lyon.fr</p>
E.E.A.	<p align="center">ELECTRONIQUE, ELECTROTECHNIQUE, AUTOMATIQUE http://edeea.ec-lyon.fr Sec : M.C. HAVGOUDOUKIAN eea@ec-lyon.fr</p>	<p align="center">M. Gérard SCORLETTI Ecole Centrale de Lyon 36 avenue Guy de Collongue 69134 ECULLY Tél : 04.72.18 60.97 Fax : 04 78 43 37 17 Gerard.scorletti@ec-lyon.fr</p>
E2M2	<p align="center">EVOLUTION, ECOSYSTEME, MICROBIOLOGIE, MODELISATION http://e2m2.universite-lyon.fr Sec : Safia AIT CHALAL Bat Atrium- UCB Lyon 1 04.72.44.83.62 Insa : S. REVERCHON Safia.ait-chalal@univ-lyon1.fr</p>	<p align="center">Mme Gudrun BORNETTE CNRS UMR 5023 LEHNA Université Claude Bernard Lyon 1 Bât Forel 43 bd du 11 novembre 1918 69622 VILLEURBANNE Cédex Tél : 06.07.53.89.13 e2m2@univ-lyon1.fr</p>
EDISS	<p align="center">INTERDISCIPLINAIRE SCIENCES-SANTE http://www.ediss-lyon.fr Sec : Safia AIT CHALAL Bat Atrium – UCB Lyon 1 04 72 44 83 62 Insa : Safia.ait-chalal@univ-lyon1.fr</p>	<p align="center">Mme Emmanuelle CANET-SOULAS INSERM U1060, CarMeN lab, Univ. Lyon 1 Bâtiment IMBL 11 avenue Jean Capelle INSA de Lyon 696621 Villeurbanne Tél : 04.72.68.49.09 Fax :04 72 68 49 16 Emmanuelle.canet@univ-lyon1.fr</p>
INFOMATHS	<p align="center">INFORMATIQUE ET MATHÉMATIQUES http://infomaths.univ-lyon1.fr Sec :Renée EL MELHEM Bat Blaise Pascal 3^e etage infomaths@univ-lyon1.fr</p>	<p align="center">Mme Sylvie CALABRETTO LIRIS – INSA de Lyon Bat Blaise Pascal 7 avenue Jean Capelle 69622 VILLEURBANNE Cedex Tél : 04.72. 43. 80. 46 Fax 04 72 43 16 87 Sylvie.calabretto@insa-lyon.fr</p>
Matériaux	<p align="center">MATERIAUX DE LYON http://ed34.universite-lyon.fr Sec : M. LABOUNE PM : 71.70 –Fax : 87.12 Bat. Saint Exupéry Ed.materiaux@insa-lyon.fr</p>	<p align="center">M. Jean-Yves BUFFIERE INSA de Lyon MATEIS Bâtiment Saint Exupéry 7 avenue Jean Capelle 69621 VILLEURBANNE Cedex Tél : 04.72.43 71.70 Fax 04 72 43 85 28 Ed.materiaux@insa-lyon.fr</p>
MEGA	<p align="center">MECANIQUE, ENERGETIQUE, GENIE CIVIL, ACOUSTIQUE http://edmega.universite-lyon.fr/ Sec : M. LABOUNE PM : 71.70 –Fax : 87.12 Bat. Saint Exupéry mega@insa-lyon.fr</p>	<p align="center">M. Philippe BOISSE INSA de Lyon Laboratoire LAMCOS Bâtiment Jacquard 25 bis avenue Jean Capelle 69621 VILLEURBANNE Cedex Tél : 04.72 .43.71.70 Fax : 04 72 43 72 37 Philippe.boisse@insa-lyon.fr</p>
ScSo	<p align="center">ScSo* http://recherche.univ-lyon2.fr/scso/ Sec : Viviane POLSINELLI Brigitte DUBOIS Insa : J.Y. TOUSSAINT viviane.polsinelli@univ-lyon2.fr</p>	<p align="center">Mme Isabelle VON BUELTZINGLOEWEN Université Lyon 2 86 rue Pasteur 69365 LYON Cedex 07 Tél : 04.78.77.23.86 Fax : 04.37.28.04.48 isavonb@gmail.com</p>

To my parents

To my friends

Contents

INTRODUCTION	5
PART 1 INTRODUCTION OF CORRUGATION IN RAILWAY NETWORKS	11
Chapter 1. State of the art.....	13
1.1 Introduction	13
1.2 Review on corrugation study	15
1.2.1 Previous research from origin to the 1990s.....	15
1.2.2 Classical classification of rail corrugation by Grassie and Kalousek.....	17
1.2.3 Description of corrugation defects: Short-pitch corrugation	21
1.2.3.1 Observation of superficial morphology	21
1.2.3.2 Observation of subsurface microstructure.....	23
1.3 The wheel-rail contact theory	26
1.3.1 Normal contact theory - Hertzian theory.....	26
1.3.2 Tangent contact theory - Traction, Friction, and Adhesion	29
1.3.2.1 Rolling/sliding wheel-rail contact model.....	29
1.3.2.2 The quasi-static model of wheel-rail contact with friction.....	30
1.3.2.3 Stick-Slip mechanism in corrugation defect.....	34
1.4 Numerical method applied to analyse corrugation defect.....	35
1.5 Conclusion	37
Chapter 2. Numerical modelling of wheel–rail contact dynamics.....	39
2.1 Numerical model chosen to study the wheel-rail dynamic problem: the mechanical scale	39
2.2 Description of the model	42
2.2.1 A simplified wheel-rail dynamic contact model.....	42
2.2.2 Strategy applied to constitute the wheel-rail dynamic contact model	44
2.2.3 Simulation protocol and parameters	45
2.3 Numerical tools to study the local wheel-rail contact dynamics: the indication of convergence	47
2.3.1 Definition of the contact force and the frictional power	47

2.3.2 Definition of the contact status	48
2.4 Convergence tendency of numerical model	49
2.5 Conclusion	51

PART 2 INVESTIGATION ON THE ORIGIN AND THE EVOLUTION OF STRAIGHT-TRACK CORRUGATION UNDER TRANSIENT CONDITIONS.....53

Chapter 3. Parametric sensibility of corrugation birth under transient conditions with single wheel passing..... 55

3.1 Characterization of the instability states under transient conditions.....	55
3.1.1 Characterization of the contact status.....	55
3.1.2 Characterization of the frequency in modal analysis	56
3.1.3 Characterization of the wheel-rail local contact dynamics.....	58
3.1.4 Characterization of the plastic flow in the birth of corrugation defect.....	59
3.2 Consequence of corrugation with different parameters applied under transient conditions	61
3.2.1 Influence of different slip ratios Γ	62
3.2.2 Influence of different Coulomb's friction coefficients μ	65
3.2.3 Influence of different times Δt to apply transient conditions	67
3.2.4 Conclusion about the study of transient conditions parameters.....	70
3.3 Consequence of corrugation under different material laws	71
3.3.1 Influence of different values of elastic limit	72
3.3.2 Influence of different values of strength index.....	76
3.4 Consequence of corrugation under different mechanical factors	80
3.5 Conclusion	84

Chapter 4. Parametric sensibility of corrugation evolution under transient conditions with multiple wheel passings and geometric defect influence (welded rail) 87

4.1 Evolution of corrugation defect under multiple wheel passings	87
4.1.1 Multiple wheel passings without slip	88
4.1.2 Multiple wheel passings with slip	91
4.1.3 Discussion of the results.....	95
4.2 Evolution of corrugation defect under wheel passing on the jointed rail area	96
4.2.1 Birth of corrugation defect under influence of the welded rail joint irregularity.....	98

4.2.1.1 Model without considering the mechanical factors.....	98
4.2.1.2 Model with considering the mechanical factors	99
4.2.2 Evolution of corrugation defect under influence of the axle loads.....	102
4.2.3 Evolution of corrugation defect under the rail joints between two sleepers	105
4.3 Conclusion	108

PART 3 IMPROVEMENT OF THE 2D DYNAMIC FEM MODEL TO REPRODUCE THE CORRUGATION DEFECTS REALISTICALLY

Chapter 5. Problem of the 2D dynamic FEM model and a suggested solution

5.1 Numerical dissipation problem	113
5.2 Introduction of Mass Redistribution Method	115
5.3 Mass Redistribution Method (MRM) applied to 2D wheel-rail contact model	117
5.3.1 Convergence tendency of the model with MRM	117
5.3.2 Local results obtained with both OM and MRM	119
5.3.3 Global results obtained with both OM and MRM.....	120
5.4 Additional wheel passings with slip in Mass redistribution model	122
5.5 Conclusion	124

CONCLUSION AND FUTURE WORK.....

125

REFERENCES.....

131

APPENDIX

143

Introduction

In urban networks, straight-track corrugation is exposed as one of the most serious defects appearing in wheel-rail contact, and affects the rail-way operation and maintenance. Straight-track corrugation is a periodical defect of rail surface that occurs while wheel-rail contact undergoes transient conditions such as braking or acceleration. Train rolling on such defect, will induce structural vibrations as well as rolling noise, and expensive cost for the maintenance.

According to the bibliographies, it is important to highlight that corrugation is not a single phenomenon with a unique cause and a unique solution or treatment. In order to find out a more detailed observation of corrugation and to understand the important factors which affect corrugation growth, some extensive and well documented surveys have been described since the end of 19th century. Many site tests were made and many surveys were conducted with a great variety of steel types, rail profiles, exploitation conditions, etc...[1] [2] [14]. In 1993, Grassie and Kalousek [3] presented a classification of corrugation with their characteristics, causes and treatments on the basis of previous researches, and submitted them to a comparative study, taking into account the historical developments of the various assets and vehicles.

Nevertheless, the process of corrugation evolving along the rail could not be observed directly on site observations or metallurgy studies. And the effects of tribological conditions such as the friction function, and the influence of material properties could not be precisely quantified. Previously, tribological investigations of rails affected by track corrugation have highlighted periodical plastic deformations coupled with Superficial Tribological Transformation[4] [5] [6]. But it is difficult to identify the various factors affecting such rail defect, and to quantify how the factor contributes to surface defect only on the basis of experiments.

To overcome the limitation of experimental surveys, a lot of numerical methods are developed [40-55] to investigate corrugation defects. Although a lot of publications present the comparison between numerical and measurement re-

sults, the generation mechanism of rail corrugation is still not completely understood. According to the literature [55][58][66][67], there are many works which try to constitute a more stable, less spurious oscillating numerical schemes. However, these studies are usually concerned about a solution in time discretization scheme, and many proposed strategies exhibit the drawbacks such as neglected kinetic energy at the contacting nodes, spurious oscillations introduced on the contact boundary or a small interpenetration. The existence, uniqueness and stability of a numerical solution is still generally unknown for wheel–rail contact modelling.

To better understand corrugation defect formation mechanism and to compensate for these numerical modelling drawbacks, a researching work of thesis is constituted and described in the manuscript for three main parts:

Part 1: The bibliographies are studied both on the metallurgy researches and on the numerical modelling researches. And the limitations to investigate the parametric influence on corrugation defects and the drawbacks of numerical modelling are presented. Therefore, an approach dealing with the local tribological analysis in wheel-rail contact is constituted and applied to the specific corrugation defects on straight-track under transient conditions.

Part 2: Through the numerical model, corrugation defects and the local contact dynamics between wheel-rail are analysed. The sensibilities of parameters which are applied under transient conditions and the influence of material properties on corrugation defects are going to be investigated. Not only the influence of a single wheel passing but also of multiple wheel passings are taken into account for the evolution of corrugation defects. Moreover, the influence of the geometric irregularity in the weld rail area are also considered about. The simulation results are highlighted that corrugation defect is not influenced by a unique cause.

Part 3: Through a compare between the numerical results and the on-site measurements on corrugation defects, there is an unusual energy dissipation

problem in the wheel-rail dynamic contact modelling, and the results in numerical model does not represent corrugation defects expected. As a more realistic corrugation defect on straight track is expected, a solution will be considered to improve the numerical modelling

Part 1

Introduction of corrugation in railway networks

Chapter 1. State of the art

1.1 Introduction

Railway transport is generally acknowledged for its low cost, environmental friendliness, energy efficiency, and fast speed (over short and medium distances) compared with other means of transportation. Therefore, railway operators and maintainers need to keep train service punctual, relatively quiet, comfortable, and low-cost. But defects of rail such as squats, cracks, corrugation, etc... appear in wheel-rail contact and affect railway operations in urban rail networks[7][12][13]; among these defects, rail corrugation is one of the most serious problems experienced by transit systems.



Figure 1.1 Sample of rail corrugation on a curved rail[14]

Rail corrugation is a periodical phenomenon which mainly appears on the running surface of the rail (Fig1.1) [14] with typical wavelengths between 25mm and 1500 mm. On the surface of severely corrugated rails, the shiny crests and darker troughs are easily recognized. The amplitudes can reach values up to hundred micrometres (μm) (Fig.1.2)[15]. Rail corrugation, showed in Fig. 1.1

and 1.2, illustrates severe wear as well as plastic deformation on the surface of rails, especially on the active flange.

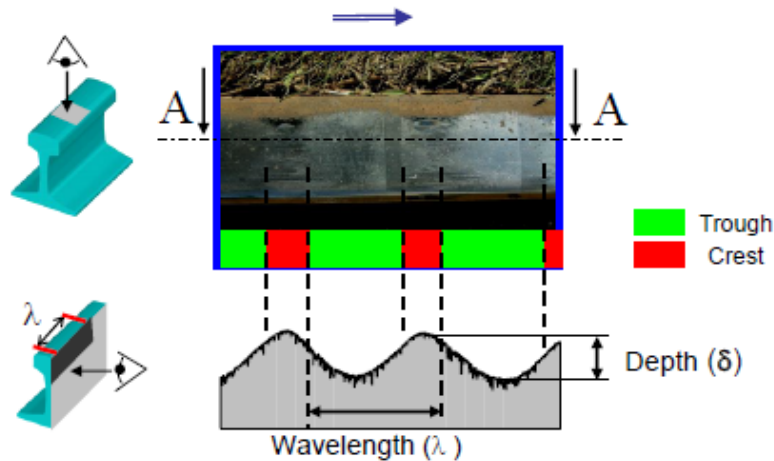


Figure 1.2 Characteristic parameters of rail corrugation on tangent rail[15]

Nowadays, the problems of rail corrugation with increasing axle loads and train speeds are apparent. These trends have led to an increased effort to understand the problem and to devise effective remedies. Indeed, these defects cause great changes in the rail profile and, therefore, strongly affect the running behaviour of railway vehicles, such as motion stability, riding comfort and derailment safety.

There is a great awareness that these defects could extent to an environment noise problem. Corrugation gives rise to high frequency vibration, in the range of 200 to 1500 Hz, and to an increase of noise emission[16]. It also causes fierce vibrations of the structures of both railway vehicles and tracks[17], discomfort for passengers and residents living near the tracks, damages for goods and reduction for structural parts lifespan [18][19]. Currently, the primary method for controlling corrugation is to grind the rail at regular intervals. However, corrugation develops so fast in some sections that the rail has to be frequently renewed because of this grinding procedure[20].

In order to find out more detailed observations of corrugation and the important factors affecting corrugation growth, some extensive and well-documented surveys are described in the following sections.

1.2 Review on corrugation study

1.2.1 Previous research from origin to the 1990s

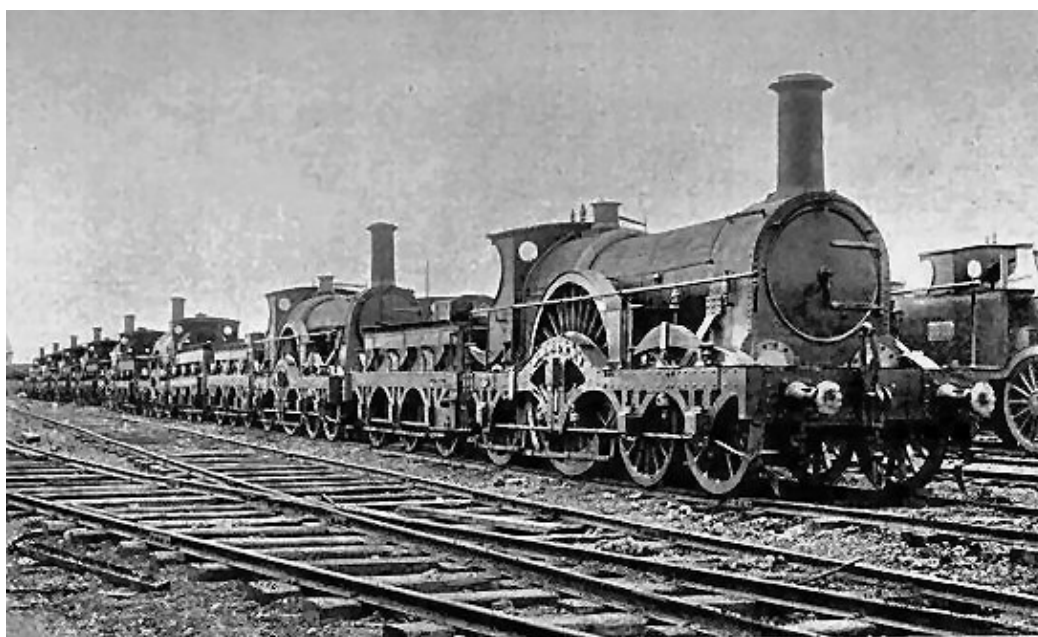


Figure 1.3 The Great Western Railway (GWR) - Iron Duke Class broad gauge locomotives[21]

In order to prevent the generation of rail corrugation, many studies have been reported in the world since the end of the 19th century. Many site tests were made and many surveys were conducted with a great variety of steel types, rail profiles, exploitation conditions, etc...

According to a review by K.H. Oostermeijer [1], the first report of corrugation in the literature dates back to 1889 on the Midland line in Great Britain. Then, in 1895, a report in the United States observed that corrugation gave rise to very poor ride comfort and high noise levels. In Germany, corrugation surveys

began as early as the 1930's. In 1953, Fink published a review paper on rail corrugation, mainly considering short-wavelength rail corrugation up to 5 cm.

The general situation on rail corrugation was discussed during a conference of the International Railway Congress Association (IRCA) in 1958. At the same time, possible causes of corrugation were investigated by Birmann[1]. In his paper, not only the vibrational behaviour of rail and wheelset was investigated, but also the prevention of corrugation growth, considering the aspects of rail material.

Several new attempts started in the 1970s. In 1975, Johnson and Gray [2] theoretically explained the self-generation of corrugations on metal surfaces in rolling contact on disc machines and validated it through experiments. They also distinguished the wavelength determined by the frequency of contact resonance and the formation and amplification of quasi-periodic pattern due to plastic deformation. According to the paper of Y.Sato[22], Mair in Australia investigated the cause of special long-wavelength corrugation related with the vertical dynamic behaviour of unsprung mass on a continuously supported track in 1977. In 1978, Eisenmann published a study on short-pitch corrugation, explaining that short-pitch corrugation was caused by the residual stresses in rail head. In 1979, Daniels et al. began their experimental investigation on the railway network of Pueblo, Colorado, establishing a test to provide an understanding of corrugation growth and corrugation mechanisms.

In 1983, two symposia on rail corrugation took place at the Berlin Technical University and in London, where papers of Frederick and Budgen[23], Clark and Kalker[24] were presented. In another paper published in 1986[22], Frederick showed how to quantify the dynamic response of wheel and rail to vertical, lateral and longitudinal forces, and how to predict whether or not a small wave in the surface of the rail will be deepened or erased by passing vehicles.

Valdivia (1988)[25] and Knothe and Ripke (1990) [26], suggested that corrugation formation can be explained as a feedback process between (a) wheel

and rail high frequency oscillations and (b) long-term wear phenomena. This work was continued in by Hempelmann and Knothe (1996) [27] and in Müller (1998)[28]. Through these results, corrugation is associated with a constant frequency, so that the wavelength varies in proportion to the predominant train speed. However, Müller in 1999[29] also introduced a wavelength-fixing mechanism for short-pitch corrugations besides frequency fixing mechanisms. If only considering the contact mechanical effects, there is a tendency to produce the corrugation in a wavelength range of 2cm to 8-10cm.

Many studies have been reported from the end of the 19th century to 1990s. But the theories introduced above did not completely explain the mechanism of corrugation formation. For example, only the contact mechanism was considered, and the wear or damage mechanism was ignored [29].

In 1993, Grassie and Kalousek [3] presented a classification of corrugation with their characteristics, causes and treatments on the basis of these researches, after submitting them to a comparative study, taking into account the historical developments of the various assets and vehicles. In the next section, the classification will be introduced.

1.2.2 Classical classification of rail corrugation by Grassie and Kalousek

Corrugation of rails occurs on nearly every railway networks. The phenomenon is a more or less periodic irregularity on the running surface which gives rise to high dynamic loads between wheel and rail, degradation of the ballast and other track components, noises, etc...[29][30][31]. It is important to highlight that corrugation is not a single phenomenon with a unique cause and a unique solution or treatment, and a better categorized study would help to understand the corrugation characteristics.

According to Grassie and Kalousek [3], categorization of corrugations can be made through two mechanisms: the damaging of the rail (wear, plastic flow etc.) and the corrugation wavelength. Figure 1.4 illustrates a feedback loop of

these two mechanisms: the rail is initially uncorrugated, but the profile is composed of the irregular roughness and combined with other factors such as traction, creep and frictions. These characteristics excite dynamic loads at the wheel-rail contact and lead to damages, thereby modifying the initial profile. Since the trains roll over the site at a similar speed, the wavelength varies similarly, thus corresponding to a wavelength fixing mechanism. The modified profile of the rail and the damages tend to exacerbate vibration of subsequent trains and leads to further damage.

This diagram (see Fig. 1.4) helps to understand the formation of corrugation caused by the structural dynamics or material behaviour. Based on Grassie and Kalousek's researching experience over the last decade [3], the corrugation is classified into six groups (Table 1.1) according to 'wavelength fixing'.

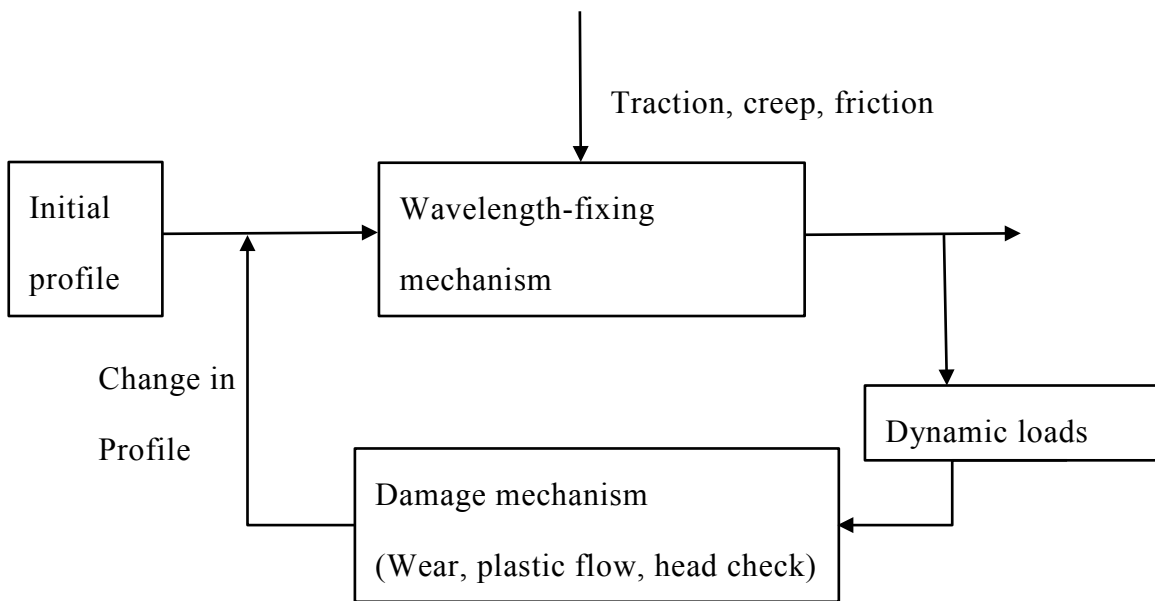


Figure 1.4 Feedback loop of structural dynamics and contact mechanics (wavelength-fixing mechanism) and damage mechanism [3]

Type	Wavelength (mm)	Wavelength fixing mechanism	Damage mechanism
I Heavy haul	200-300	P2 resonance	Plastic flow in troughs
II Light rail	500-1500	P2 resonance	Plastic bending
III Booted	45-60(RATP) 51-57 (Baltimore)	Sleeper resonance Flexural resonance of wheel set	Wear of troughs Lateral oscillation Plastic flow of peaks
IV Contact fatigue	150-450	P2 resonance latterly	Rolling contact fatigue
V Rutting	50(trams) 200(RATP) 150-450(FAST)	Torsional resonance of wheelset Peak vertical dynamic force	Wear of troughs from longitudinal oscillation
VI Roaring rails	25-80	Unknown	Wear of troughs from longitudinal slip

Table 1.1 Types and characteristics of corrugation[3]

Table 1.1, proposed by Grassie and Kalousek[3], has proved to be a useful and less misleading means of classifying corrugations. There are six types of cor-

rugation classified in Table 1.1, each type of corrugation has a particular combination of wavelength-fixing and damage mechanisms.

Table 1.1 makes several reference to “pinned-pinned resonance” (or “P2 resonance”), which is a resonance in which the rail vibrates as a fixed beam, as if a beam was pinned between periodically-placed sleepers[32][33]. Table 1.1 clearly shows the excitation of the P2 resonance is responsible not only for the variation in corrugation amplitude at sleeper pitch, that is commonly seen on main-line railways in Britain e.g.[32], but also contributes to the “wavelength fixing” mechanism for corrugation. In an investigation of causes and treatments of corrugation encountered on metro railways in the United States, it was found that the principal wavelength-fixing mechanism for corrugation on these metro systems was the second torsional resonance of driven wheelsets, in which the main drive gear oscillates in anti-phase to the wheels [34]. In the meantime, the P2 resonance of the unsprung mass on track stiffness is a significant wavelength-fixing mechanism for many types of corrugations. The corrugation was also excited by extremely severe and frequent discrete irregularities at joints[3][34].

Figure 1.5 shows different types of resonances contributing to the formation of corrugation. As a result of dynamic resonances, several types of corrugations occur in both tangent rail and curved rail. The formation of corrugation is likely to be exacerbated by conditions that result in different tractions by wheels that run on the high and low rails, particularly if one wheel is in full slip and the other not.

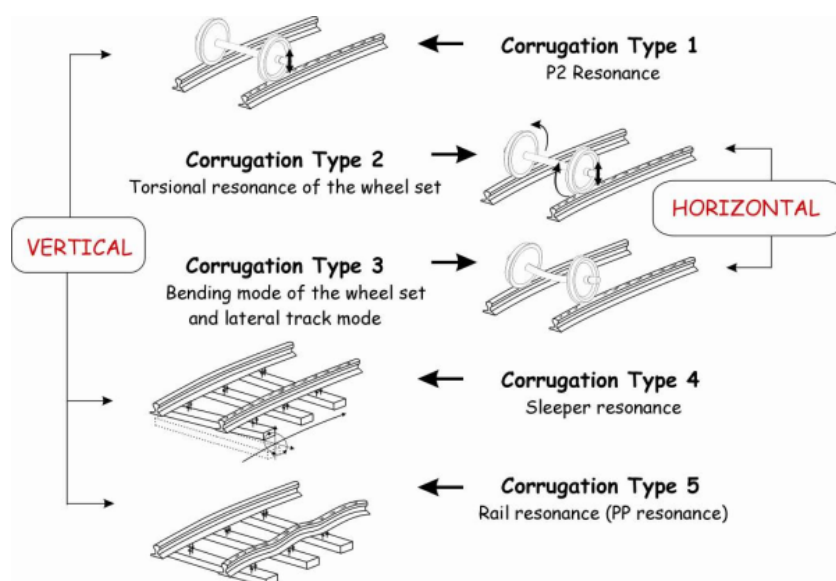


Figure 1.5 Different resonances of the coupled vehicle-track system[35]

The classification defined by Kalousek and Grassie provides a summary of the previous studies, which helps understand whether structural dynamics or material behaviour is mainly responsible for the formation of rail corrugations. In their paper [3][34], most types of corrugation are understood from both damages and wavelength fixing mechanisms. But the wavelength fixing mechanism of roaring rail corrugation is unknown, and the tribological aspect of the corrugation still remains a mystery. Therefore, in the next section, we will concentrate on the metallurgical study of short-pitch corrugation.

1.2.3 Description of corrugation defects: Short-pitch corrugation

1.2.3.1 Observation of superficial morphology

The roaring rail corrugation is also called “short-pitch corrugation”, and mainly occurs on tangent tracks (or on curves with large radius of about a thousand meters). The short-pitch corrugation shows an undulation of the rail surface with typical wavelengths, between 25 - 80 mm. The amplitudes can reach values up to several hundred micrometres.

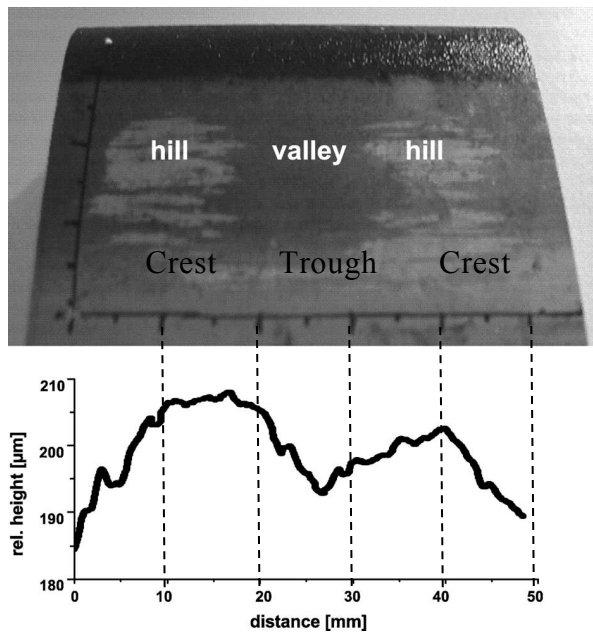


Figure 1.6 Surface topography of the rolling surface[4]

In the paper of Wild [4], this phenomenon is described as ripples which present a nearly regular succession of waves with shining wave hills (crest) and dark wave valleys (trough) on a rail rolling surface (Fig.1.6). A succession of polished shiny areas was found on rail running surfaces and contrasts with a duller base. The shiny patches are 25 to 80 mm apart and are generally quite regularly spaced. The shiny, raised parts correspond to the highest points of the bumps, the dark parts correspond to the lowest points and the dark parts are oxidised. Metallographic analyses reveal that the peaks have a hardened martensitic structure to a very slight depth (from a few hundredths of a millimetre to 0.05 mm).

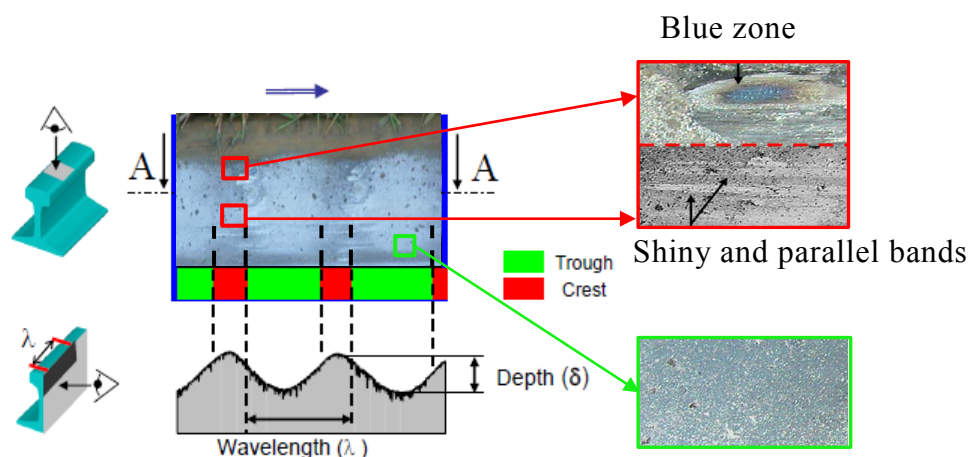


Figure 1.7 Short-pitch corrugation on tangent track[15][36]

Figure 1.7 shows a typical example of a corrugated rail. Two morphologies can be distinguished at the corrugated rail surface (Fig.1.7): smooth and shiny crests, homogeneous and matt troughs. From the surficial observation on the corrugated rail, the shiny parts are parallel to the direction of train. According to Grassie[37], the sliding between wheel and rail would give rise to the corrugation defect in this zone. In the crest area, a blue zone is also locally found and corresponds to the sliding in contact, coming with the increasing temperature in this area. Unlike the crest appearance, the trough appearance (Fig.1.7) is similar to an uncorrugated rail surface.

Besides the superficial observation of the two morphologies, the unknown microstructures of material in the rail subsurface also need to be investigated.

1.2.3.2 Observation of subsurface microstructure

In this section, a microstructure of corrugated rail is presented according to the research work of Wild [4], which describes corrugation raised under a track load between 10 and 20 tons, and under track speed between 50 and 120Km/h.

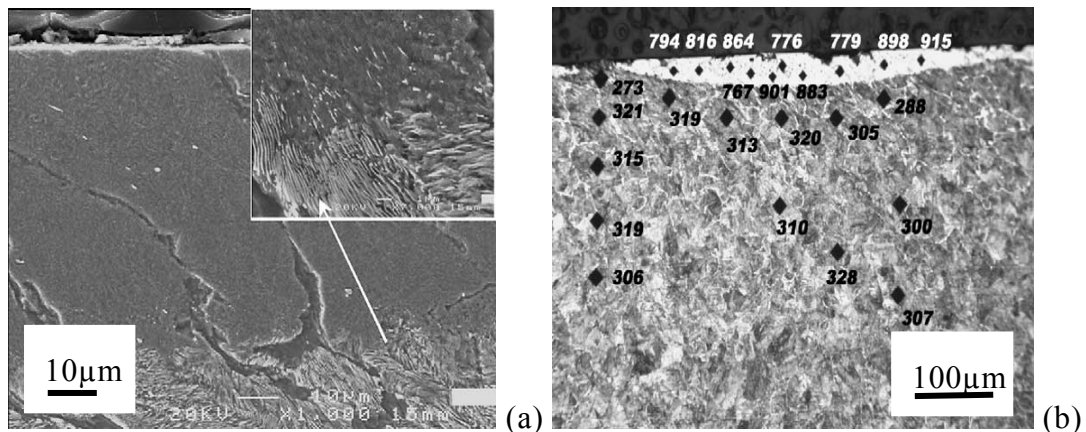


Figure 1.8 (a) White etching layer in the cross-section of crest, (b) Microhardness distribution beneath the surface of crest[4]

The observation of microstructure on the crests does not show significant orientation of the cementite lamellae (Fig.1.8(a)). There is no lateral material flow in the crests area, and this zone appears homogenous. However, under the observation with optical microscope, the cross section specimen reveals that there are some bright patches on the crests, called white etching layers or tribologically transformed structure (TTS) of the rails (Fig.1.8 (a))[38]. The thickness of the white etching layer varies between approximately 5 and 20 µm (Fig.1.8 (b)). The maximum hardness values appear in the bright patches on the crests. Usually, the appearance of such phases is attributed to the martensitic transformation of steel and its fast cooling, carried out in a temperature of more than 700 °C (in atmospheric pressure). Yet, the temperature in a wheel-rail contact rarely reaches more than 400 °C, which is not enough to begin martensitic formation[39]. So the increase of temperature on the surface of the rail is not the unique reason which affects the development of these white phases; high contact stress and shear stress also contribute to the microstructural transformation[40][41].

Microhardness determination on the crest area shows that the hardness in the white etching layers is considerably higher at the surface (about 800-900 HV) than in the areas under the surface (about 300 HV). The transformation to

white phase appears to form on the crests of rail irregularities, where the contact pressures and frictional force are highest.

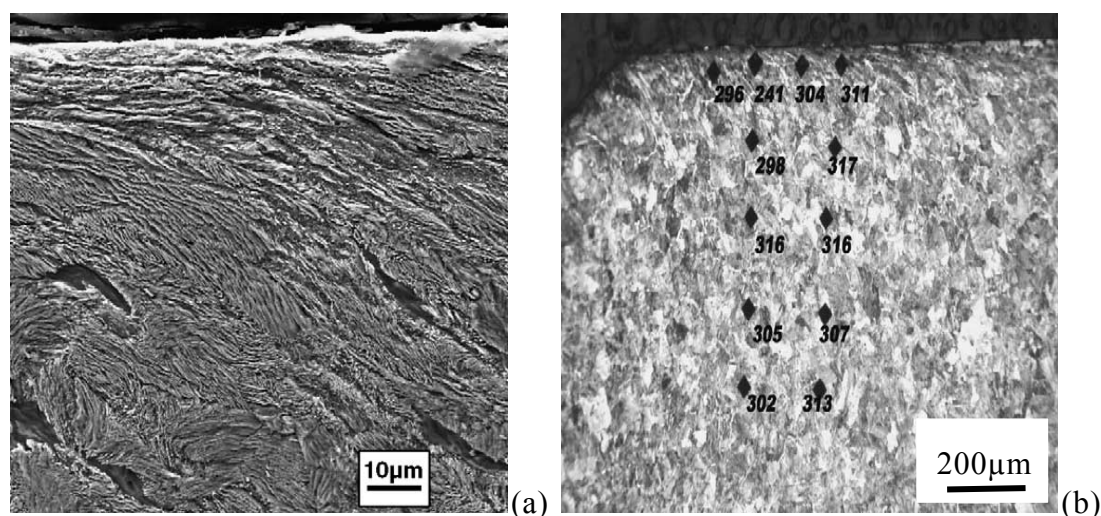


Figure 1.9 (a) Etching relief in the cross-section of trough, (b) Microhardness distribution beneath the surface of trough[4]

On the troughs of corrugated rail surface, the superficial view on top of the rail does not show obvious material changes. But referring to the optical and scanning electron microscopy images of the cross-section of the troughs[4] (Fig.1.9(a)), the microstructure of the material is severely modified from its original status. Optical and scanning electron microscopy shows that the deformation layer has a thickness of approximately 150 µm. Initially non-orientated, cementite lamellae reach an orientation of approximately 45° to the rail surface, and even become parallel to the rail surface. This indicates strong friction effects. The microstructure appears to have suffered from strong plastic deformation undulated along the traffic direction and related to the sliding condition of wheel-rail contact.

The hardness distribution on the troughs surface is uniform (Fig. 1.9.b), at a value of approximately 300 HV and the microhardness varies between 240 and 311 HV in the depth of 150 µm (Fig. 1.9.b). It is inferred that the hardness of the deformation layer is influenced by tribological conditions, such as friction, pressure, etc... during the contact of rail and wheel.

In general, there are several observations on short-pitch corrugation:

- Corrugation exhibits severe plastic deformation along the direction of track, dependent on the location of the contact patch;
- Steel Hardness at the crests is significantly higher than at the troughs;
- Corrugation is essentially stationary in position. The crests and troughs do not translate as the trains pass. The plastic deformation seems stronger at the trough than at the crest, which progressively produces corrugation;
- White etching layers (WEL) are often found on corrugation crests.

The short-pitch corrugation is investigated with both the superficial and the microstructural morphologies. However, the process of corrugation evaluating along the rail could not be observed directly on metallurgy study. And the effects of tribological conditions could not be precisely quantified. It is thus necessary to investigate this corrugation referring to the theoretical study.

1.3 The wheel-rail contact theory

Since the appearance of corrugation is one of the serious problems encountered, the need of the wheel-rail traction capabilities is becoming more and more urgent. As a consequence, it is necessary to understand corrugation defect with a more precise tool and the influence of wheel-rail contact in both tangent and normal directions on these defects. Therefore, a model using the wheel-rail contact theory is proposed to study the corrugation defects.

1.3.1 Normal contact theory - Hertzian theory

Geometrical effects on local elastic deformation properties were considered as early as 1880 with the Hertzian Theory of Static Elastic Deformation [42]. This theory relates the circular contact area of a sphere with a plane (or more generally between two spheres) to the elastic deformation properties of the materials.

In this theory, any surface interactions, such as adhesive contact interactions, are neglected. According to the Hertzian Theory, the contact area and the normal stress carried by it can be calculated.

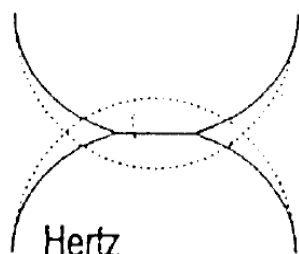


Figure 1.10 Hertzian Static Contact Mechanical Models (fully elastic model)

The Hertzian Theory leads to an elliptical contact area and a semi-ellipsoid contact pressure distribution in the contact area. Due to its efficiency and simplicity, this theory has been extensively applied since its publication. However, there are two limiting conditions for the applications of this theory:

- a) The contact between elastic bodies should be frictionless,
- b) The significant dimensions of the contact area should be much smaller than the dimensions and the radius of curvature of the bodies in contact.

According to this theory, the wheel-rail contact is considered as a two curved surfaces contact, and a simplified model of the wheel and the rail is used (see Fig.1.11) [42].

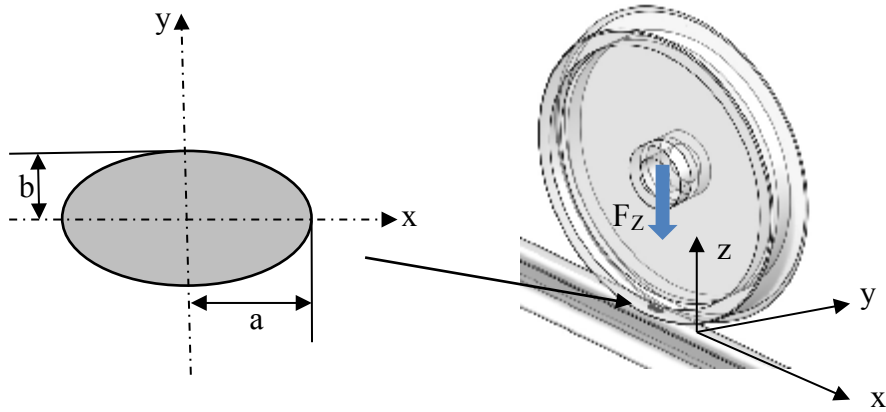


Figure 1.11 Assumption of distribution of normal and tangential stresses in the wheel-rail contact area[42][43]

According the Hertzian Theory, the contact surface is elliptic in semi-axes defined by[42][44]:

$$C = \{(x,y,0) / (x/a)^2 + (y/b)^2 \leq 1\}$$

$$b = \sqrt[3]{\frac{6k^2 \varepsilon F_z \bar{R}}{\pi E'}}$$

$$a = \frac{b}{k} = \sqrt[3]{\frac{6\varepsilon F_z \bar{R}}{\pi k E'}}$$

a and b are defined as the major semi-axis of the ellipse and the minor semi-axis. k is the ratio of the contact semi-axes: $k=b/a$. \bar{R} is the reduced radius of contact, and E' is the reduced elastic modulus.

$$\frac{1}{\bar{R}} = \frac{1}{R_x} + \frac{1}{R_y}$$

$$\frac{2}{E'} = \frac{1-\nu_1^2}{E_1} + \frac{1-\nu_2^2}{E_2}$$

R_x is the effective radius of curvature in x-plane. R_y is the effective radius of curvature in y-plane. E is elastic module and ν is poison ratio.

Approximate solutions for the elliptical integrals are given in [43][44]:

$$k \approx \beta^{2/\pi}$$

$$\varepsilon \approx 1 + \frac{s}{\beta}$$

$$F \approx \frac{\pi}{2} + s \ln \beta$$

with $\beta = R_y / R_x$ and $s = \pi / 2 - 1$

The maximum Hertzian pressure denotes by p_h is given by:

$$p_h = \frac{3\omega}{2\pi ab}$$

The pressure distribution denotes by $p(x,y)$ is given by:

$$p(x,y) = \begin{cases} p_h \sqrt{1 - (x/a)^2 - (y/b)^2}, & \text{if } (x/a)^2 + (y/b)^2 \leq 1; \\ 0, & \text{otherwise.} \end{cases}$$

1.3.2 Tangent contact theory - Traction, Friction, and Adhesion

1.3.2.1 Rolling/sliding wheel-rail contact model

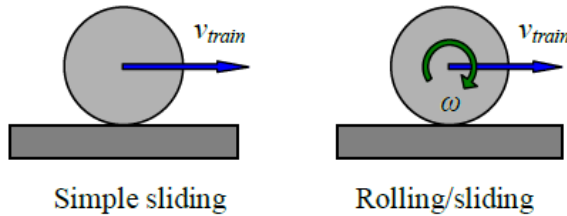


Figure 1.12 Rolling/sliding wheel-rail contact

When it is said that wheel-rail contact is a sliding/rolling contact (Fig.1.12), it is implied that the peripheral velocity of the wheel is comparable within limits to the global velocity of the train. Consider a rail, see (Fig.1.13). A Cartesian coordinate system is attached to x-axis along the rail, the y-axis points to right when one looks along the direction of x-axis, the z-axis points vertically downwards stats. The wheel rolls to the direction of x-axis with a rolling velocity V_{train} which we can call Velocity-advanced, and the wheel has a circum-

ferential velocity V_{wheel} . If the wheel is regarded as a rigid body, the value $V_{\text{train}} - V_{\text{wheel}}$ is called as the relative slip of wheel over the rail. So the longitudinal creepage is derived as coefficient of sliding:

$$\Gamma = \frac{V_{\text{train}} - V_{\text{wheel}}}{V_{\text{train}}}$$

This relative sliding exists in the x-y plane of contact, and is composed of a translation velocity in the plane x-y, and rotation around the z-axis.

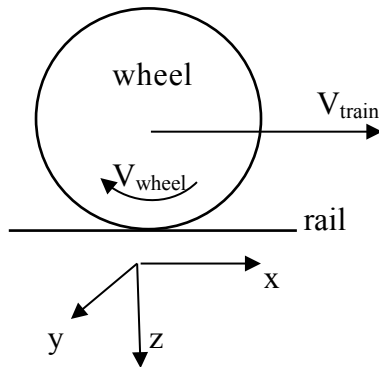


Figure 1.13 Simplified 2D model of wheel-rail contact. [24]

1.3.2.2 The quasi-static model of wheel-rail contact with friction

The first theory of rolling contact with friction was developed by Carter in 1926 [24]; it is a two-dimensional theory, which considers the wheel as a cylinder, and the rail as a thick plate and in which only the sliding coefficient is taken into account. Figure 1.14 shows a typical local loading.

There was also an unbounded half-space hypothesis to compute exact integral terms by Green kernel method, without computer, during 1920s [45].



Figure 1.14 Local traction distribution according to Carter Theory (2D model: S is an area of slip; A is an area of adhesion.)

In Kalker's theory [42], the problem of wheel-rail contact is modeled in quasi-static scheme, without any consideration of the inertia effect. Owing to the elasticity of the wheel and rail, contact area between the two bodies is an elliptic form, which respects the Hertzian Theory. The friction force between two bodies in contact during sliding is defined as the lateral applied force necessary to maintain constant motion. The coefficient of friction is defined as the friction force divided by the normal force, which loads the system. In simple sliding tribological systems, the coefficient of friction is often referred to as Coulomb type [46][47].

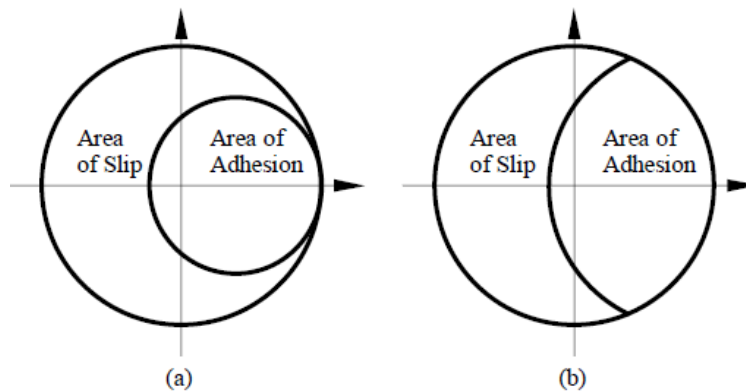


Figure 1.15 Division of the contact area (adhesion and slip) of a rolling/sliding contact after (a) Kalker [24] and (b) Haines and Ollerton.

In rolling/sliding contacts, i.e. wheel-rail contact, the Coulomb model of friction is applied for static case and a more complex modelling is required due to so-called adhesion and interfacial slip areas which appear in the contact area (Fig. 1.15).

From a tribological point of view[48], adhesion is the force required to separate two surfaces that have been brought into contact. However, the term “adherence” has become widely used in the wheel–rail research community to refer to the tangential force exerted in the wheel–rail contact, for example, as

used by Fletcher et al.[49] and Lewis[48]. Friction force is defined as the resistance encountered by one body moving over another.

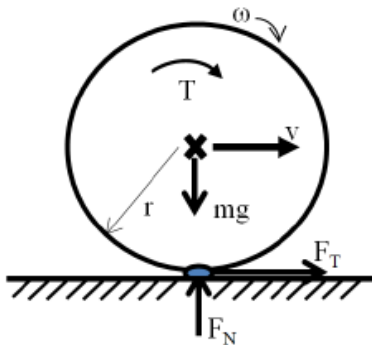


Figure 1.16 Schematic of a rolling–sliding contact under acceleration (X is the gravity centre; all forces in the figure are acting on either the block or the wheel) [48].

Figure 1.16 [48] shows a cylinder rolling along a stationary plane surface. This is analogous to the case of a wheel rolling along a rail. The wheel is subject to normal force, F_N , and travels along the rail at velocity V . The wheel is subject to torque, T , which maintains the angular velocity of the wheel, ω , and also causes a reactive tangential force, F_T , at the wheel–rail interface. The tangential force of a driving wheel is known as traction, which ultimately propels the wheel along the rail. During deceleration, the tangential force, F_T , opposes to the running direction due to the braking torque, T , applied anticlockwise. The tangential force F_T in the longitudinal direction during both acceleration and deceleration is referred to as adhesion.

The transmitted tangential force on the wheel refers to the adhesion and traction mentioned above, and the tractive force refers to the applied force. During acceleration or when overcoming losses while driving at constant speed, the tangential velocity at the wheel surface, ω , of a driven wheel will always be greater than its body velocity, V . The difference between the tangential velocity of the wheel, ω , and the body velocity, V , divided by the rolling velocity is referred to as creep[42].

Since adhesion is the tangential force in the longitudinal direction, the creep discussed here refers to longitudinal creep and the contact refers to the wheel tread–rail head contact. In the railway literature, slip is sometimes used instead of creep. However, to distinguish slip from micro-slip, the term “creep” will be used throughout this thesis instead of “slip”.

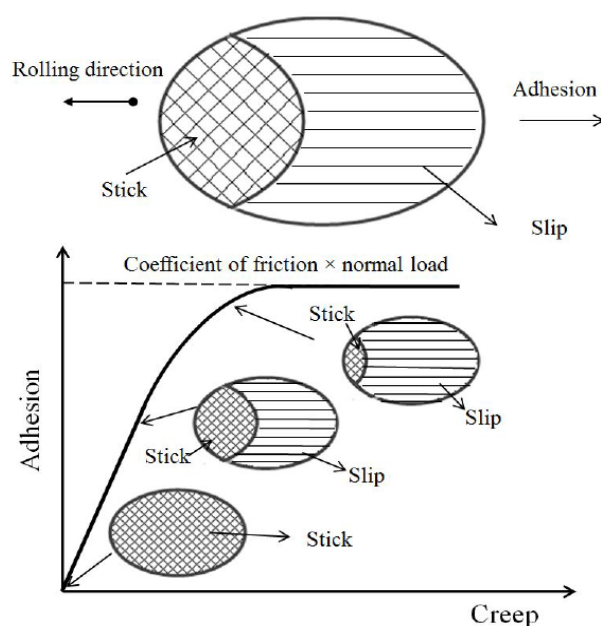


Figure 1.17. A creep curve showing the relationship between adhesion and creep[50]

Fig.1.17 shows the relationship between creep and adhesion for a typical dry wheel–rail contact. This plot of adhesion versus creep is known as the creep curve. When the creep is zero, the whole contact area sticks and no tangential force is transmitted, in what is known as “free rolling”. However, zero creep does not exist in reality, since the inevitable deformation between two contact bodies results in a certain amount of creep. Slip occurs at the trailing edge and spreads forward through to the contact area as the adhesion increases. The slip area increases and the stick area decreases, resulting in a rolling–sliding contact until pure sliding appears. In that state, the adhesion equals the friction force between two bodies under pure sliding conditions. When the creep is

small, the adhesion increases in an approximately linear fashion with increased creep. After that, the slope of the creep curve (the increasing rate of adhesion) decreases with increased creep. At approximately 1–2% creep, the slope of the creep curve and the stick area are extremely small, and the adhesion is very close to the friction. For a typical creep curve in the railway context, the adhesion decreases after reaching its maximum [50], typically at 1–2% creep under dry and clean conditions. The adhesion at that point is considered the maximum tangential force that approximately equals the friction force.

1.3.2.3 Stick-Slip mechanism in corrugation defect

In any rolling motion, creep occurs due to the finite size of the contact patch. Creep may be caused by roll-slip behaviour, due to decreasing friction associated with increasing creepage. Roll-slip behaviour may be determined primarily by geometrical characteristics such as contact patch dimensions, because short-pitch corrugation often has a wavelength that is relatively independent of vehicle speed, called geometric fixing mechanism.

Grassie and Kalousek [3] indicate that short-pitch corrugation is further aggravated by high contact forces at the peaks of corrugation and low contact forces resulting in slip at the troughs. Stick-slip effect as a corrugating mechanism is also supported by Grassie, et al. in a mathematical and experimental study of short-pitch corrugation [32]. Creep is predicted at corrugation crests due to an out-of-phase relationship between wheel-rail contact force and rail profile. Modelling of wheel-rail contact behaviour in the presence of contact separation or lateral and longitudinal slip is complicated by the non-linearity of the vertical contact load versus vertical displacement, and slip versus vertical displacement. So the dynamic wheel-rail contact model is required to understand the corrugation formation process.

1.4 Numerical method applied to analyse corrugation defect

Previously, tribological investigations of rails affected by track corrugation have highlighted periodical plastic deformations coupled with Superficial Tribological Transformation[5][4][6]. But it is difficult to identify the various factors affecting such rail defect, and to quantify how much the factor contributes to surface defect only on the basis of experiments. As a consequence, tribological investigations on real rails affected by such defect have to be completed with numerical modelling. So far, many works have been done to investigate the corrugation defect by numerical modelling.

Several hypotheses were suggested to explain the development of short-pitch corrugation. Until now, however, no generally accepted explanation was given. Different phenomena are probably involved in creating corrugation of different wavelengths. One idea put forward by some authors is that the short-term dynamic behaviour of the train-track system causes long-term wear to develop. Other authors tried to refine dynamic models of wheels and tracks, trying to find a corrugation-initiating mechanism in terms of short-term behaviour of the wheel-track system. Thus, many authors tried many different hypotheses to explain the origin of rail corrugation.

Clark and Foster (1983) [51] put forward that self-excited vibration characteristics of a flexible wheelset and track system under high creepage conditions may provide possible explanations for the formation of corrugations on the running surface of the rails. But their model is very specific for the creep characteristics on sharp curve. Suda and Iguchi (1989) [52] stated that the corrugation growth conditions depend on the natural frequencies of the system. By appropriate selection of the natural frequencies, it would be possible to reduce the development of corrugation of one wavelength without inducing growth of corrugation of other wavelengths. They also stated that rolling direction and speed have a great influence on corrugation growth. Then a linear model giving wear rate as a function of frequency was suggested by Tassilly and Vincent (1991) [53]. A transfer function between the initial wheel and rail roughness

and the wear rate spectrum in the contact patch was presented. Under some conditions, the initial roughness on the rail was shown to degenerate into corrugation in some frequency bands. The model was used as a tool to design track modifications and to prevent corrugation growth. However these models focus on the structure of the vehicle system, the roughness of rails surface and the frequency of wheelset and track system, but the damage mechanisms, such as plastic flow, which influence the corrugation formation are neglected.

Ideas including plastic deformation of the railhead are put forward by Cervoni and Vincent (1986) [54], Bogacz *et al.* (1987) [55], and Suda and Iguchi (1989) [52], and Böhmer and Klimpel [56] have provided a more complete research. They used mathematical models to study the influence of work hardening and residual stresses on corrugation and considered the influence of plastic deformation as a possible saturation mechanism for corrugation growth. A plane strain finite element model in quasi-static is thus introduced.

In the last 15 years, many numerical models were developed to investigate the formation and evolution of corrugation defect. The validation of the numerical model is applicable for analyses of loading condition of wheel-rail contact, plastic deformation, fatigue and corrugation [7][57][58]. Wen *et al.* combine the non-Hertzian three-dimensional rolling contact theory with the friction theory. They did a series of simulations about the formation and evolution of corrugation on a curved rail to investigate the effect of train speed and vibration of track on corrugation [59][60]. The concept of feedback between the corrugation development and the train-track dynamic are also considered in the simulation [14] [31] [57]. Meanwhile, a 2D-dynamic finite element model of wheel-rail contact was developed to reproduce such periodical defect [61]. Results show a specific contact dynamics consequence: the birth of periodical plastic deformation on the rail surface as well as periodical increase of local sliding and temperature-up to hundreds of Celsius degree [8][20][62]. Nevertheless, such simple 2D-modelling was performed only with a single pass of a

wheel. But several wheels are required to fully develop straight-track corrugation.

Although a lot of publications present the comparison between numerical and measurement results, the generation mechanism of rail corrugation is still not completely understood.

1.5 Conclusion

This part introduced the corrugation characteristics, the formation mechanism, the morphology and the consequence of these phenomena. Since the rail corrugation problem is getting severe, grinding or planning merely alleviates the symptoms. Investigating researches are necessary to help better understand the corrugation defect. In this part, the static and dynamic contact theories were presented to help understand the wheel-rail contact theory; and with referring to the previous numerical models developed by the researchers, dynamic impact problems in the wheel-rail contact is still an open mathematical issue. The existence, uniqueness and stability of numerical solution is still unknown in general for wheel-rail contact modelling. Therefore, the following part is going to select an appropriate tool to constitute the dynamic wheel-rail contact model.

Chapter 2. Numerical modelling of wheel–rail contact dynamics

The short-pitch corrugation defect is acknowledged as an important aspect to be studied; although the problem has been known and investigated for many years, a fully satisfactory explanation of the phenomenon has not yet been found. Experimental investigations in which corrugation evolves over thousands of trains passings are very difficult to carry out. Instead, numerical simulations have become a powerful tool in the search for understanding corrugation evolutions by instrumenting the contact locally. In the following work, a proper numerical model will be selected to investigate the dynamic local contact problem that deals with corrugation defect formation on straight track. For this purpose, it is necessary to constitute a wheel-rail contact model that is able to represent the corrugation raising process and simplified to save computational cost.

2.1 Numerical model chosen to study the wheel-rail dynamic problem: the mechanical scale

According to the previous introduction about the numerical methods applied to analyse the corrugation defects, the choice of numerical tools depends on the scale in which we investigate the phenomenon. At present, there is no perfect tool to fully describe the corrugation defect.

To constitute the model, the first strategy is to use the coupling model of vehicle-track interaction to investigate the material deterioration of the rail profile (Fig.2.1)[63]. This type of model mainly deals with the global influence of train speed, axle load, etc... and regards the wheelset or rail and track as rigid. The interactions between the bogie and the wheelset, and between the rail and the sleepers are highlighted in these models. But the local wheel-rail contact condition is not determined, and the dynamic impact problem of wheel-rail

contact is not well detailed. The multi-bodies model only considers the interaction of rigid bodies, whereas the continuum mechanics that deals with the analysis of the kinematics and the mechanical behaviour of materials is neglected.

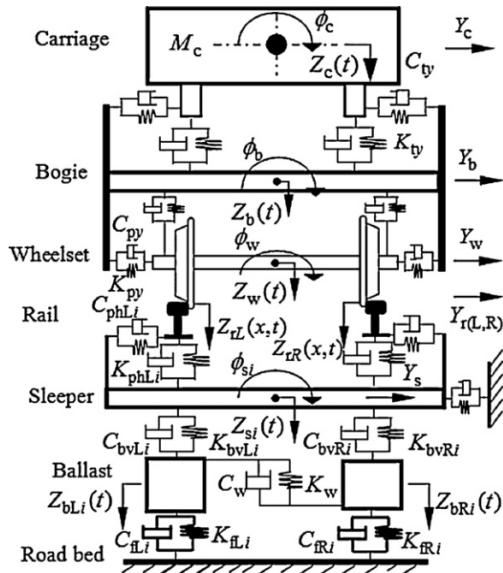


Figure 2.1 Coupling model of vehicle-track interaction[63]

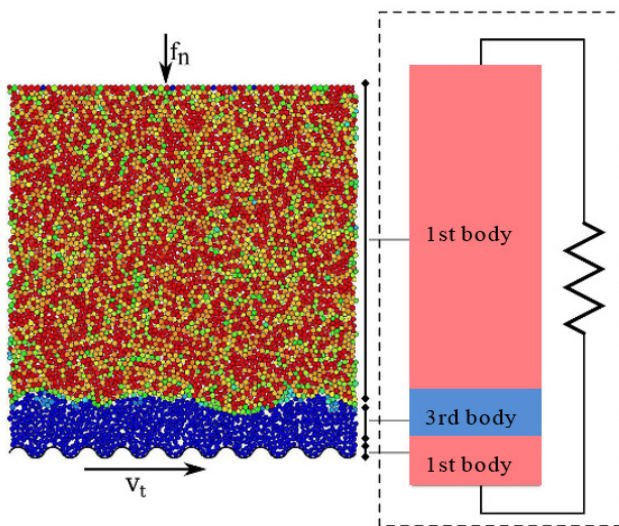


Figure 2.2 Discrete element method to present tribological triplet[64]

Another strategy deals with a microscopic aspect using the Discrete Element Methods (DEM) to investigate the divided feature of some media such as granular ones, masonries or 3rd body layer in the contact interface. Classically, DEM are based on the interactions between particles and their resulting influence at the macroscopic scale of the interfacial media (Fig.2.2) [64]. However, these discrete element methods are relatively computationally intensive, which limits either the length of a simulation or the number of particles. It is a real hard challenge to transfer the mechanism interaction between the wheel-rail contacts at this scale.

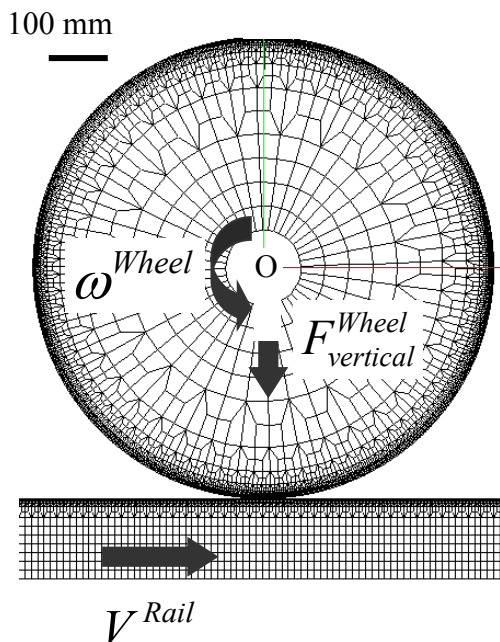


Figure 2.3 FEM model of wheel-rail contact

The third approach deals with the scale of the 1st body, the interaction localized between the wheel and the rail using continuum mechanical model. The quasi-static or dynamic models using finite element method (FEM) are widely applied to describe the deformations and the local contact problem (Fig.2.3)[61]. This method has some limitations for not considering the global vehicle system, 3rd body layer, etc... Moreover, in dynamic contact problem,

models constituted in commercial FEM software are dissipative, imprecise with penalization method or unstable without artificial viscosity etc. But the convenient application, the well-developed integration scheme show the advantages to apply the FEM approaches. Especially, there are more and more commercial FEM software (Abaqus, ANSYS, etc.) which provide a fast hand-program work platform. Many scientific researchers are working on wheel-rail contact problems using this method and they provide many examples to compare with and that could be better developed. Therefore, the FEM model is chosen primarily to investigate the dynamic local interaction of wheel-rail contact problems.

2.2 Description of the model

2.2.1 A simplified wheel-rail dynamic contact model

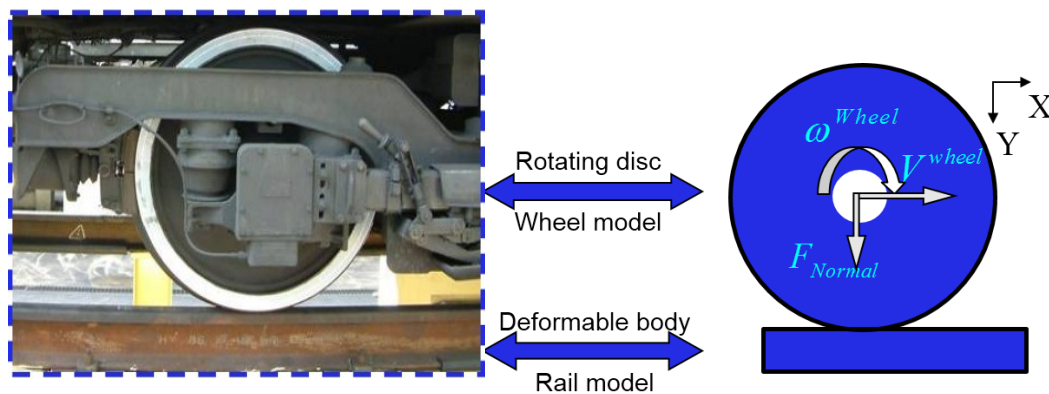


Figure 2.4 Simplified wheel-rail contact model

Referring to the wheel-rail contact problem, the first strategy is to use a simplified model of the frictional contact between two 2D-deformable bodies (Fig.2.4). The wheel is simplified as a disc with the interior radius as 70 mm and exterior radius as 430 mm (Table2.1) in 2D. The value corresponds to a real wheel geometry in French metro and tramways. A French audit measured the average speed of the metro and tramway at about 20km/h [65], and of ur-

ban train from 50 to 200 km/h. Therefore, the translating velocity is chosen as $V_{\text{wheel}}=17\text{m/s}$, and an angular velocity $\omega_{\text{wheel}}=39.5\text{rad/s}$ is applied at the centre of the wheel. Considering masses of trains and passengers, each car can weigh about a hundred tons and each wheel-set is loaded with about 80kN. When the data is transferred in the 2D wheel-rail contact model, the load F_{normal} is defined as 8kN and vertically applied at the centre of the wheel.

As the wheel-rail contact model is going to represent the corrugation defect raising process, the rail body in the 2D model is described as elasto-plastic behaviour. In order to get closer to rail material property, a law of linear elasto-plastic with isotropic linear hardening properties is used for the rail material: $\sigma_{\text{ep}}=455+250 \varepsilon_{\text{p}}^{\text{P}}$, with σ_{ep} being the equivalent plane stress and ε_{p} the equivalent plastic plane strain. Because the plastic flow is mainly localized in the rail body, the wheel is defined with elastic behaviour to save the computational cost (see Table 2.1).

	Rotating disc (wheel)	Deformable body (rail)
Young's modulus E (MPa)	205,000	205,000
Poisson's ratio ν	0.3	0.3
Density ρ (Kg/m ³)	7850	7850
Dimensions (mm)	$R_{\text{int}}^{\text{wheel}}=70$ $R_{\text{ext}}^{\text{wheel}}=430$	$L_{\text{rail}}=2340$ $H_{\text{rail}}=150$
Material behaviour	Elastic	Elasto-plastic

Table 2.1 Characteristics of the deformable rotating disc (wheel) and the deformable body (rail)

2.2.2 Strategy applied to constitute the wheel-rail dynamic contact model

The wheel-rail dynamic contact problem is a differential partial evolution equation under unilateral constraints. In Appendix 1, the mathematical model is briefly presented, using the continuous mechanical framework theory according to the assumptions described in previous sections. Unfortunately, as it is well known, only a few existing results for the elasto-static problems with Coulomb friction have been mathematically proved, with some reasonable assumptions on the regularity of the boundary and for a sufficiently small friction coefficient. The uniqueness of the solution for a small friction coefficient is an open problem. Examples of non-uniqueness were exhibited in for a large friction coefficient.

Then, in order to solve numerically the continuous equations of wheel-rail dynamic contact problem, space and time discretization schemes are applied.

Firstly, we discretized the problem in space with a finite element method: 2D-stress 4-node linear plane strain quadrilateral element, and a structural mesh distributed along the wheel-rail profile. The numerical Abaqus model starts with a smooth contact surface and the standard μ -Coulomb's friction law is applied at the contact with the friction coefficient $\mu=0.3$. The influence of the friction coefficient will be studied later in the next chapters.

The time integration code in Abaqus cannot be solved by using explicit Euler method, because it exposes a difficulty to complete the calculation and the Lagrange multipliers dealing with the contact and plasticity problems are not applicable. As far as numerical results are concerned, in this model, we mainly used Hilber-Hughes-Taylor-Newmark implicit schemes for the time discretization of the problem. The Hilber-Hughes-Taylor (HHT) operator is an extension of the Newmark beta-method. Numerical parameters associated with the HHT operator are tuned differently for moderate dissipation and transient fidelity applications. The backward Euler explicit operator is used by default if the application classification is quasi-static. These time integration operators

are implicit, which means the operator matrix must be inverted and a set of simultaneous nonlinear dynamic equilibrium equations must be solved at each time increment. This solution is done iteratively using Newton's method. It is an interesting scheme since it is energy-conserving on the linear part (elasticity's equations without constraint), but, of course, any other stable scheme can be applied. Let us recall that the use of an explicit (Euler centre differences) method requires impractically small time steps to keep the error acceptable in the result. Moreover the treatment of frictional contact and plasticity's conditions may lead to an ill-posedness of the fully explicit discrete problem whatever the length of the time step is. That is why we impose $\alpha=0$ in the HHT scheme, and then we used a classical Newmark scheme. (See Appendix 2)

The inequalities of the dynamic contact problem and plasticity problem are solved thanks to Lagrange multipliers [54][55]. For the dynamic contact problem we use one multiplier for the non-penetration normal condition, and one other for the standard μ -Coulomb's friction law without penalization nor regularization of the tangential stress with respect to the tangential velocity component. Meanwhile, there is one multiplier for the plasticity problem. The fact that the Lagrange multipliers are under different constraints leads to practical difficulties for the numerical resolution. This is one of the reasons why augmented Lagrangian ("generalized Newton's method") are considered, following the pioneering work of P. Alart and A. Curnier [67].

2.2.3 Simulation protocol and parameters

According to the previous researches, the corrugation defect is mainly highlighted while wheel-rail contact undergoes transient conditions such as braking or acceleration[1][22]. In a braking or acceleration process, the global slip ratio between the wheel-rail contact is inferior to 10%. To highlight the influence of transient conditions on corrugation development, the slip ratio is defined as high as 20% in the 2D-FEM wheel-rail contact dynamic model and the

time to apply the slip ratio is define as 0.1ms which is much shorter than the acceleration/braking time. The instability states are characterized as the consequence of the sliding velocity imposed, shear stress at the contact and impacts. In order to study the wheel-rail contact instability in transient conditions, the global stiffness and the train-track system are not considered in this study.

Sliding conditions are imposed through an increase of the angular velocity ω_{wheel} at the centre of the disc while the translating velocity V_{wheel} remains constant. The resulting imposed global sliding ratio Γ is calculated as followed:

$$\Gamma = \frac{|R^{\text{wheel}} \omega^{\text{wheel}} - V|}{V}$$

The simulation process includes two main steps: the step with no transient conditions applied and the step with transient conditions applied. The latter step is the most important to reproduce corrugation.

In the step with no transient conditions applied, the wheel is rolling in a constant velocity while a constant value of normal load is progressively applied in the centre of the wheel. The model assures that the wheel is in pure rolling state, and that the whole system gets through with stability. This is why this step is called “stability step”.

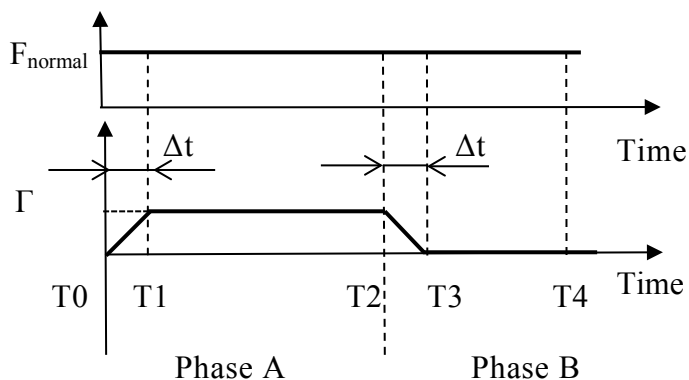


Figure 2.5 Evolution of normal load F_{normal} and global sliding ratio Γ imposed at the centre of the wheel

In the step with transient conditions applied, see Fig.2.5, the simulation protocol shows the evolution of the global contact condition, and this step, with transient conditions applied, is divided into two parts:

At the beginning of this step $t=T_0$, the wheel rolls without sliding on the rail with a constant linear velocity $V=R_{\text{wheel}} \omega_{\text{wheel}}=17\text{m/s}$, then the angular velocity ω_{wheel} imposed at the centre of the wheel is increased within a time period Δt $[T_0, T_1]$, to create the global sliding conditions between the wheel-rail contact. The first part is defined as Phase A $[T_0, T_2]$.

The second part is defined as Phase B $[T_2, T_4]$. The slip ratio Γ is maintained constant until $t=T_2$. Then, the sliding conditions are removed quickly, which leads to return to pure rolling conditions.

These two parts are also called “instability steps”. The simulation parameters are shown in Table 2.2.

Normal load at the centre of the disc, F_{normal} (N)	8000
Global sliding ratio, Γ	20%
Transient time to apply sliding condition, Δt (s)	0.1^E-3
Coulomb friction coefficient, μ	0.3

Table 2.2 The simulation parameters

2.3 Numerical tools to study the local wheel-rail contact dynamics: the indication of convergence

2.3.1 Definition of the contact force and the frictional power

In order to highlight instability states occurring in the contact patch, the temporal evolution of the global tangential contact force F_{tang}^G , which is the sum of all the local tangential contact force $F_{\text{tang}}^{\text{node}(i)}$ at the contact surface:

$$F_{\tan g}^G = \sum_i F_{\tan g}^{node(i)}$$

The numerical tool of the local frictional power $P_f^{node(i)}$ at each node(i) of the contact patch is used [36]. This can also help to determine whether or not the oscillatory state leads to surface degradation:

$$P_f^{node(i)} = \sigma_{shear}^{node(i)} S_{contact}^{node(i)} V_{sliding}^{node(i)} = V_{sliding}^{node(i)} F_{\tan g}^{node(i)}$$

With $S_{contact}^{node(i)}$ being the elementary surface around each node(i) equal to the product of the unitary thickness of the wheel with the node spacing in the contact patch, $\sigma_{shear}^{node(i)}$ is shear stress at each node(i) and $V_{sliding}^{node(i)}$ is the local relative sliding velocity between the wheel and the rail at node(i) in the contact patch.

The sum of all $P_f^{node(i)}$ at each node(i) of the contact is equivalent to the classical global frictional power P_f^G [4][6]:

$$P_f^G = F_{\tan g}^G V_{sliding}^G = \sum_i P_f^{node(i)}$$

With $|V_{sliding}^G| = \Gamma |V|$ being the global relative sliding velocity between the rail and wheel.

2.3.2 Definition of the contact status

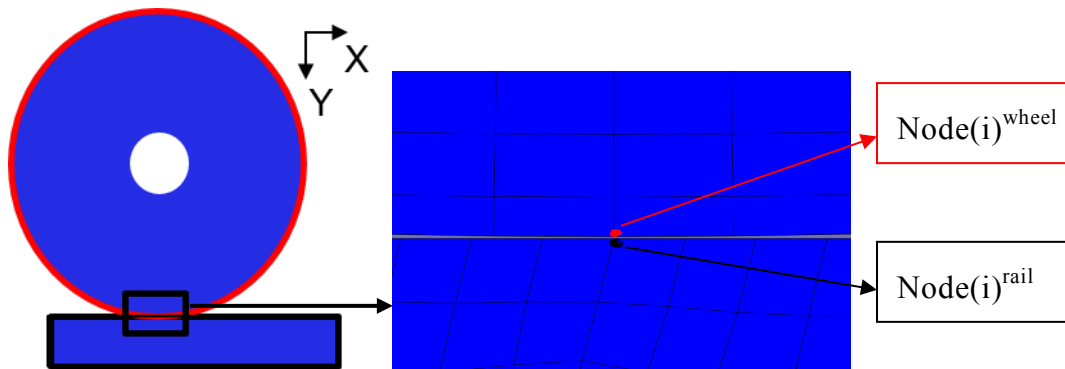


Figure 2.6 Nodes in wheel-rail contact surfaces

The variable of contact status describes whether individual nodes on the wheel and rail surfaces are in contact or not; and if so, whether the surfaces are sticking or slipping at that point. The goal is to compare the velocity in the node(i)^{wheel} and the node(i)^{rail} : if the velocity is different between the contact nodes, the surface is slipping at this node; if the velocity is the same between the contact nodes, the surface is sticking at this node. This approach helps to understand the local contact status within the instability states.

2.4 Convergence tendency of numerical model

Before studying the evolution of local contact dynamic problems in 2D-wheel-rail model under transient conditions, the influence of the elements' size and of different integration time steps have to be found out to get the model valid.

The following simulations are made with a 2D-FEM model constituted in Abaqus; 2D-stress 4-node linear plane strain quadrilateral element and structural meshes are used. The time integration code uses Hilber-Hughes-Taylor implicit schemes and the initial time stepping increment is 1e-5 s. The parameters of wheel-rail contact model, material property and the simulation protocol are described in Tables 2.1 and 2.2. The first results are listed as followed: contact shear force (CSF), normal force (CNF), global frictional power (P_f^G), etc...

To get a balance between a better presentation of the model and a less computational cost, the results obtained in the simulations will be compared. The subject is to study the rail-wheel contact, and a more compressed mesh is expected on the contact surface. Therefore, the following table (Table 2.3) is a comparison of different mesh sizes in the contact area.

Mesh	Total elements number (wheel+rail)	Elements' size at the contact area(mm)	Relative CPU time
M1	30,631	1.0*1.0	0.2
M2	70,168	0.4*0.4	0.3
M3	108,703	0.2*0.2	0.7
M4	171,342	0.1*0.1	1.0

Table 2.3 Characteristics of different meshes in the 2D-wheel-rail model

According to the results calculated with different mesh sizes (Table 2.4), values such as contact shear force (CSF), normal force (CNF), global frictional power (P_f^G), etc... show great differences between M1 and M2, comparing to M4, while results show little differences between meshes M3 and M4. With smaller mesh sizes in the 2D-model, the results seem to be more accurate but CPU time cost is also more important.

Mesh	CSF	CNF	V_{slid}	P_f^G	CPRESS	PEEQ
M1-M4	10%	8%	16%	18%	45%	50%
M2-M4	8%	7%	15%	15%	40%	42%
M3-M4	5%	5%	5%	4%	5%	5%

Table 2.4 Comparison of the results with different mesh sizes

In the meantime, the convergence tendency of the model is observed with different increment times and different mesh sizes in the contact area. Table 2.5 shows us that the model could be completed with very small time increment, which means that the model using automatic time integration (at the range of $\Delta t_{min} = 1e-7s$ and $\Delta t_{max} = 1e-4s$) needs a smaller computational cost for simula-

tion. So, the mesh type M4 using automatic time increment is satisfying, with accuracy and less consumption of computing time. Finally, the mesh type M4 is chosen to do the numerical analysis.

Mesh	$\Delta t_1(1e-5 \text{ s})$	$\Delta t_2(1e-6 \text{ s})$	$\Delta t_3(1e-7 \text{ s})$	Δt_{auto}
M1	√	√	√	√
M2	√	√	√	√
M3	√	√	√	√
M4	×	√	√	√

× Calculation aborted

√ Calculation completed

Table 2.5 Different time increments influence on the model convergence tendency

2.5 Conclusion

In this part, a simplified 2D-finite element model is constituted to analyse the wheel-rail contact dynamic problem. A proper simulation protocol is chosen to apply the transient conditions in the wheel-rail contact and to study the wheel-rail contact instabilities. The numerical tools are described to help understand the local contact dynamics between wheel and rail. And thanks to the study of the influence of different mesh sizes and integration times on the model convergence tendency, an available mesh type and integration scheme is selected for the following simulation. Therefore, in the next part, the raising process and the evolution of corrugation defect under transient conditions will be represented by the transient parameters studies, etc....

Part 2 Investigation on the origin and the evolution of straight-track corrugation under transient conditions

Chapter 3. Parametric sensibility of corrugation birth under transient conditions with single wheel passing

According to the bibliographic studies (see chapter 1), the corrugation defect is becoming a severe problem that usually appears under transient conditions such as braking/accelerating. To better understand the origin of this defect, a 2D-FEM wheel-rail contact dynamic model was constituted. A simulation protocol (see Fig. 2.5) is defined to represent the transient conditions in the wheel-rail contact model. In the following work, we expect to reproduce the birth of corrugation defect under transient conditions and to study the influence of parameters on the corrugation defect.

3.1 Characterization of the instability states under transient conditions

3.1.1 Characterization of the contact status

Using the simulation protocol in Figure 2.5 and the parameters in Tables 2.1 and 2.2, two phases are distinguished according to the simulation results:

At first, in the so-called Phase A $[T_0, T_2]$ (see chapter 2.2), the slip ratio Γ imposed at the centre of the wheel is increased within a time period $\Delta t [T_0, T_1]$, to create the global sliding conditions between the wheel-rail contact. According to the observation of the wheel behaviour during this phase (0-0.01 s), we can see that all the nodes in the contact patch are in the sliding status (see Fig. 3.1). This is why this phase is called “slip state”.

Secondly, in Phase B $[T_2, T_4]$ (see chapter 2.2), the slip ratio Γ is removed within the same period $\Delta t [T_2, T_3]$, which leads the wheel to return to pure

rolling conditions. The results show that nodes in wheel-rail contact switched between sliding status and sticking status (0.01-0.02s). Therefore, this phase is called “stick-slip state”.

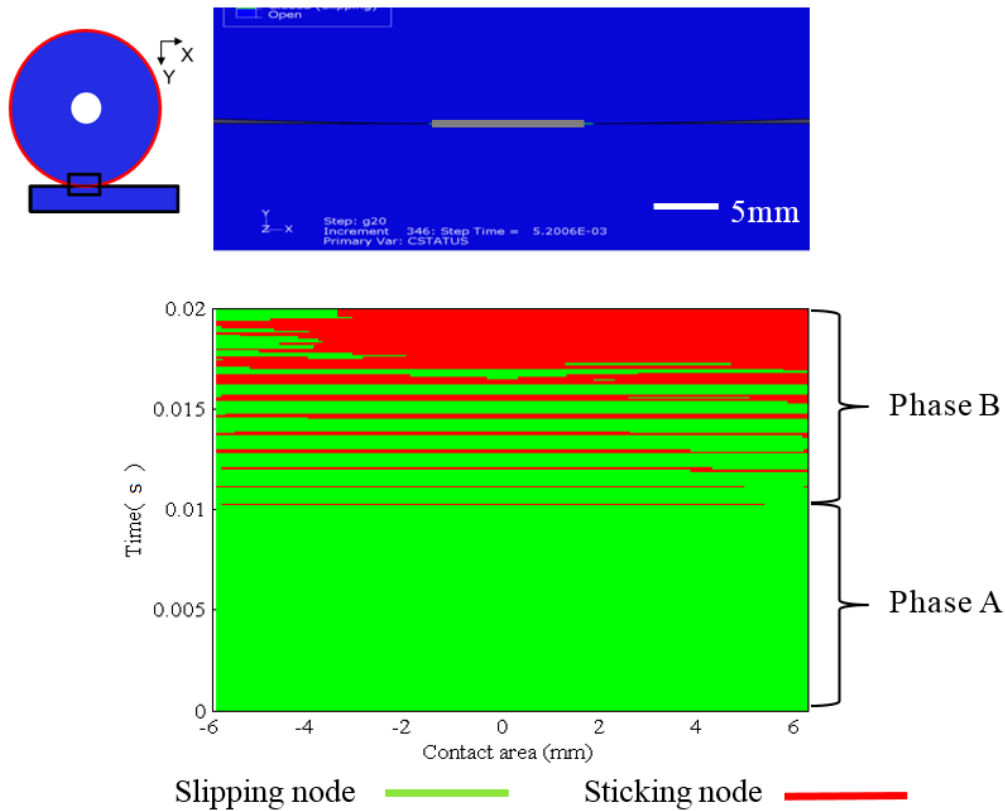


Figure 3.1 Evolution of contact status

3.1.2 Characterization of the frequency in modal analysis

Modal analysis is applied to measure and analyse the dynamic response of wheel-rail contact model. Since contact status in the phase A is in fully sliding state, the first modal analysis (see Fig.3.2) deals with a free wheel constrained only through its centre. The natural frequencies of the free wheel $f_{free}^{1st-mode}$ were 558 Hz, and the shape of this mode is a classical torsional movement of the wheel around its centre.

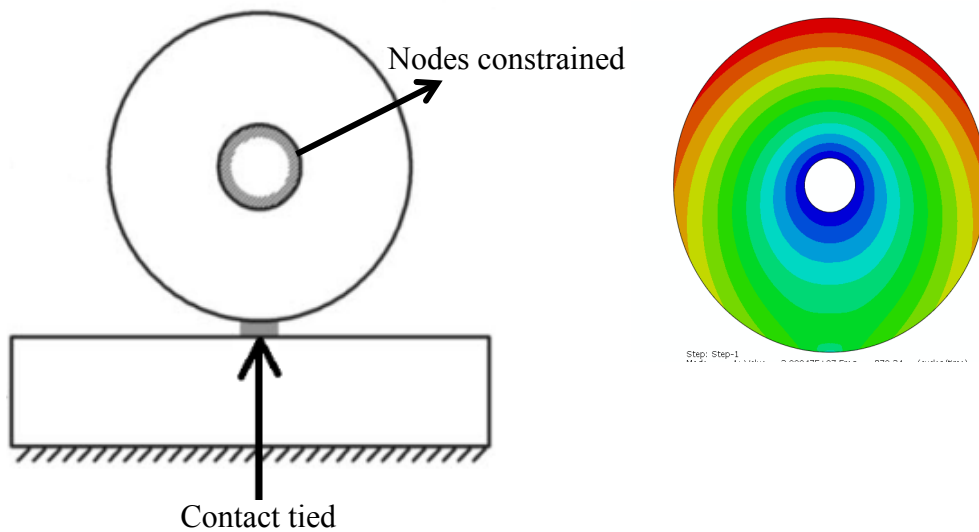


Figure 3.2 Modal analysis of a free wheel model and its first natural mode result

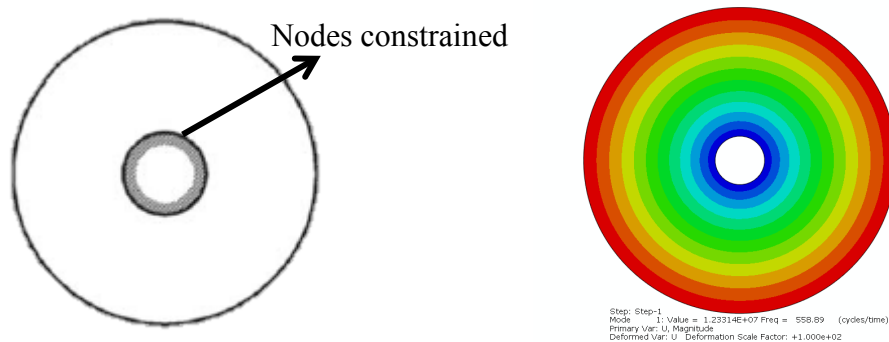


Figure 3.3 Modal analysis of a couple wheel-rail model and its first natural mode result

As the local contact conditions during phase B were characterized by the coexistence of both sticking and sliding areas, the wheel and rail were coupled for the modal analysis. Consequently, the nodes at the contact area were tied together to represent the sticking conditions in the contact patch (see Fig.3.3). Whereas the first mode had a frequency $f_{\text{coupled}}^{\text{1st-mode}} = 810 \text{ Hz}$, the shape of this mode remained a torsional movement of the wheel around its centre though

perturbed by the tied contact conditions imposed at the interface between the two bodies.

3.1.3 Characterization of the wheel-rail local contact dynamics

Thanks to the results obtained in the simulation, two phases can be distinguished according to the evolution of global tangential contact force F_{tang}^G (see Fig.3.4 (a)). In slip state Phase A (from T_0 to T_2), F_{tang}^G increases to reach the maximum value of 2400N which is function of the constant Coulomb friction coefficient μ , in this case equal to 0.3, and the normal force F_{normal} of 8000N. The instability state has a frequency of 527Hz, which corresponds to the frequency of the first torsional mode of a free wheel. According to the comparison between the shape of the mode and the behaviour of the wheel during this state, the behaviour of the wheel during Phase A shows that frequency of the slip oscillatory state is fixed by the frequency of the first natural mode of the free wheel. While in Phase B (for $t > T_2$), when the slip ratio is removed from the wheel, F_{tang}^G oscillates with a frequency of 743Hz decreasing to a minimum value around zero. The nodes in contact switch between sliding status and sticking status, while the frequency of the first mode of coupled wheel-rail model turns out to be 870Hz; the difference between the simulation results and the modal analysis during stick-slip oscillatory state is caused by the nodes in the contact which are not all adhering to the surface.

The global frictional power P_f^G for the slip state is present in Fig. 3.4(b). Result shows high oscillations with a frequency identical to F_{tang}^G (see Fig. 3.4(a)). The mean value of $P_f^G = 8000\text{W}$ is very close to the theoretical global frictional power $P_{f\text{ theory}}^G = F_{\text{tang theory}}^G * V_{\text{sliding}} = 8160\text{W}$ which is due to the theoretical maximum tangential contact force, and sliding velocity imposed at the centre of the wheel. In Phase B, the consecutive frictional power quickly reaches zero (see Fig. 3.4(b)); the stick-slip oscillatory state is not as energetic as the slip oscillatory state.

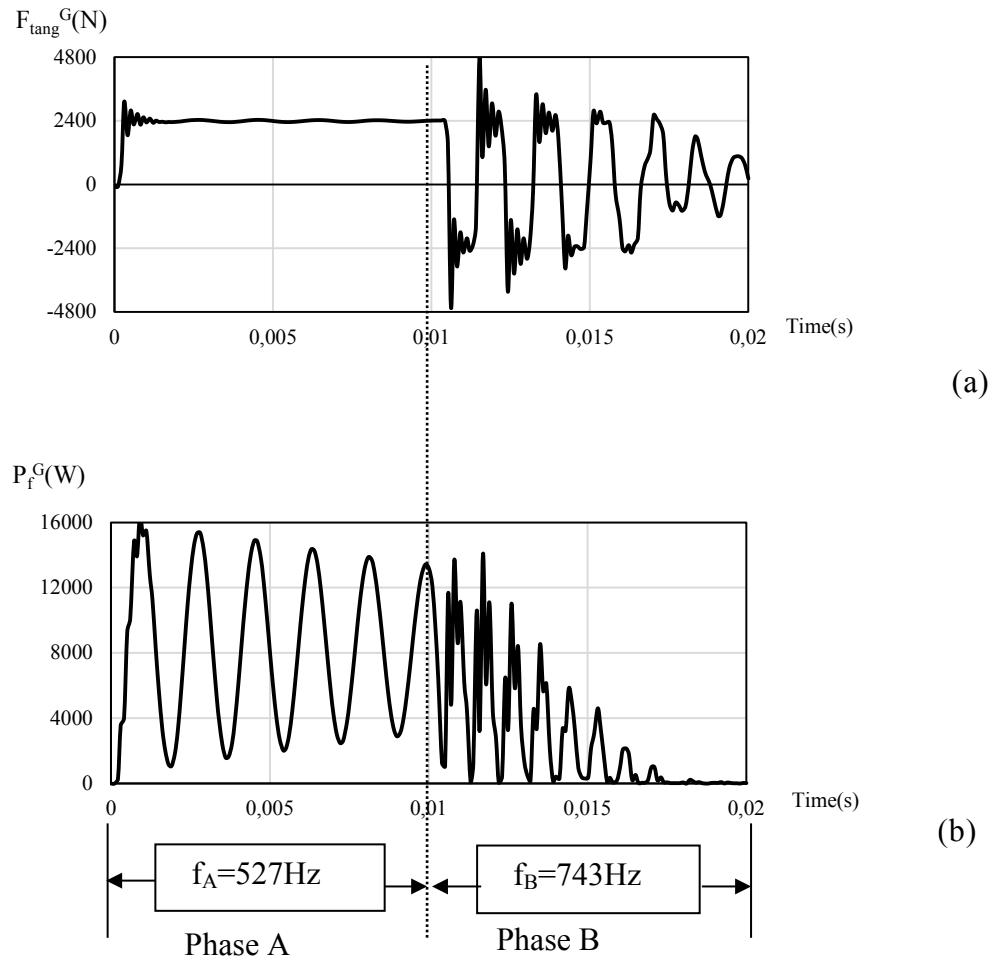


Figure 3.4 Evolution of (a) global tangential contact force F_{tang}^G and (b) global frictional power P_f^G

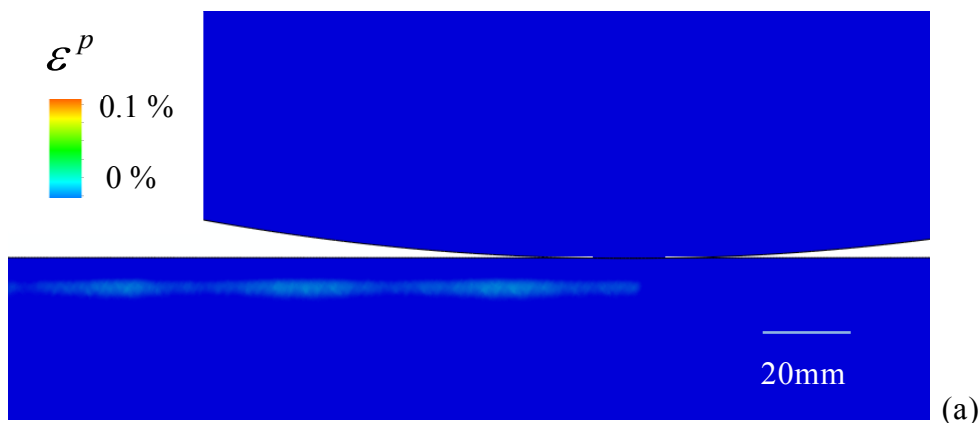
3.1.4 Characterization of the plastic flow in the birth of corrugation defect

In the step with no transient conditions applied, the wheel rolls without sliding on the surface of the rail. Figure 3.5(a) shows that nearly null plastic deformation (about 0.009%) occurs. While transient conditions are applied, slip instability state occurs. In Phase A, periodical plastic deformations are high-

lighted on the rail surface (see Fig. 3.5(b)) with a wavelength of $\lambda_A=30\text{mm}$. And the maximum plastic deformation reaches about 0.1%. The plastic deformation is produced consecutively as the transient velocity oscillates in the contact path. During Phase B (stick-slip oscillatory state, see Fig. 3.5(c)), the periodical deformation is more obvious, maximum deformation reaches about 0.16%, and the wavelength λ_B is about 23mm.

According to the results obtained in Phases A and B, the consequence of the periodical plastic deformation is the formation of a waviness in the rail, which appears not only on the contact surface but also inside the rail. And the plastic deformation is produced as the transient velocity oscillates in the contact path.

The wavelengths of these two phases correspond to the frequency of the two oscillatory states $f_A=527\text{Hz}$, $f_B=743\text{Hz}$ as a function of the translating velocity $V=17000\text{mm/s}$. Compared with the undeformed rail head under pure rolling step (Fig. 3.5(a)), the periodical plastic deformations in Phases A and B (Fig.3.5 (b) and 3.5 (c)) show that the consequence of transient conditions is the reason why the rail deforms periodically. The simulation results (see Fig.3.4, Fig.3.5) match the previous work performed with a laboratory FEM code PlastD in Saulot's thesis [61].



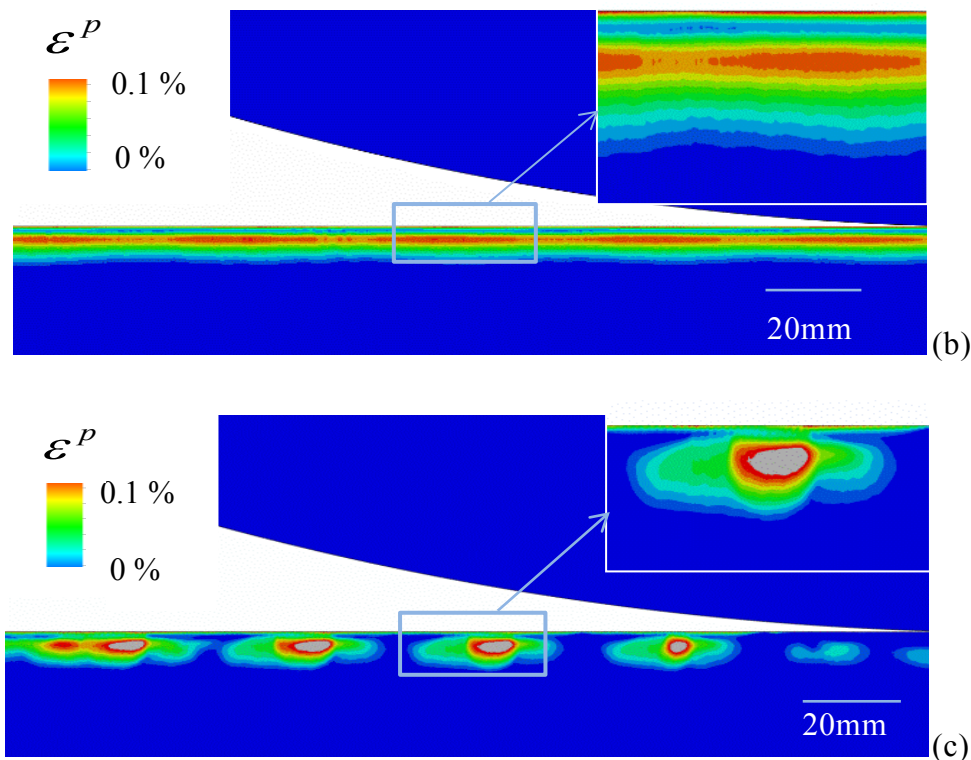


Figure 3.5 Periodical Plastic deformation of (a) pure rolling state, (b) Phase A: slip state and (c) Phase B: stick-slip state in 20% sliding rate with friction coefficient 0.3 in 2D model

3.2 Consequence of corrugation with different parameters applied under transient conditions

The first result obtained in the previous section shows two instability states investigated under transient conditions. The slip ratio Γ imposed in transient time increment is believed to influence the instability states. For the following study, normal load F is kept equal to 8 kN, the influence of different parameters such as slip ratio Γ (from 1% to 20%), transient time for applying sliding conditions Δt (from 0.1ms to 5ms), and Coulomb's friction coefficient μ (from 0.1-0.5) will be investigated in the oscillatory states. The sensibility of corrugation defect will be studied through different parameters under transient conditions.

3.2.1 Influence of different slip ratios Γ

At first, the parameter studied deals with the influence of different slip ratios Γ . Three different values of Γ were chosen: 20%, 5%, and 1%. Figure 3.6 presents the temporal evolution of the global tangential force F_{tang}^G and of the global frictional power P_f^G for three sliding ratios Γ imposed (20%, 5% and 1%). The figure shows that, at the begin of the transient phase in which the wheel is running under pure rolling conditions, the global tangential force F_{tang}^G and the global frictional power P_f^G are equal to zero.

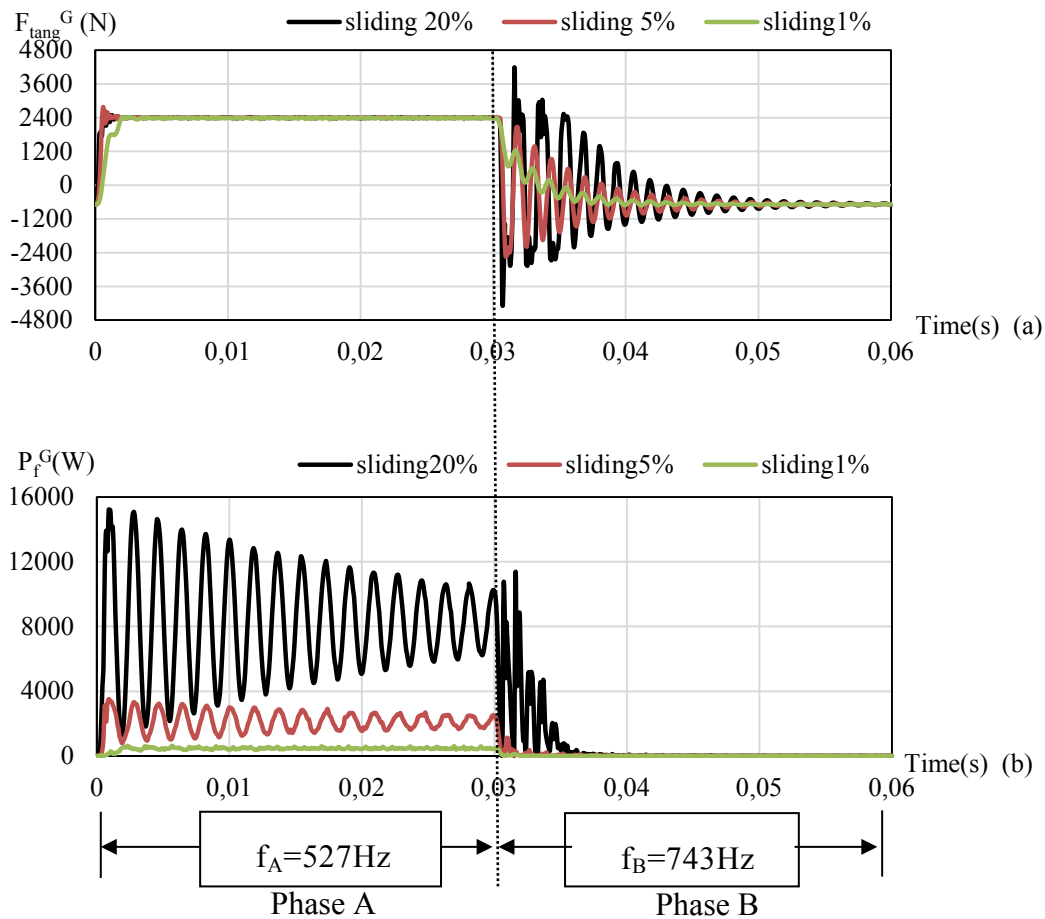


Figure 3.6 Influence of different slip ratios Γ on the evolution of (a) global tangential contact force F_{tang}^G and (b) global frictional power P_f^G

Highlighted by the temporal evolution of P_f^G along Phase A (Fig. 3.6(b)), the slip oscillatory state remains with the same frequency f_A whatever the sliding ratio is. The consequences of a decrease of the sliding ratio are twofold. On the one hand, both the mean values and the amplitude of P_f^G fluctuations decrease, while on the other hand, P_f^G delayed its increase at the beginning of Phase A. Indeed, since the sliding ratio is lower, the system needs more time to accumulate enough torsional energy to counterbalance the energy required to reach sliding conditions as a function of the normal load and friction coefficient. Highlighted by the temporal evolution of F_{tang}^G along Phase B (Fig. 3.6(a)), the stick-slip oscillatory state also remains and its frequency f_B does not change. Decreasing slip ratio Γ lowers the amplitude of the oscillations and modifies the evolution of their mean value when too small (e.g., 1%). In this latter case, the system slowly releases the torsional energy accumulated during Phase A.

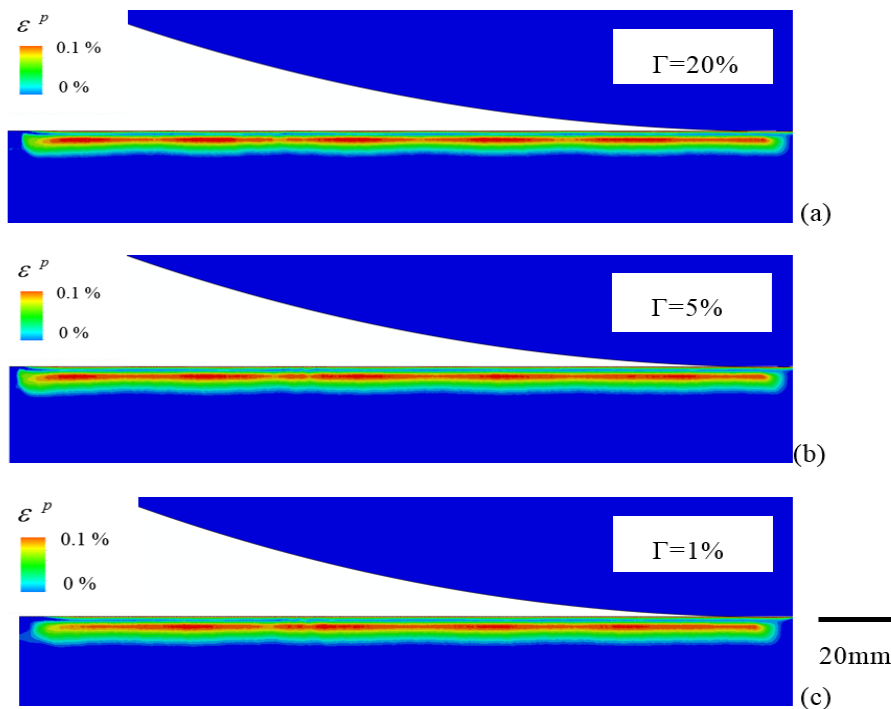


Figure 3.7 Influence of different slip ratios Γ on the evolution of plastic deformation in the rail under slip instability state (Phase A)

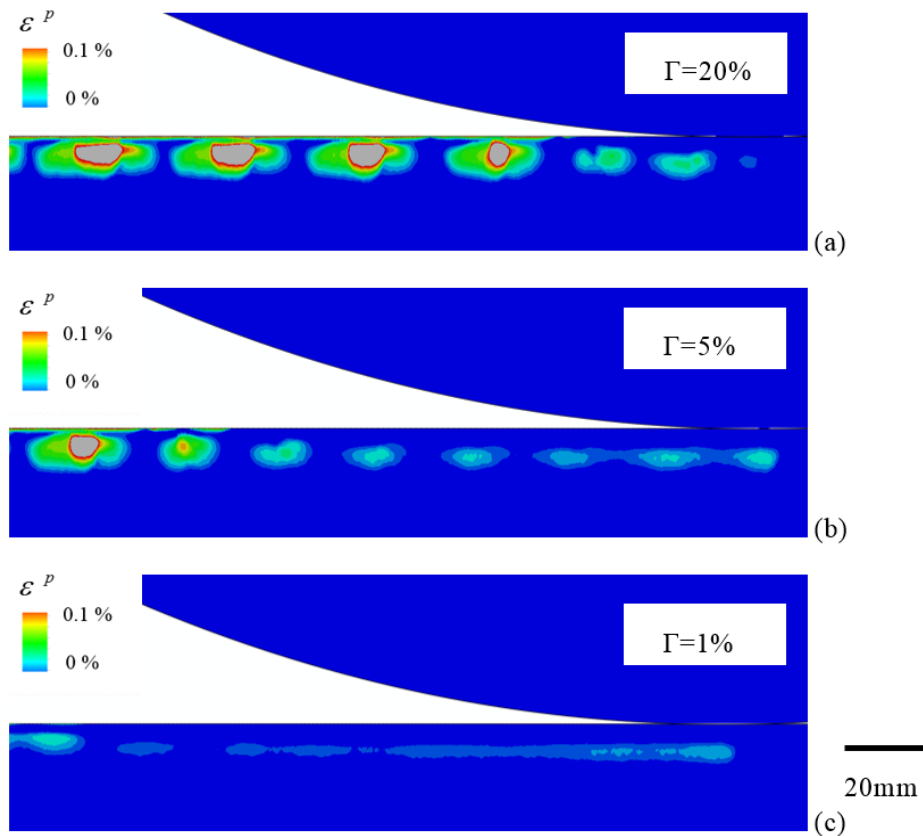


Figure 3.8 Influence of different slip ratios Γ on the evolution of plastic deformation in the rail under slip-stick instability state (Phase B)

According to the evolution of plastic deformation obtained in Phase A (see Fig.3.7), the plastic flow of the material does not show much difference within the different slip ratios Γ . Both the wavelength and peak value of plastic deformation are presented similarly.

The results shown in Phase B (see Fig.3.8) differ from the different slip ratios Γ . As the slip ratio Γ decreases from the 20% to 1%, the plastic deformation seems to get lower and lower. We cannot observe the periodical deformation with $\Gamma=1\%$ in this phase.

From the results obtained in both Phase A and Phase B, it could be concluded that the slip instability state is the main state that causes the birth of corrugation defect. The different slip ratios do not affect this defect in slip state, while

the evolution of the corrugation defect in the slip-stick state is more sensitive to the slip ratio Γ .

3.2.2 Influence of different Coulomb's friction coefficients μ

The same simulation protocol was used again for the study, except for the sliding ratio Γ chosen as 20%, transient time Δt chosen as 0.1ms. The influence on the oscillatory states of three friction coefficients μ (0.1, 0.3 and 0.5) was studied.

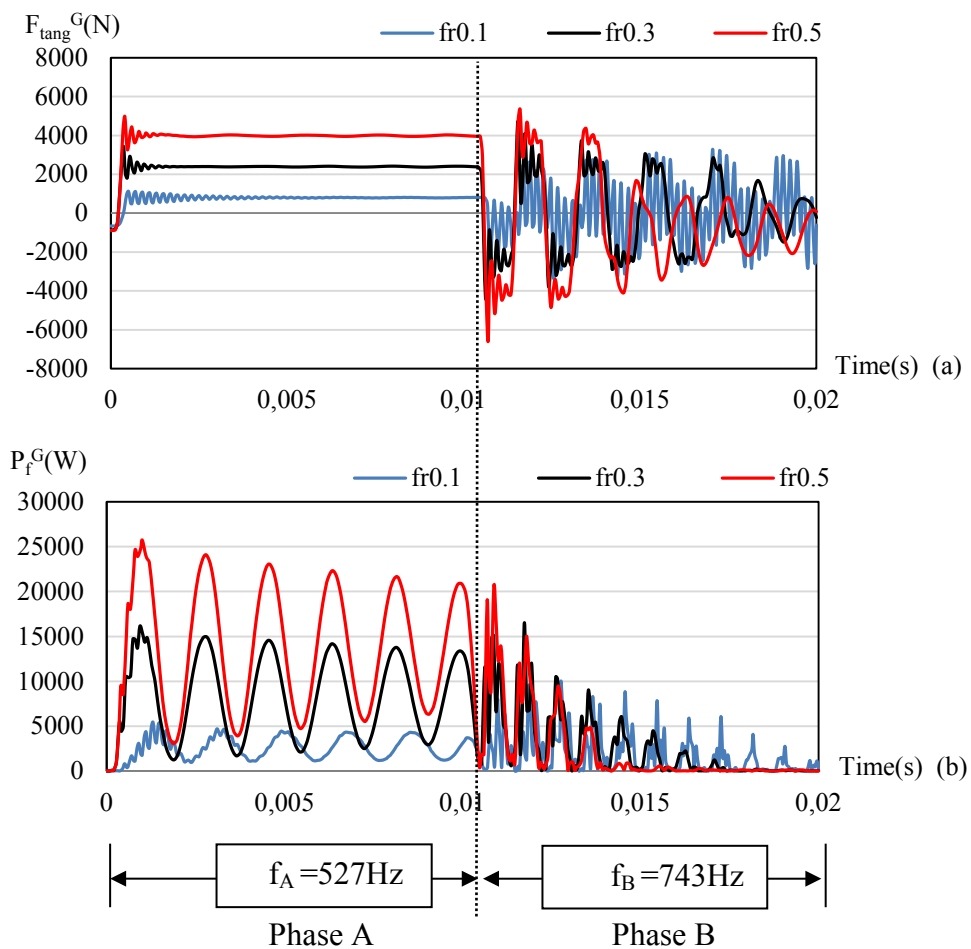


Figure 3.9 Influence of different friction coefficients on the evolution of (a) global tangential contact force F_{tang}^G and (b) global frictional power P_f^G

For the slip oscillatory state, the higher the friction coefficient was, the higher the mean value and the amplitude of P_f^G fluctuations were (Fig. 3.9(b)). As for the stick-slip oscillatory state, the mean value of F_{tang}^G was always around zero (Fig. 3.9(a)), whereas the amplitude of its oscillations decreased with the friction coefficient. Furthermore, the frequency of the oscillatory states remained unchanged for each phase.

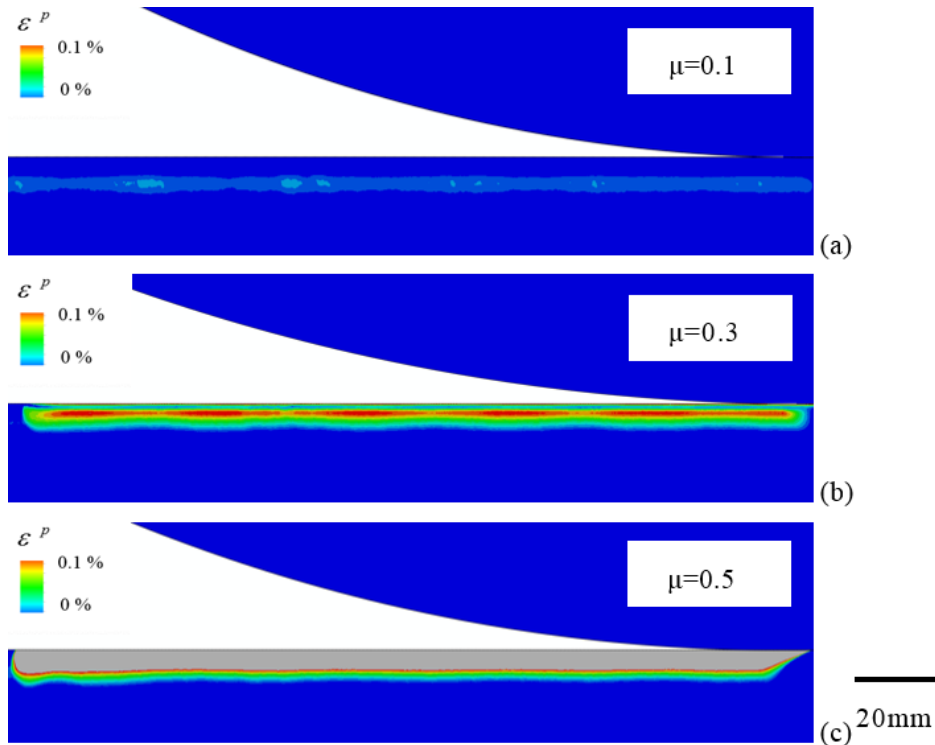


Figure 3.10 Influence of different friction coefficients μ on the evolution of plastic deformation in the rail under slip instability state (Phase A)

Since the frequencies of the instability states are kept unchanged with different friction coefficients μ , the wavelength of the plastic deformation is supposed to be fixed. The results obtained in Figures 3.10 and 3.11 show the plastic flow in both slip state and slip-stick state. With different friction coefficients μ imposed in the wheel-rail contact, the frictional force in the contact strongly affects the plastic deformation in rail (see Fig.3.10 and Fig.3.11). When friction coefficient μ is as small as 0.1, the plastic deformation ε^P is very weak as a

value of 0.01%; while when friction coefficient μ is increased to 0.5%, ε^P achieves a very high value of 1-2%.

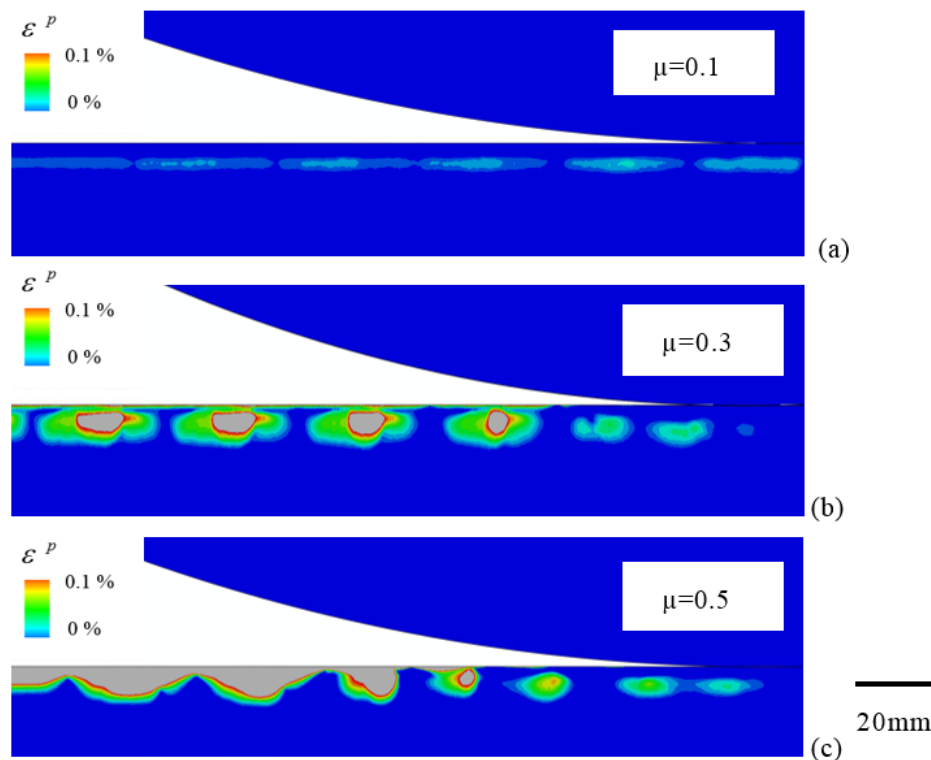


Figure 3.11 Influence of different friction coefficients μ on the evolution of plastic deformation in the rail under slip-stick instability state (Phase B)

The parametric study with different friction coefficients μ indicates that the friction force has a big influence on the corrugation defects in both slip state and slip-stick state.

3.2.3 Influence of different times Δt to apply transient conditions

To study the influence of the time increment on the instabilities, the following analysis uses different time durations ($\Delta t = 0.1\text{ms}$, 1ms , 5ms) to apply the wheel sliding ratio.

Results in Figure 3.12.(a) show that the time increment Δt increases from 0.1ms to 5ms , but the amplitude of F_{tang}^G is not affected in the two stability

states. The different tendencies of the tangential contact force raising to the maximum depend on the different time increments applied. And this effect is evident in global frictional power P_f^G (Fig. 3.12(b)): the system is more energetic with smaller time increment.

Naturally, we could expect that slip or stick-slip oscillatory state would not develop for very long transient values while applying sliding conditions (over 1 s).

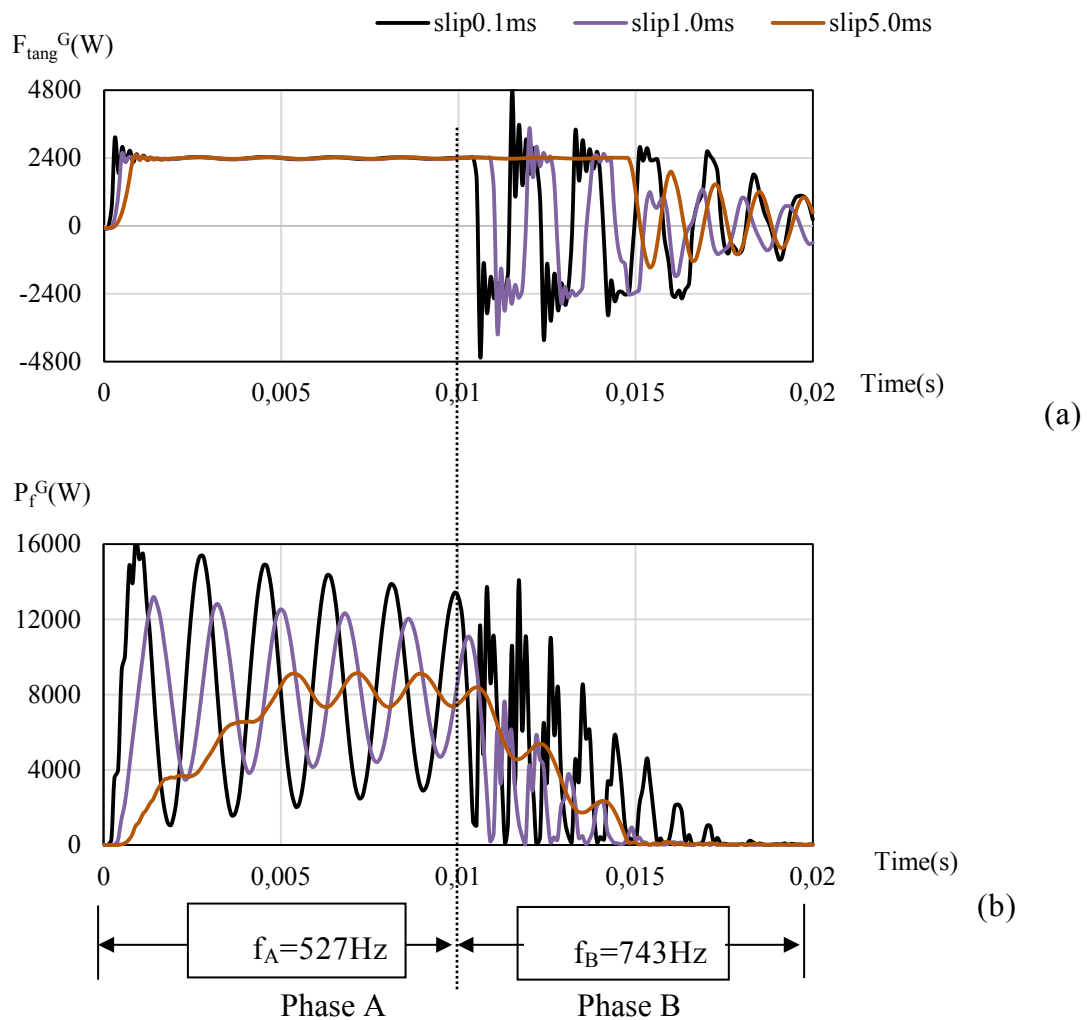


Figure 3.12 Influence of different time increments on the evolution of (a) global tangential contact force F_{tang}^G and (b) global frictional power P_f^G

The results in Phase A (see Fig.3.13) show the plastic deformation is not influenced by different time increments Δt . Same wavelength and amplitude are observed in slip instability state with different time increments Δt .

While in Phase B (see Fig.3.14), the plastic deformation develops more slowly and more constantly both in the surface of and inside the rail when the transient conditions are applied in larger time increment ($\Delta t=5\text{ms}$). And the different time increments Δt do not influence the amplitude of the elastic deformation.

Under transient conditions, the corrugation defect is more sensitive for the short time increment $\Delta t = 0.1\text{ms}$ comparing with $\Delta t = 5\text{ms}$.

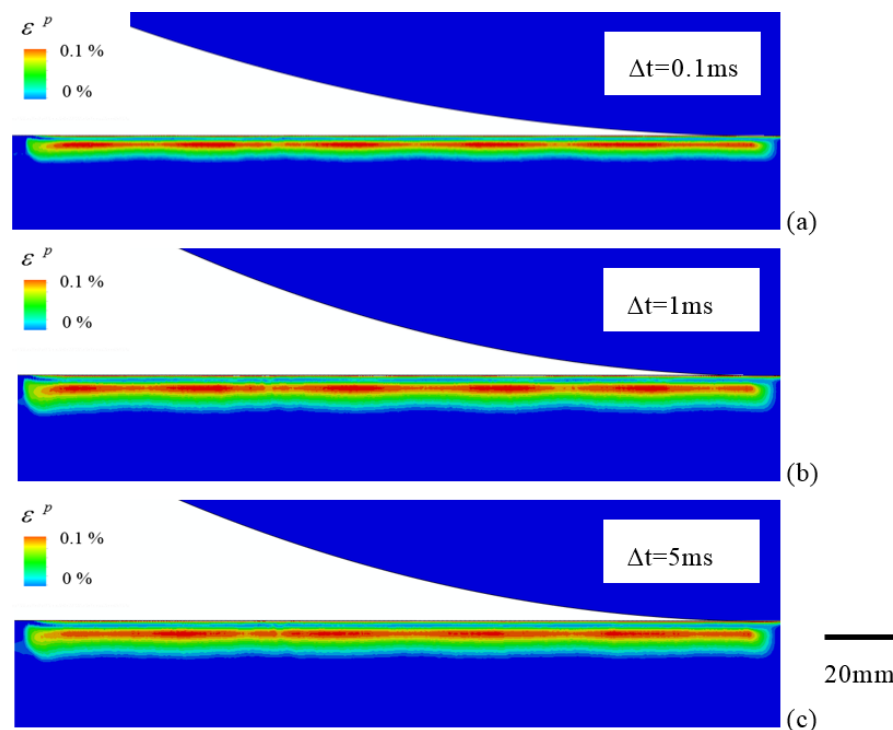


Figure 3.13 Influence of different times increments Δt on the evolution of plastic deformation in the rail under slip instability state (Phase A)

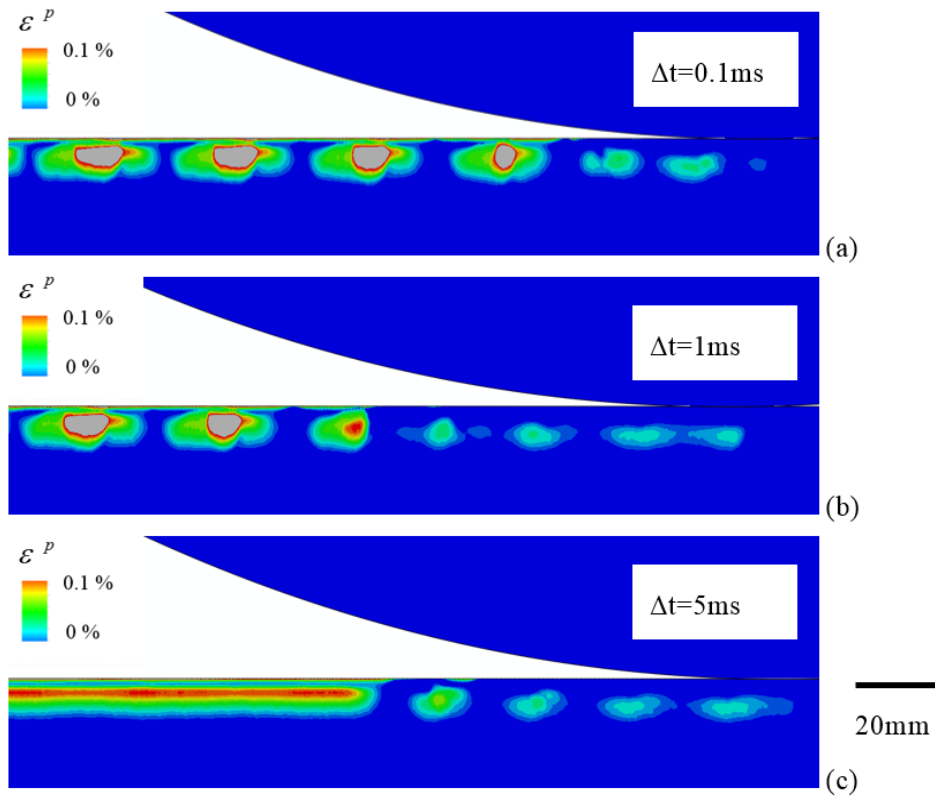


Figure 3.14 Influence of different transient times Δt on the evolution of plastic deformation in the rail under slip-stick instability state (Phase B)

3.2.4 Conclusion about the study of transient conditions parameters

These results obtained with different transient conditions parameters show that the birth of the plastic deformation depends on the transient conditions of the wheel behaviour. And thanks to the study of different slip ratios Γ , different friction coefficients μ and different time increments Δt , the sensibility of the corrugation defect is investigated.

3.3 Consequence of corrugation under different material laws

In the stress-strain curve of a material (see Fig.3.14), stresses beyond the elastic limit cause a material to yield or flow. For such materials, the elastic limit marks the end of elastic behaviour and the beginning of plastic behaviour.

In order to approach wheel-rail contact reality, the strain-stress curve is represented in the 2D-FEM wheel-rail contact model as the rail material uses a law of linear elasto-plastic with isotropic linear hardening properties: $\sigma_{ep}=455+250 \varepsilon^p$ (MPa) [68][10], with σ_{ep} being the equivalent plane stress and ε_p the equivalent plastic plane strain.

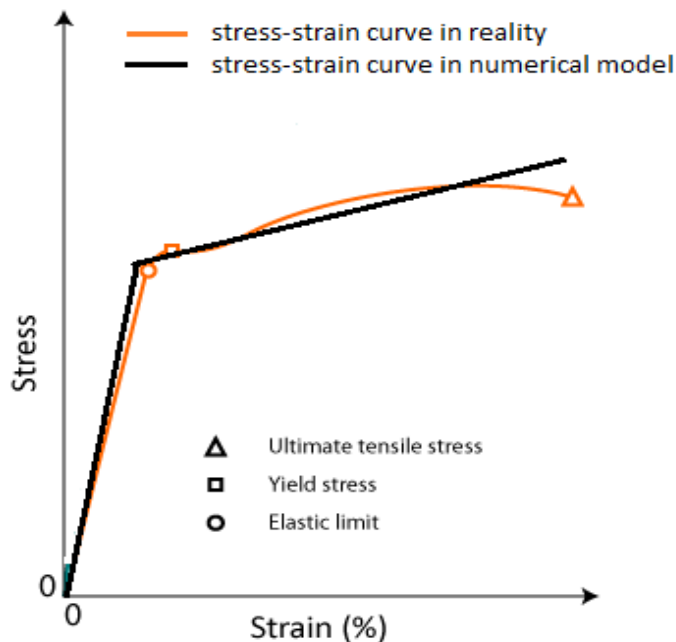


Figure 3.15 Strain-stress curve of steel[56]

As an initial definition, the elastic limit of rail material is set to 455MPa, and the strength index is set to 250MPa per 0.01% plastic deformation. To understand the influence of the material law on the evolution of corrugation defect, both the various values of elastic limit and the strength index will be studied.

3.3.1 Influence of different values of elastic limit

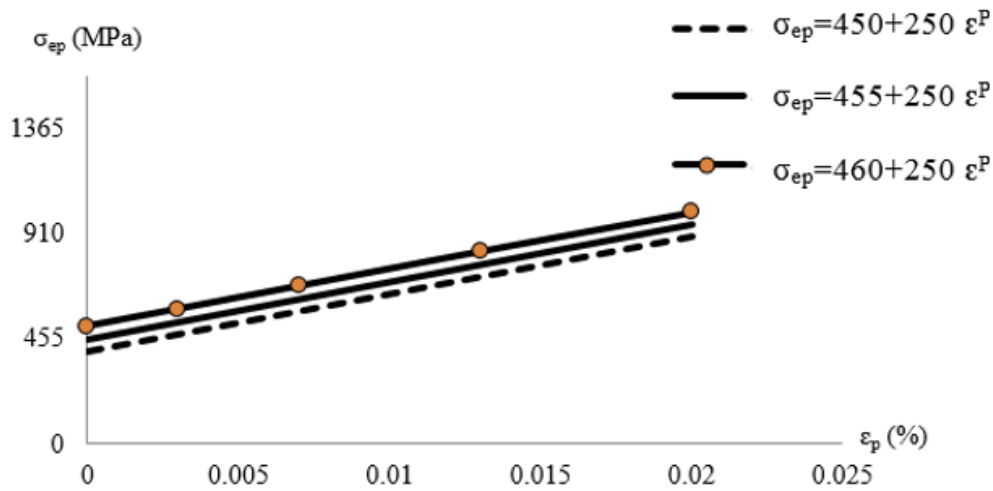


Figure 3.16 Different elastic limits of strain-stress curves

At first, the influence of different elastic limits will be studied. The wheel-rail model still uses the same protocol (see Fig. 2.5): load $F_{\text{normal}}=8\text{kN}$, slip ratio $\Gamma=20\%$ applied in transient conditions with $\Delta t=0.1\text{ms}$, which are the same parameters used in Tables 2.1 and 2.2. The different elastic limits are chosen with the values of 450MPa, 455MPa and 460MPa, which are in the range of steel yield stresses.

The evolutions of global tangential contact force F_{tang}^G (see Fig. 3.17(a)) and global frictional power P_f^G (see Fig. 3.17(b)) show that the elastic limit of the material does not affect the amplitude nor the frequency. The slip oscillatory state remains with the same frequency f_A and the slip-stick oscillatory state remains with the same frequency f_B .

The contact pressure only depends on the geometry of the contact bodies, the material property that includes the Young's modulus E , and the Poisson ratio γ , etc... So the contact force and sliding velocity are not influenced by the small variation of elastic limit (5MPa difference). Results obtained in Figure 3.17 show the gap between different elastic limits is inferior to 5%, and these re-

sults show the elastic limit has a very weak influence on the wheel-rail contact dynamics.

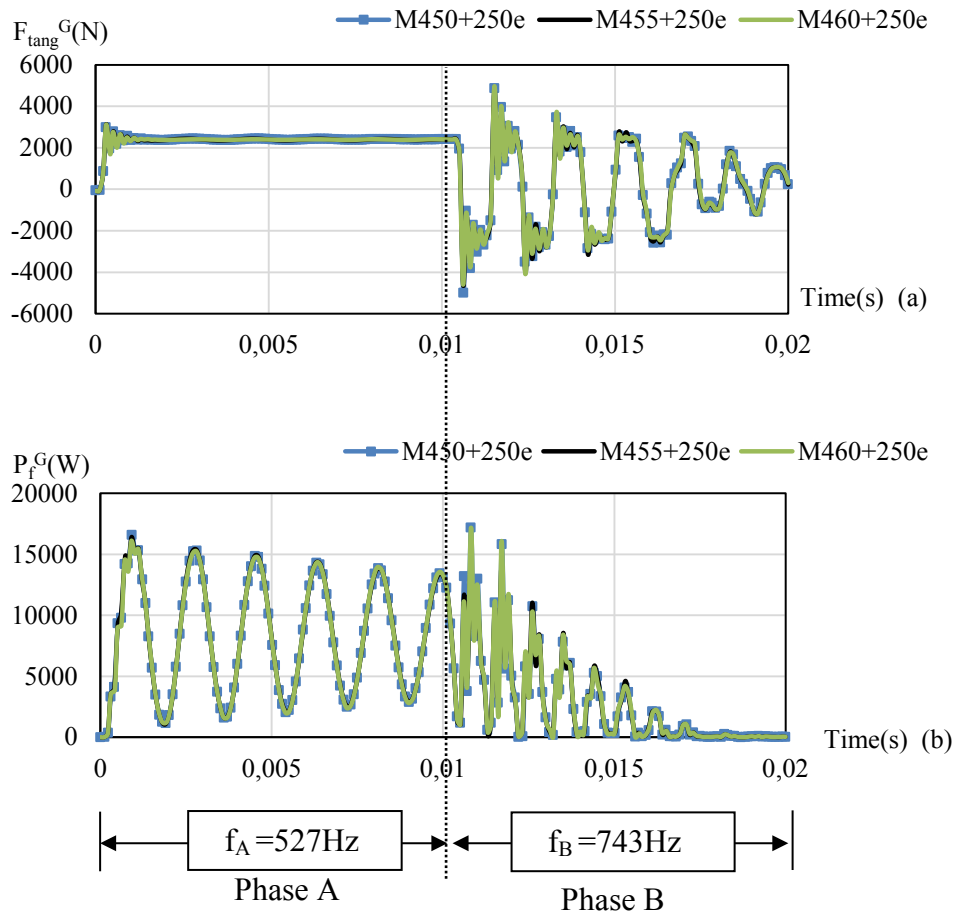


Figure 3.17 Influence of different elastic limits on the evolution of (a) global tangential contact force F_{tang}^G and (b) global frictional power P_f^G

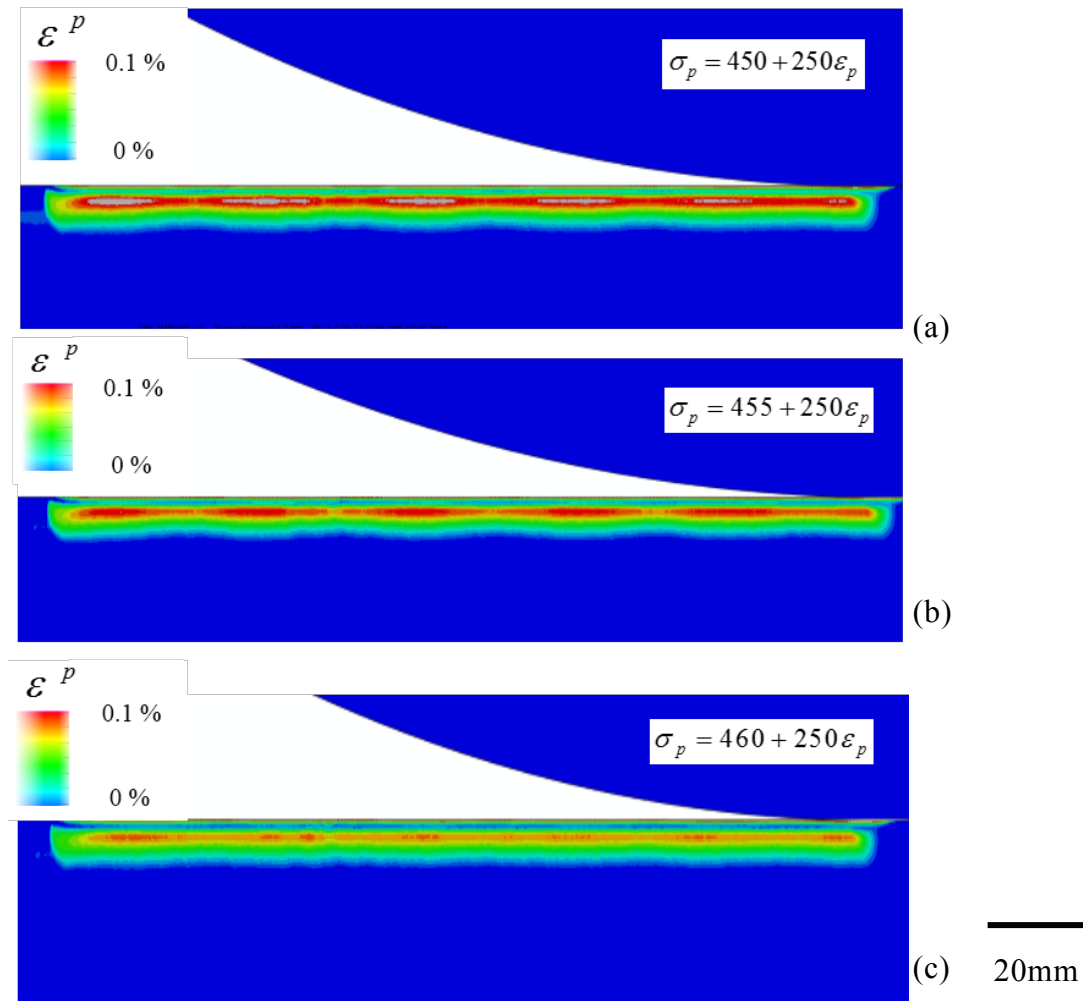


Figure 3.18 Influence of different elastic limits on the evolution of plastic deformation in the rail under slip instability state (Phase A)

Though the evolution of plastic deformation was influenced by the different elastic limits, the value does not much change. Figure 3.18 shows that, with the increase of elastic limit by 5 MPa, from 450MPa to 460MPa, the amplitude of the periodical plastic deformation has decreased from 0.12% to 0.8%. With the higher value of the elasticity limit, the deformation is less obvious. Same results are found in Phase B (slip-stick instability state): the plastic deformation is not significant if the elastic limit is high (460 MPa) (Fig. 3.19). It could be assumed that the regimes of instabilities have not enough energy to seek material in its plastic domain, if the elastic limit is high (such as 460MPa).

A small difference (5MPa) of elastic limit will lead to obvious change in plastic deformation. The corrugation defect is very sensitive to the small variations of the elastic limits.

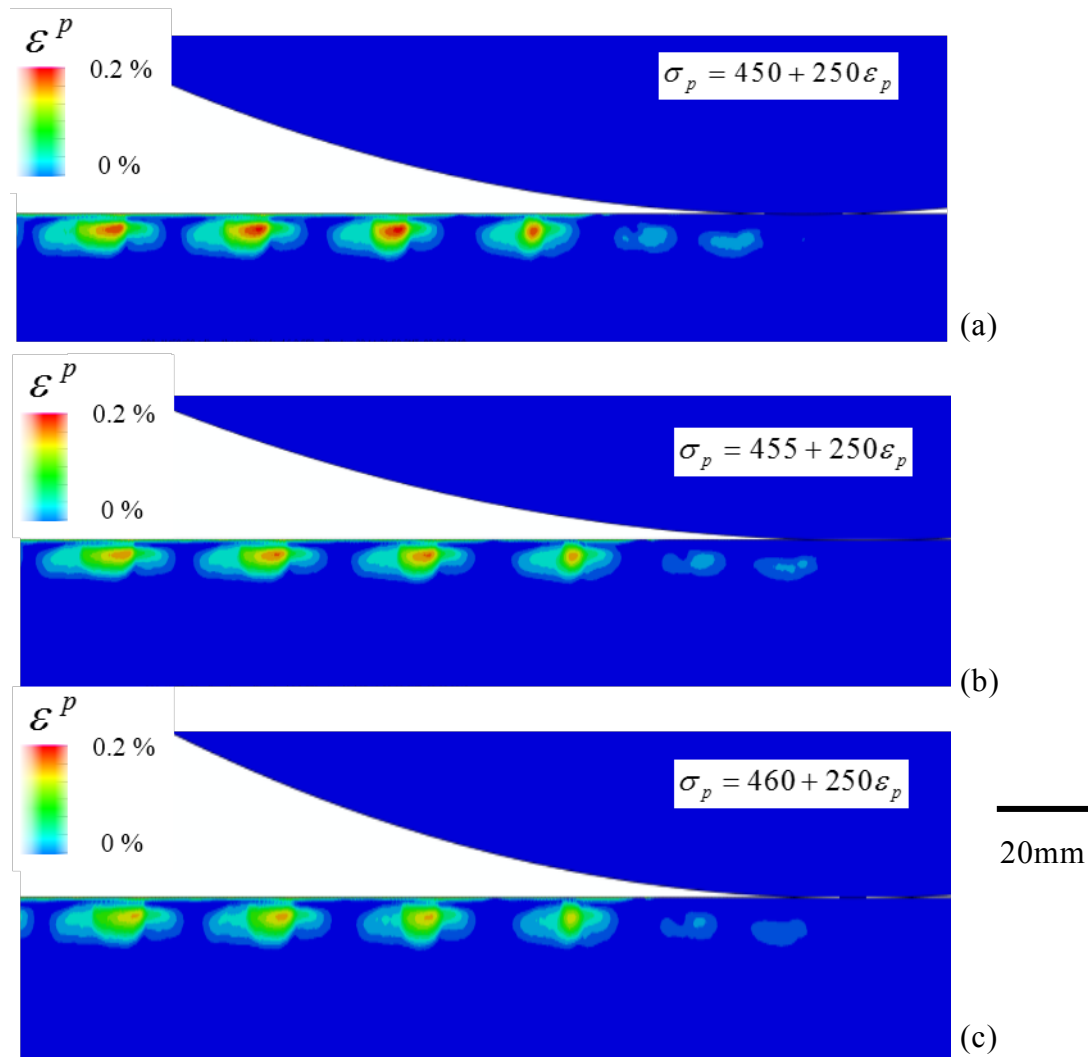


Figure 3.19 Influence of different elastic limits on the evolution of plastic deformation in the rail under slip-stick instability state (Phase B)

3.3.2 Influence of different values of strength index

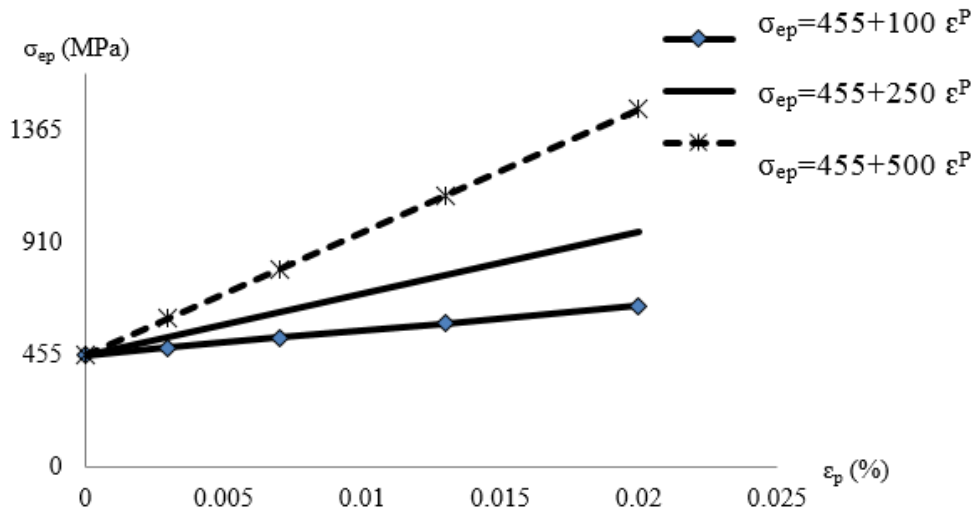


Figure 3.20 Strain-stress curves with different strength indexes

In this second study, the influence of different strength index values will be studied (see Fig. 3.20). The wheel-rail model still uses the same protocol: load $F_{\text{normal}}=8\text{kN}$, slip ratio $\Gamma=20\%$ applied in transient conditions with $\Delta t = 0.1\text{ms}$ which are the same parameters used in Tables 2.1 and 2.2.

The evolutions of global tangential contact force F_{tang}^G (see Fig. 3.21(a)) and global frictional power P_f^G (see Fig. 3.21(b)) show that the strength indexes of the material does not affect the amplitude nor the frequency. The slip oscillatory state remains with the same frequency f_A and the slip-stick oscillatory state remains with the same frequency f_B . The difference of global contact dynamic results between the three different strength indexes is inferior to 5%.

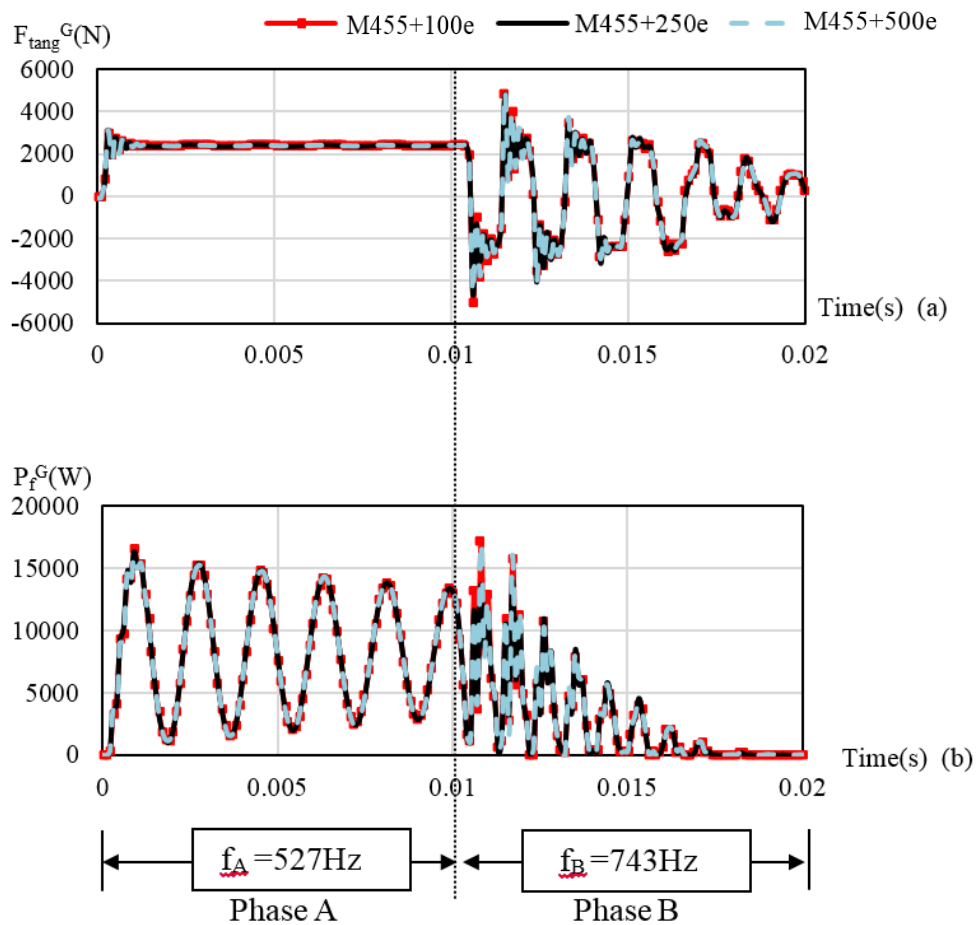


Figure 3.21 Influence of different strength indexes on the evolution of (a) global tangential contact force F_{tang}^G and (b) global frictional power P_f^G

Figures 3.22 and 3.23 show that the wavelength of plastic deformation is not affected by the deformed ratio both in the slip instability state and in the slip-stick instability state. With a higher strength index of the material, it turns to lower plastic deformation.

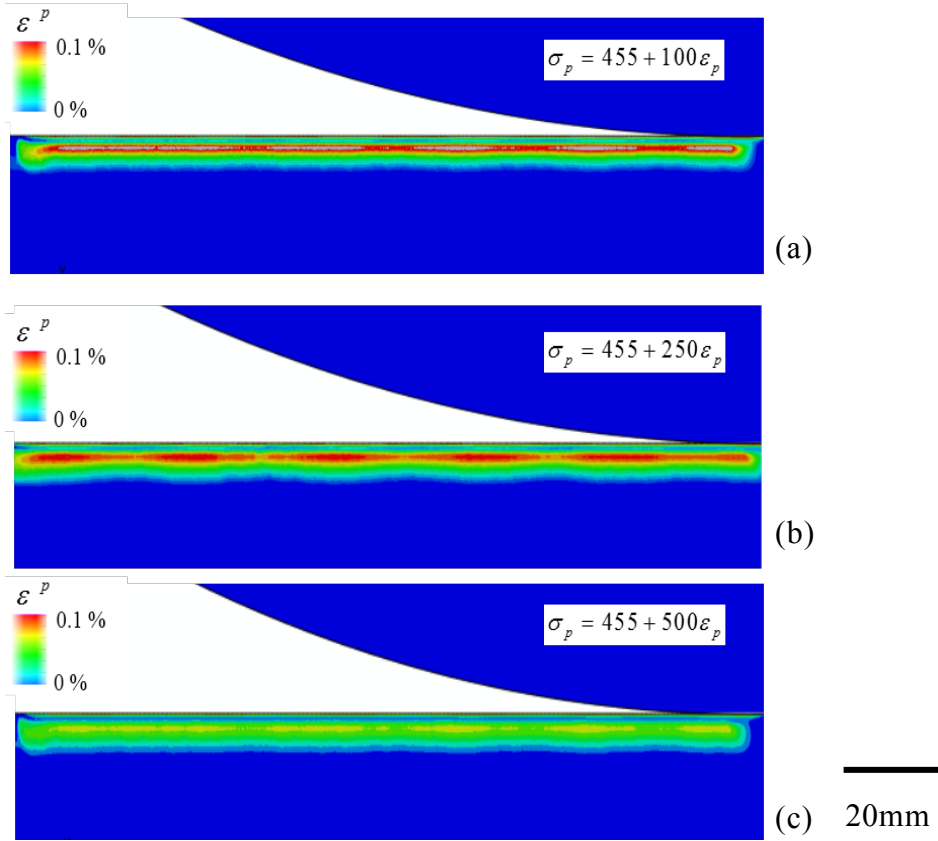


Figure 3.22 Influence of different strength indexes on the evolution of plastic deformation in the rail under slip-stick instability state (Phase A)

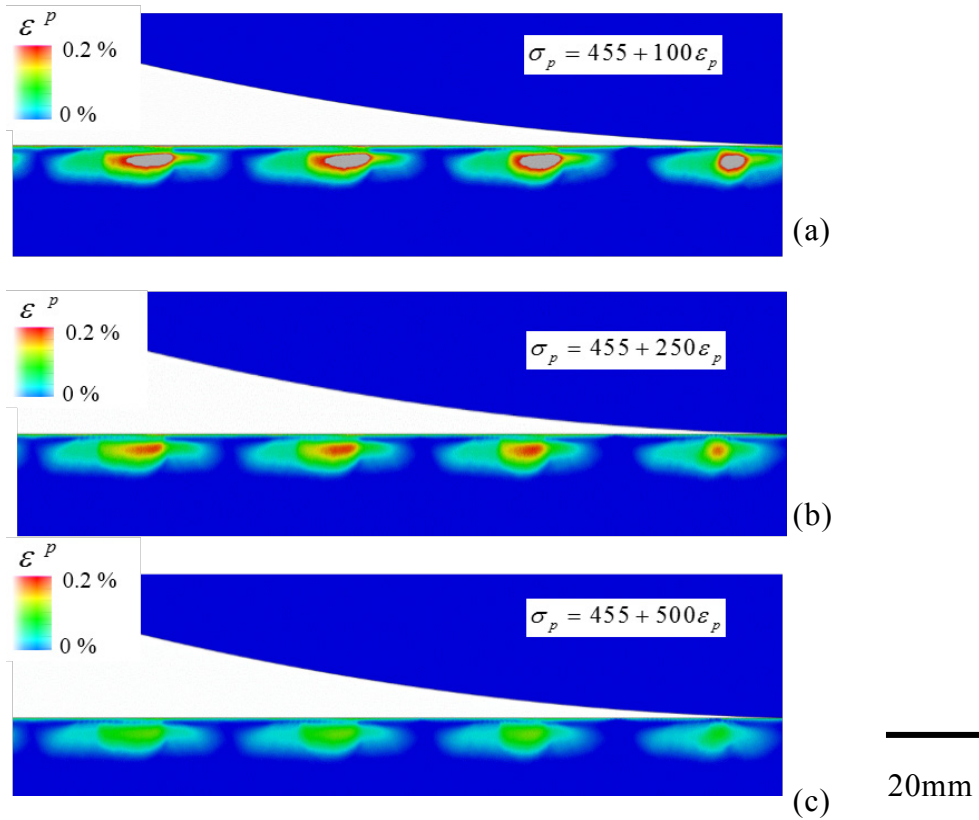


Figure 3.23 Influence of different strength indexes on the evolution of plastic deformation in the rail under slip-stick instability state (Phase B)

The evolution of corrugation defects is very sensitive to the material property. Both the elastic limit and the strength index have a strong influence on plastic deformations. The material property is actually a prevailing factor for the evolution of corrugation defects.

3.4 Consequence of corrugation under different mechanical factors

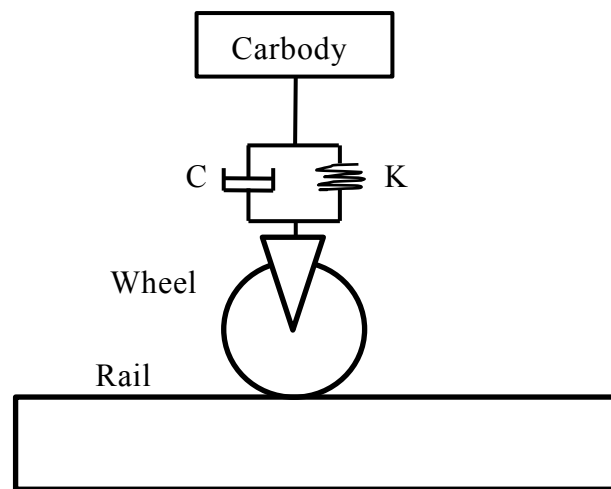


Figure 3.24 Simplified model of railway vehicle and track

In order to further investigate the corrugation defect under transient conditions, the previous model has been modified to take account for a simple modelling of the vehicle by introducing both an equivalent stiffness of equivalent springs and an equivalent damping between the car body and the wheel (see Fig. 3.24). In the simulation, we ignore the influence of the lateral motion of the vehicle and track on wheel-rail contact to pay more attention on the influence of the vertical motion on the corrugation defect. The coefficient of stiffness of equivalent springs and the one of equivalent dampers are not considered in rail ballast and sleepers. So the parameters of stiffness of equivalent springs K and equivalent dampers C in the vertical direction are chosen as $K = 1.15 \times 10^6$ N/m and $C = 2500$ Ns/m [4][43][63]. The protocol and parameters are the same as the ones used in previous model (see Table 2.1 and Table 2.2).

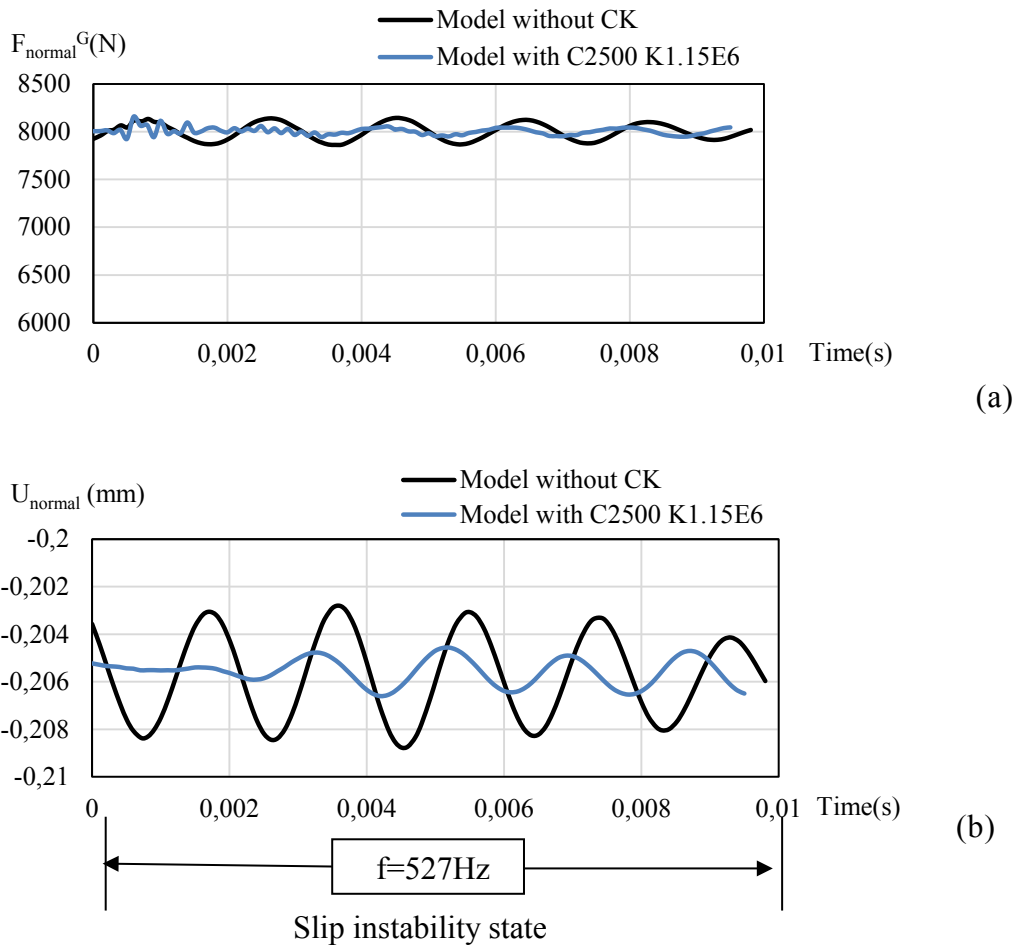


Figure 3.25 Evolution of (a) Global normal contact force F_{normal}^G and (b) Relative vertical displacement of the wheel U_{normal} under slip instability state

The slip instability state is the condition that is closer to reality [1][22]. So the following simulation is done under slip instability state. The results are obtained thanks to a wheel-rail contact model with stiffness and damper taken into account. The global normal contact force F_{normal}^G (see Fig. 3.25 (a)) shows that the frequency of the instability state remains the same. The amplitude of vibration slightly decreased (2%) in the wheel-rail contact that takes into account both the stiffness and the damper of the vehicle. The value of the relative displacement of the wheel U_{normal} in the vertical direction (see Fig. 3.25 (b)) indicates that the wheel is running in a less oscillating process (the amplitude of vibration decreases by 20%) when the stiffness and the damper are considered. The stiffness and damper have an influence on the contact behaviour in

vertical direction. The influence of the normal contact force is supposed to affect the corrugation evolution, which will be studied later.

Nevertheless, the oscillation of the instability state cannot be neglected. The global tangential friction force F_{tang}^G (see Fig. 3.26(a)) in both models, with and without taking into account spring and damper, shows that there is no big difference (inferior to 2%) between the two of them. Global frictional power P_f^G computed (see Fig. 3.26(b)) shows that the model which takes into account the spring and the damper is less dissipative than expected. Because the sliding velocity in the wheel-rail contact varies in an more stable amplitude, it leads to the energy of the model which is less dissipative.

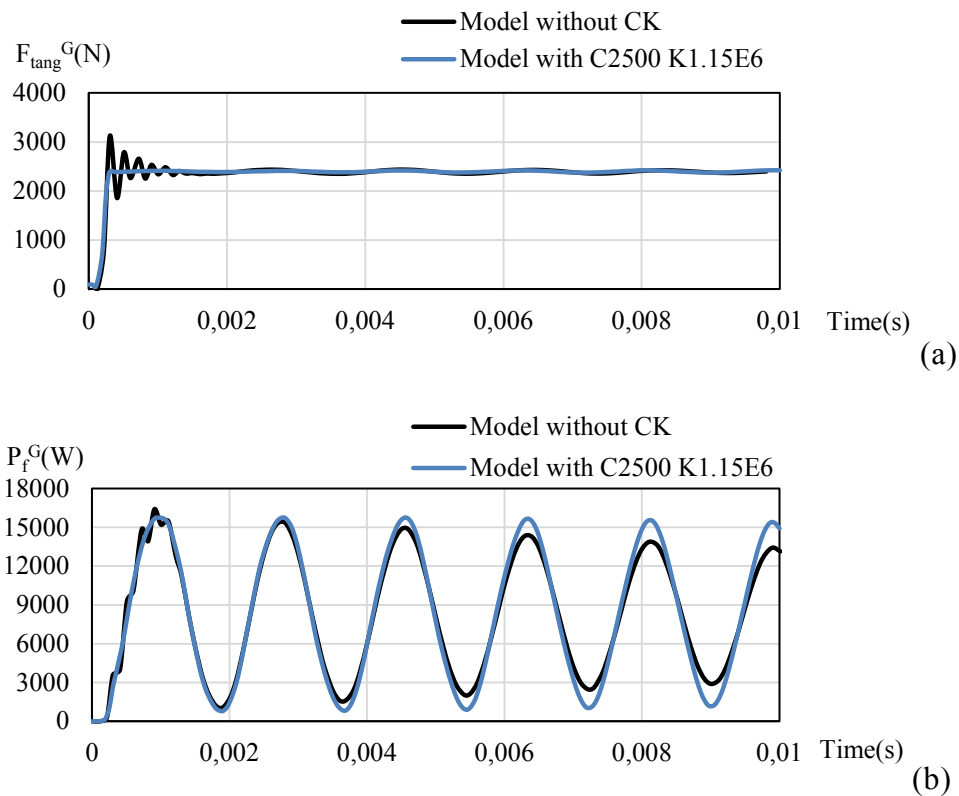
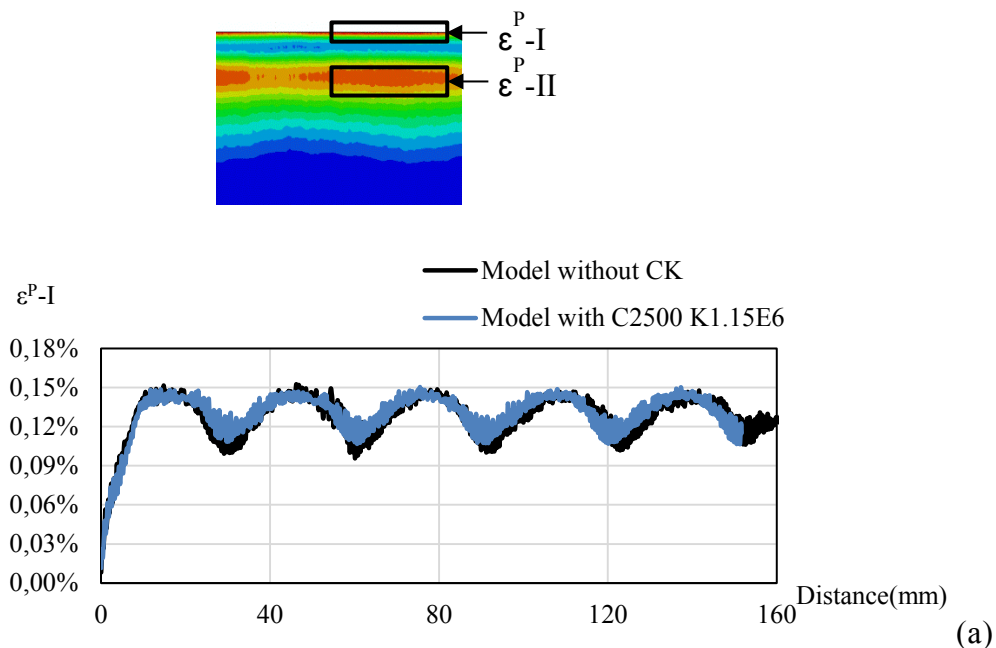


Figure 3.26 Evolution of (a) global tangential contact force F_{tang}^G and (b) global frictional power P_f^G

The result in Figure 3.5 shows that plastic deformation in the rail has two significant layers which are identified both in the surface of and inside the rail.

Figure 3.27 shows plastic deformation measured both in the rail surface ε^P -I and the maximum deformed layer inside the rail ε^P -II (see Fig.3.27 (a)). The amplitude of plastic deformation ε^P -I on the rail surface (see Fig. 3.27 (a)) has no major influence on both models (with and without taking into account the spring and the damper). The value of plastic deformation varies in the range of 0.10% to 0.15%. In the model that takes into account the stiffness of spring and the damper, a very slight influence is obtained on the rail surface plastic deformation. Meanwhile, the amplitude of ε^P -II (see Fig. 3.18 (b)) in the interior of the rail becomes less oscillating.

As a consequence, the relative amplitude between crest and trough in corrugation defect also decreases. This indicates that the periodical plastic deformation inside the rail is becoming less obvious with the influence of the stiffness of spring and the damper. The results show that corrugation defect is mainly affected by the tangential contact force, and that the stiffness of spring and the damper will decrease the oscillation of plastic flow inside the rail.



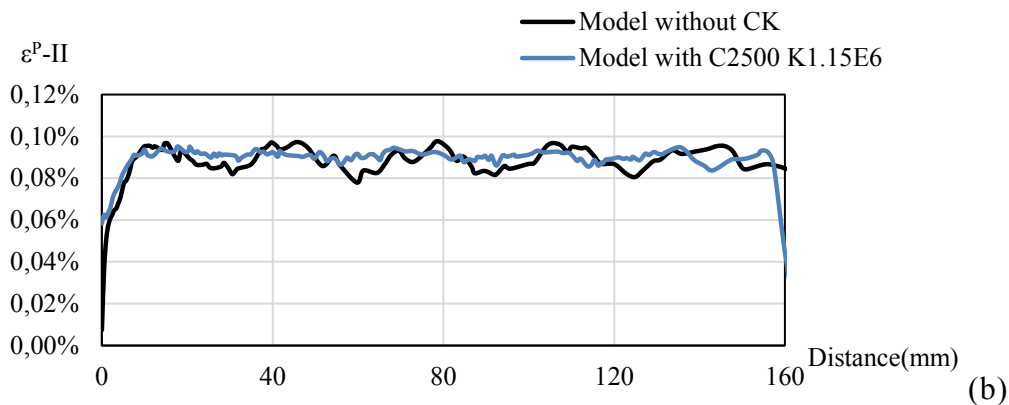


Figure 3.27 Evolution of equivalent plastic deformation ε^P in (a) rail surface and (b) inside rail under slip instability state (Phase A)

3.5 Conclusion

At the beginning of this work, the potential origin of corrugation birth was studied and the sensibility of corrugation defect to a series of parameters was investigated. Results obtained in the finite element model highlight the origin of instability states occurring, and linked to wheel-rail contact under transient conditions. The study of different parameters' influence on the birth of corrugation defect was presented. The wavelength and the frequencies of the two instability states only depended on the mechanical behaviour of the contact. According to this study, parameters, such as slip ratio, friction coefficient, transient conditions applying time, etc..., do have an influence on both slip state and slip-stick state. The different consequences are summarized in Table 3.1. Plastic deformation, which is linked to the corrugation defect, is mainly influenced by material property. Moreover, corrugation defect is not sensitive to the function of the stiffness of spring and the damper between the car body and the wheel. Thus, the parameters under transient conditions have a strong influence on the sensibilities of corrugation defect.

Instability States		ε^P		f (HZ)		F_{tang}^G		P_f^G	
		A	B	A	B	A	B	A	B
Physical parameters	Γ	+	+	527 -	743 -	+	++	++	+
	μ	+	+			++	++	++	++
	Δt	+	+			+	++	++	++
Material law	Elastic limit	++	++			-	-	-	-
	Strength index	++	++			-	-	-	-
Mechanic factor	C	+							
	K					-	++		

++ Important influence + Little influence - No influence

Table 3.1 Summary of the influence of the different parameters

Chapter 4. Parametric sensibility of corrugation evolution under transient conditions with multiple wheel passings and geometric defect influence (welded rail)

In the last chapter, results show a specific contact dynamics consequence on the birth of periodical plastic deformation on the rail surface, as well as periodical increase of local sliding. Nevertheless, such 2D-modelling was performed only with a single passing of a wheel, even if several wheels are required to fully develop straight-track corrugation. As a consequence, the previous dynamic finite element model of wheel-rail contact in 2D will be adapted to allow multiple wheel passings.

4.1 Evolution of corrugation defect under multiple wheel passings

The results of the previous study show the birth of periodical defect at the wheel-rail interface under transient conditions. According to researches [19], corrugation defect develops with several wheel passings. To study the evolution of corrugation defect with multiple wheel passings, the strategy applied in the simulation is defined as followed:

- The instability states are expected in each wheel passing.
- The same transient conditions are applied for each wheel passing in order to compare the evolutions of corrugation defect on the rail.
- The same simulation protocol (see Fig. 2.5) as described in Section 2.2 is used for each wheel passing.

The following analysis was done in two different conditions (see Table 4.1): in TEST1, no slip condition is imposed in the two passings following the first

wheel passing; in TEST2, the slip condition is taken into account in two additional passings. The simulation parameters are summarized in Table 2.1 and Table 2.2.

TEST \ Pass	#1	#2	#3
		Transient conditions	
#1	slip	no slip	no slip
#2	slip	slip	slip

Table 4.1 Transient conditions imposed in analysis

4.1.1 Multiple wheel passings without slip

In TEST1, after the first passing of a wheel with slip, the 2nd and 3rd wheel passings are in pure rolling conditions. In the results of TEST1, the 1st wheel runs in transient conditions, the global tangential contact force F_{tang}^G increases to reach the maximum value of Coulomb friction limit 2400N in slip state and oscillates severely in slip-stick state. When no slip ratio is imposed after the 2nd passing, the global tangential contact force F_{tang}^G (see Fig. 4.1(a)) does not oscillate as the first wheel passes. The value of F_{tang}^G is less than 100N, which is less than the Coulomb friction limit of 2400N. The figure shows the same tendency in the 3rd passing.

The global frictional power P_f^G of 2nd and 3rd passing has a value around zero (300-400W) comparing with P_f^G in the first passing with slip (see Fig. 4.1(b)). Since there is no slip ratio between the wheel-rail contact in the 2nd and 3rd passings, we suppose that the changed geometry of rail surface played a part in the contact dynamics which lead to the value $P_f^G \neq \text{zero}$.

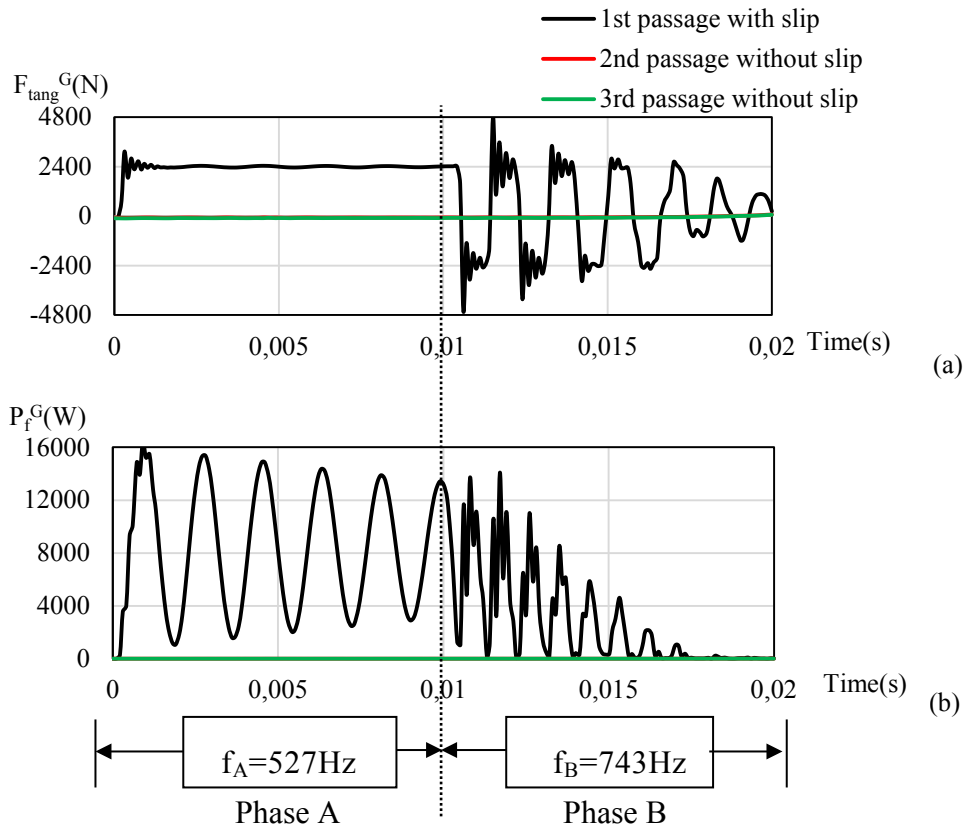


Figure 4.1 Evolution of (a) global tangential contact force F_{tang}^G and (b) global frictional power P_f^G in TEST1

Referring to the figure of the 1st wheel passing under transient conditions (see Fig. 4.2(a)), on the rail surface, the plastic deformation varies between the 0.10% and 0.15% in the slip instability state, and the maximum plastic deformation is produced when the sliding velocity reaches the maximum value. In the stick-slip instability state, the plastic deformation varies severely and the value has a tendency of decrease to zero as function of the global frictional power decreases. The value of plastic deformation shifts from 0.08% to 0.10% in the slip oscillatory state, and has a large variation with the peak deformation of 0.17% in stick-slip instability state. The plastic deformations measured in the 2nd and the 3rd passages with no slip show that there is little change (inferior to 2%) in the plastic deformation. This slight change of ε^P shows that the small periodical

geometry (less than 5 micrometre height) created after the first wheel passing has little consequence (inferior to 2%) on the contact dynamics for the 2nd and the 3rd passings with no slip. The transient conditions are the reason why the oscillatory defect appears.

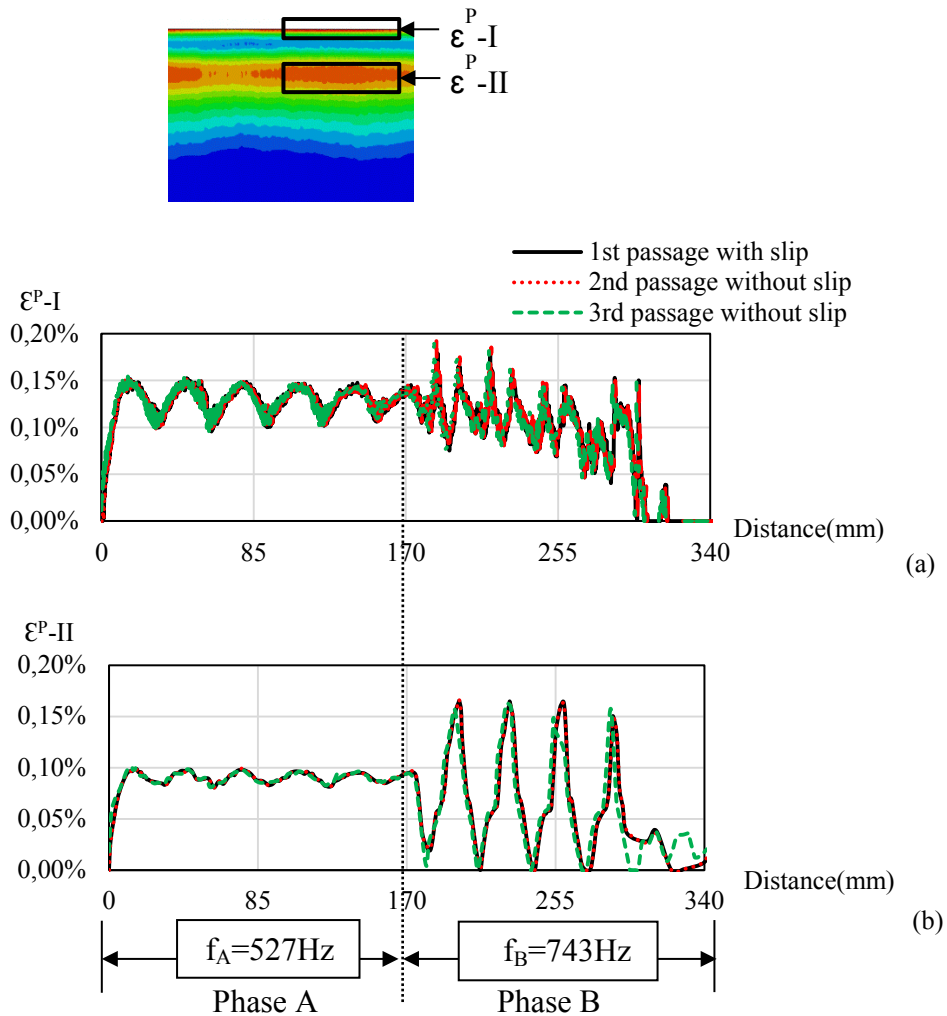


Figure 4.2 Plastic deformation of rail (a) on the rail surface and (b) inside the rail in TEST1

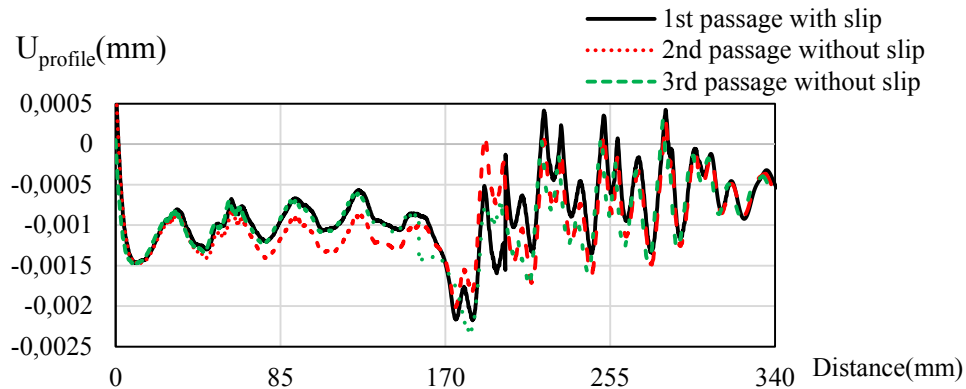


Figure 4.3 Profile of the deformed rail surface after each passing of wheel without slip

The profile of the deformed rail surface (see Fig.4.3) is calculated after the wheel passing. From the curve in Figure 8, the geometry of both crest and trough on the rail surface coincide with the evolution of the plastic deformation in the contact surface. But even though the second passing without slip has no influence on the rail plastification, the rail surface is still deformed. The amplitude of profile decreases of about $0.2 \mu\text{m}$. On the contrary, the deformed rail surface is recovered after the third passing. The amplitude of the surface profile increases by $5 \mu\text{m}$. This figure indicates that the stable rolling contact conditions has no major effect on the rail geometry. And without transient conditions applied, the corrugation defect will not be developed within only three wheel passings.

4.1.2 Multiple wheel passings with slip

As an analogy with TEST1 (the wheel passings without slip), to verify the influence of transient conditions on the evolution of corrugation defects, TEST2 carries out a 2nd and 3rd wheel passings with a slip ratio imposed for each passing. The simulations are stepped from the previous passing in order to import the wheel and rail status to the following wheel passing. Simulation parameters remain the same (Fig 2.5, Table 2.1 and Table 2.2) where the slip ratio Γ is

kept at 20%, imposed in $\Delta t = 0.1\text{ms}$, normal force F_{normal} in the three wheels passings.

The amplitude of the global tangential contact force F_{tang}^G (see Fig. 4.4 (a)) doesn't change during the slip instability state after the first millisecond of simulation in Phase A. But in Phase B, for the following wheel passings (2nd passing and 3rd passing), the amplitude of F_{tang}^G does not oscillate much, as it does in the previous passing. Both slip state and slip-stick state in each passing remain with the same frequency described previously (See section 3.1).

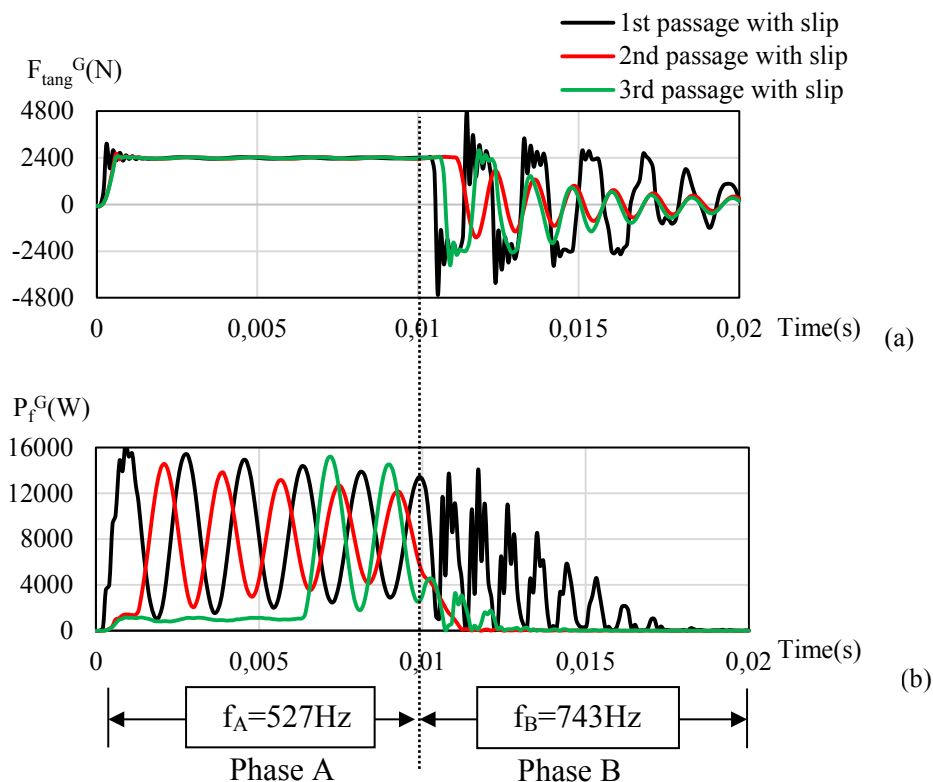


Figure 4.4 Evolution of (a) global tangential contact force F_{tang}^G and (b) global frictional power P_f^G in TEST2

The amplitude of P_f^G (see Fig. 4.4 (b)) seems to slightly decrease after both 2nd and 3rd wheel passings; this evolution might be due to the accommodation of the slip velocity at the interface which is slightly modified due to the periodical geometry created after the 1st wheel passing. In Phase B, the amplitude of

P_f^G does not oscillate as high as during the 1st wheel passing, which means that sliding velocity in the contact nodes shifts quickly to zero as the slip ratio is removed.

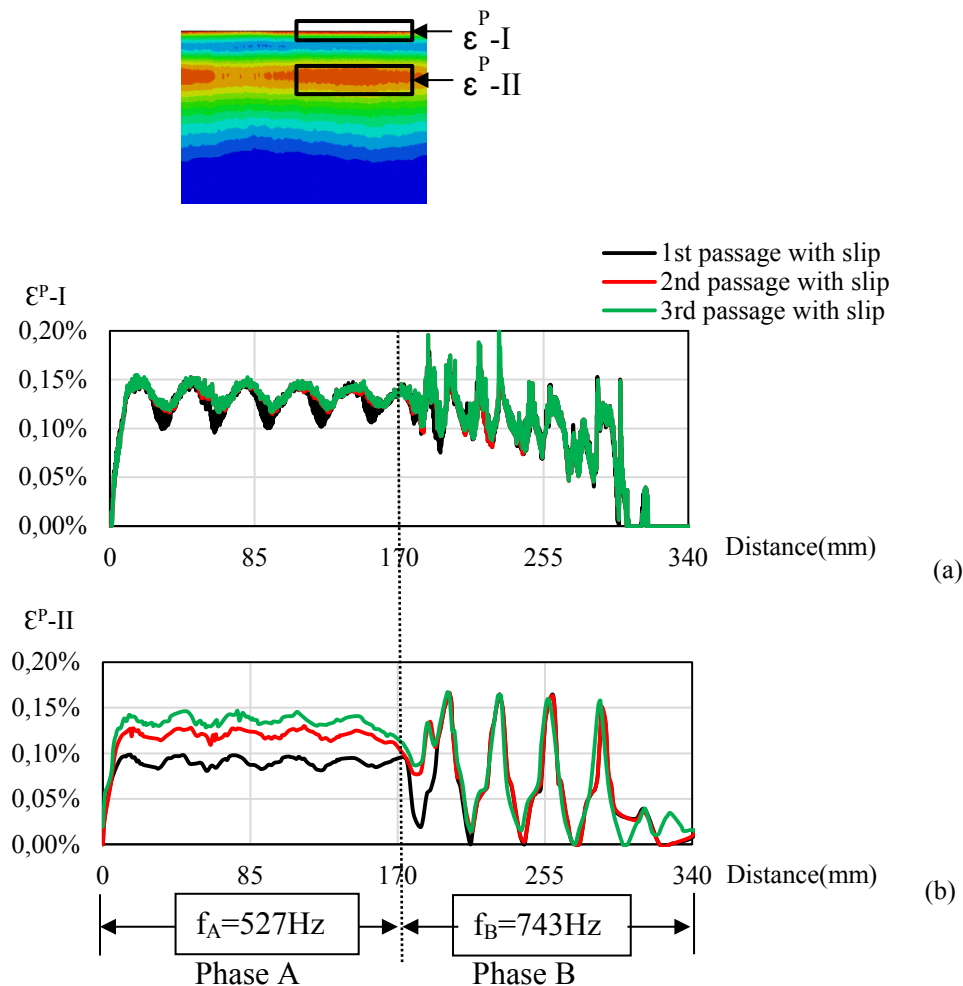


Figure 4.5 Equivalent plastic deformation (a) on rail surface and (b) inside the rail in TEST2

The amplitude of the plastic deformation ϵ^P -I on the rail surface (see Fig. 4.5 (a)) does not change much (inferior to 5%) through the multiple wheel passings. The value of the plastic deformation varies in the same range from 0.10% to 0.15%, and the peak value of plastic deformation is about 0.01% different from one passing to another. The multiple wheel passings with slip have very

slight influence on the rail surface plastic deformation. The transient conditions are supposed to be the main reason that leads to the development of corrugation defect.

On the contrary, the amplitude of ε^P -II (see Fig. 4.5 (b)) inside the rail increases with the number of wheel passings while slip instability state occurs. As a consequence, the relative amplitude between crest and trough of corrugation defect, see Figure 4.5(b), also increases with the number of wheel passings. Indeed, this value rises from 0.018% for the first wheel to 0.021% for the second wheel and finally reaches 0.028% for the third wheel. This indicates that the periodical plastic deformation inside the rail is becoming more and more evident with the repetition of such transient conditions. And there is no change in Phase B (stick-slip oscillatory state) in which the oscillatory consequence is very weak. The results of ε^P -II show that the plastic flow inside the rail has an important role on the corrugation defect development.

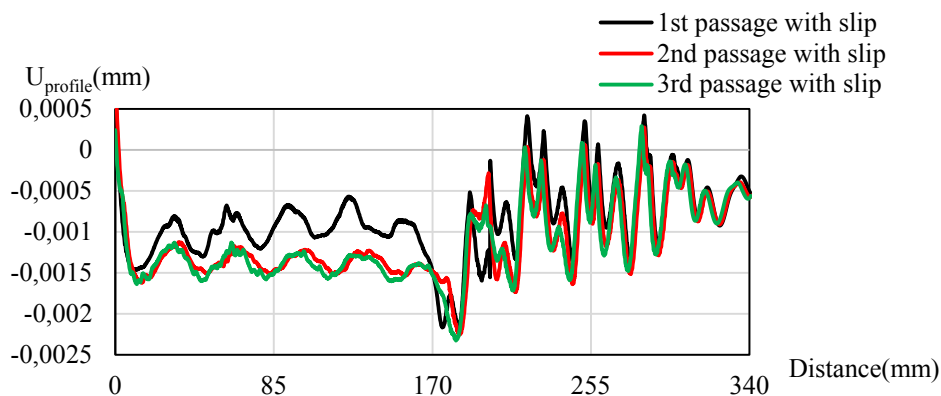


Figure 4.6 Profile of the deformed rail surface after each wheel passing with slip

The geometry of the rail surface measured after the wheel passing with slip (see Fig. 4.6) shows that the profile is decreased to 0.5 μm from the first passing to the second passing, and shows little change after the third passing.

4.1.3 Discussion of the results

According to the analysis with the different transient conditions in each wheel passing, a summary table (see Table 4.2) shows the influence of transient conditions on the results. From a qualitative point of view, these results coincide with on-site observation of real corrugation defect on rail surface[4].

Transient condition Numerical results	Pass #1		Pass #2		Pass #3	
	slip	slip	no slip	slip	no slip	slip
Frequency f	0	0	0	0	0	0
F_{tang}^G	++	++	0	++	0	++
P_f^G	++	++	0	++	0	++
ε^P -I	++	++	0	0	0	0
ε^P -II	++	++	0	++	0	++
Corrugation profile	++	++	0	++	0	++
Corrugation growth	++	++	0	+	0	+

++ Important influence + Little influence 0 No influence

Table 4.2 Summary of the influence of different parameters on the multiple wheel passings analysis

In Table 4.2, the corrugation profile refers to the curve of plastic deformation observed on rail surface (see Fig. 4.4(a)), and the corrugation growth refers to the difference between each wheel passing. Through this Table, the influence of the contact dynamics is highlighted under transient conditions. And it is indicated that the transient conditions influenced both plastic deformation and profile geometry of the rail. The corrugation defect is developed under transient conditions, the plastic flow inside the rail plays an important part in the corrugation defect development; indeed, such defect grows with both the number of wheel passings and the repeatability of contact conditions.

4.2 Evolution of corrugation defect under wheel passing on the jointed rail area



Figure 4.7 Welded rail joint[69]

Railway rails are manufactured in sections of 25–120 m length. The method of joining rails has changed over the years. In the past, the most common method was to use bolting; however, it was found that bolted joints were also a cause of rail defects. As a consequence, new joining methods for rails were investigated, and in the 1950's, the first welded rails began to appear in tracks. The

use of the welding method for joining rails has since then been applied increasingly, and it is now standard practice all over the world. The most important reasons to use continuous welded rails, in contrast to bolted rails, are the lower maintenance cost and the improved dynamic behaviour of the train-track-rail system.[12]

The joints between the metal rails have always been recognized as a potential source of weakness in the construction of railways[70]. So if the use of continuous welded rail (CWR) has showed its advantages, it has also showed its weak spots[63]. Small cracks or other defects can appear in the welded cross-section[12]. And on the welded rail area, the stresses introduced in a rail by a passing train are very significant, and the influence of flexural action and local contact stresses from axle load and train speed are highlighted [63].

In previous works, the wheel-rail dynamic contact model dealt with the corrugation defect evolution on the rail surface without taking into account the geometric irregularity. Therefore, the following work will deal with the influence of the geometric irregularity of the welded rail joint, which on-site measurement is provided by RATP (see Fig. 4.8), on the corrugation defect observed in this welded rail area.

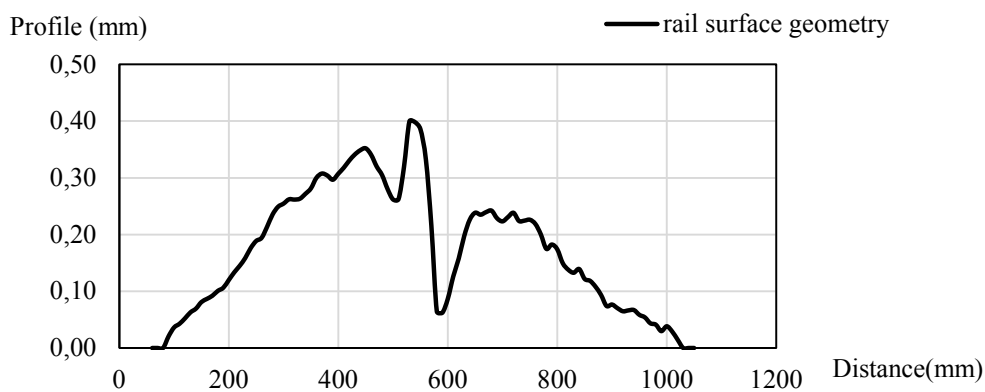


Figure 4.8 Profile geometry of welded rail joint area

4.2.1 Birth of corrugation defect under influence of the welded rail joint irregularity

To investigate the influence of the welded rail joint irregularity, the dynamic FEM model considers the wheel passing on the welded rail joint area with a constant velocity without sliding. The force F_{normal} is 8kN, velocity V_{wheel} is 17m/s. The rail length is 2000mm, and the geometry of the rail surface uses the data in Figure 4.8. Though the material property of rail joint area is different from the normal rail, the present model will only deal with the geometric irregularity and considers the material property homogeneous in the rail in order to simplify the dynamic FEM model. The effect of material property in rail joint area will be studied in the future.

4.2.1.1 Model without considering the mechanical factors

In the first numerical simulation, only the interactions between wheel and rail are considered and simulated by contact elements. The results of the maximum contact pressure (see Fig. 4.9) show that the normal load has a large influence on the contact stresses under the condition of rail joints (from 500mm-700mm). The amplitude of contact pressure P_{max} has increased by two times in the joint area compared with the value in normal rail ($P_{\text{max}}=850\text{MPa}$). The amplitude of P_{max} raises up to 1500 MPa where the wheel runs on the peak profile of the rail joint area. After the area of the rail joint, the contact pressure varies much more, which indicates that the contact dynamics between the wheel and rail is highlighted with the rail joint.

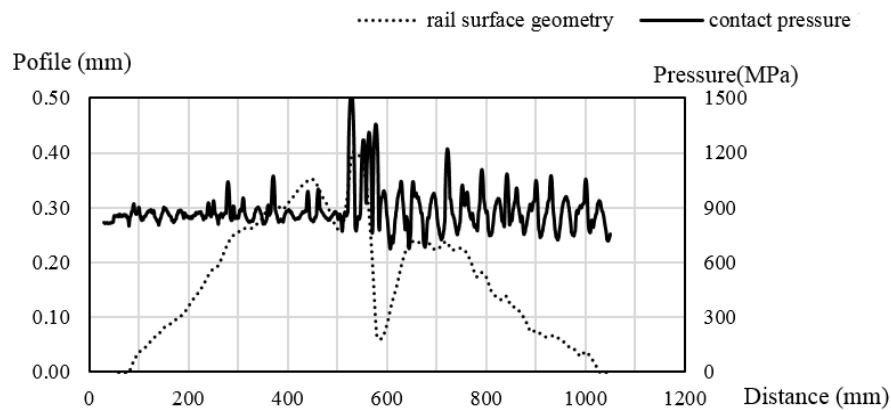


Figure 4.9 Distribution of maximum contact pressure P_{\max} along the rail surface in original model

4.2.1.2 Model with considering the mechanical factors

In the following part, we consider that the influence of stiffness of equivalent springs K and equivalent dampers C in the vertical direction between wheel and rail. The parameters are chosen as $K=1.5160E+06$ N/m and $C=7160$ Ns/m (data provide by RATP), respectively. The maximum contact pressure (see Fig.4.10) increased when the wheel was rolling on the rail joints but after passing the peak profile, the curve showed that the wheel was rolling without contact with the rail surface. So the contact pressure became equal to zero which indicates that the wheel jumped over the rail joints.

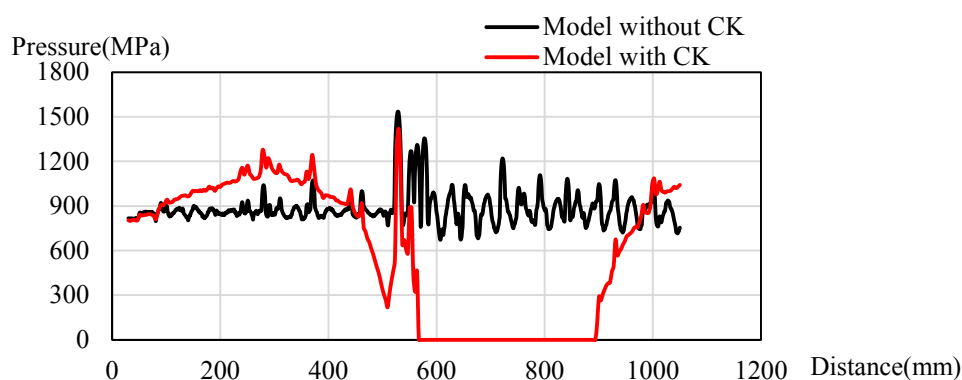


Figure 4.10 Distribution of maximum contact pressure P along the rail surface in the model with and without consideration of mechanical factors

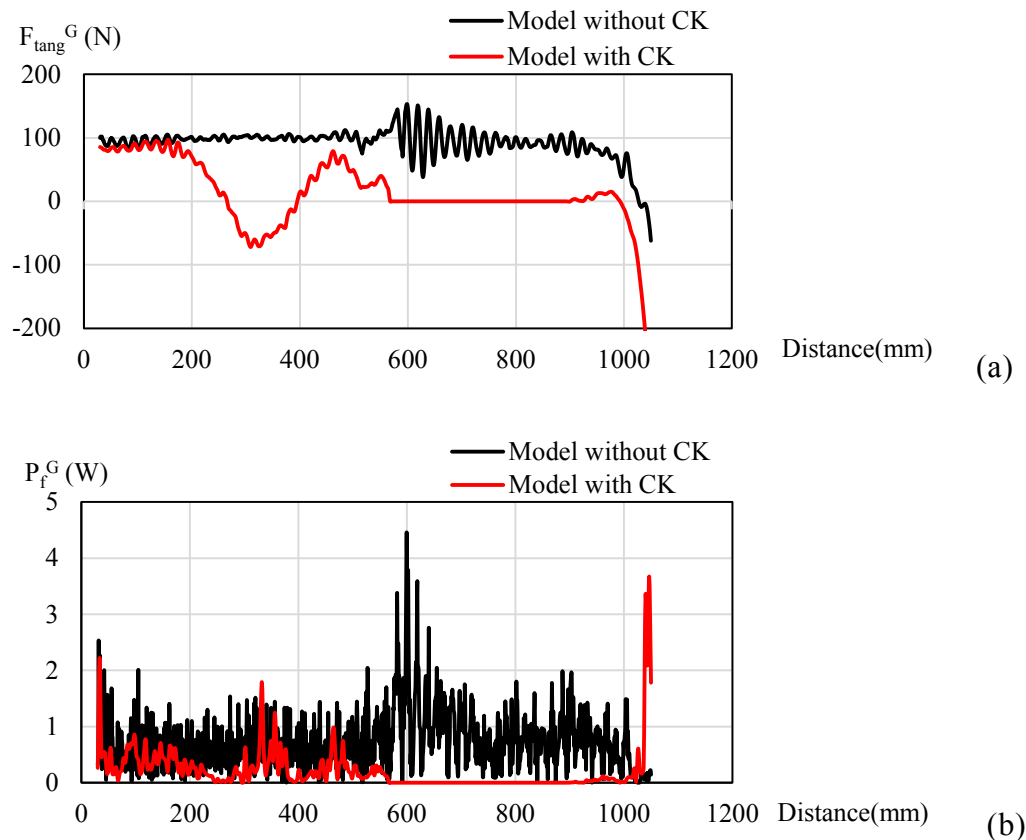


Figure 4.11 Evolution of (a) global tangential contact force F_{tang}^G and (b) global frictional power P_f^G

As there is no sliding ratio defined in this model, both global tangential contact force F_{tang}^G and global frictional power P_f^G (see Fig 4.11) are very small ($\sim 0\text{W}$) comparing to the instability states in previous results (see Chapter 3). But the irregularity of the rail joints slightly influenced the results. Without considering the mechanical factors, the global frictional power seems more various; and the value of P_f^G decreased much more in the model with mechanical factors. It shows that, with considering the mechanical factors, the model becomes more stable and the vibrations of the movement are reduced.

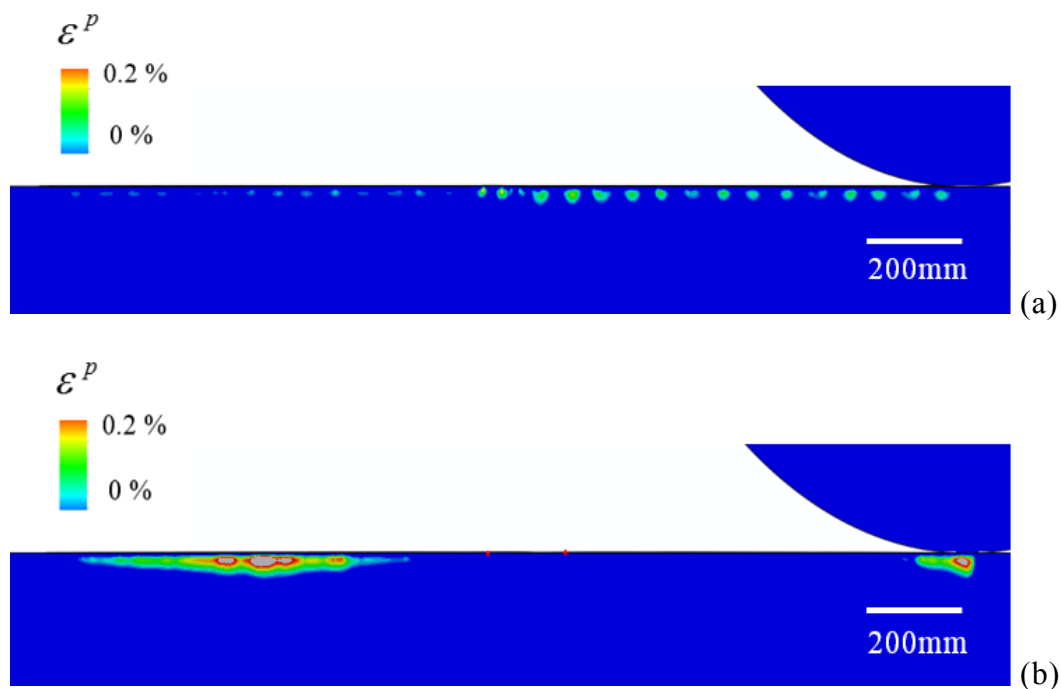


Figure 4.12 Equivalent plastic deformation ε^P in the rail with joints geometry (a) without considering mechanical factors, (b) with considering mechanical factors

The equivalent plastic deformation ε^P in the rail with joints geometry (Fig.4.12 (a)) shows that before the wheel passes the rail joints, there is no significant plastic deformation in the rail. After passing the rail joints geometry, the slight plastic deformation ε^P evolves periodically in the rail with a value about 0.1% and a wavelength about 20mm that is mainly distributed inside rail area. The corrugation defect is not yet produced on rail surface with joints geometry because there is no transient conditions or repetition of wheels passing, but the evolution of plastic deformation inside the rail shows that rail joint geometry contributes to the formation of plastic flow.

Otherwise, considering the mechanical factors in the wheel-rail contact model, the increased contact pressure makes the deformation more obvious with a value about 0.3% before the wheel passed the rail joints (see Fig 4.12(b)). And the plastic deformation becomes null till the wheel rolls in contact the rail. The

results seem to differ from reality. In fact, the wheel will not jumped over the rail when it passes the rail joints area. So the model should consider the axle loads applying accurately.

4.2.2 Evolution of corrugation defect under influence of the axle loads

Under condition of velocity V_{wheel} of 17m/s, stiffness of equivalent springs K and equivalent dampers C in the vertical direction between the wheel and rail contact are chosen as $K=1.5160E+06$ N/m and $C =7160$ Ns/m. According to the data provided by RATP, the maximum contact stress usually reaches more than 1GPa in the rail joints areas, so an axle load of 16kN is chosen. In the following work, the influence of the axle loads of 8kN and 16kN on the maximum contact pressure will be shown in Fig.4.13. It was found that the investigated results increase with the increased axle load. And with the higher axle load, the wheel rolls over the rail joints without losing contact with the rail surface.

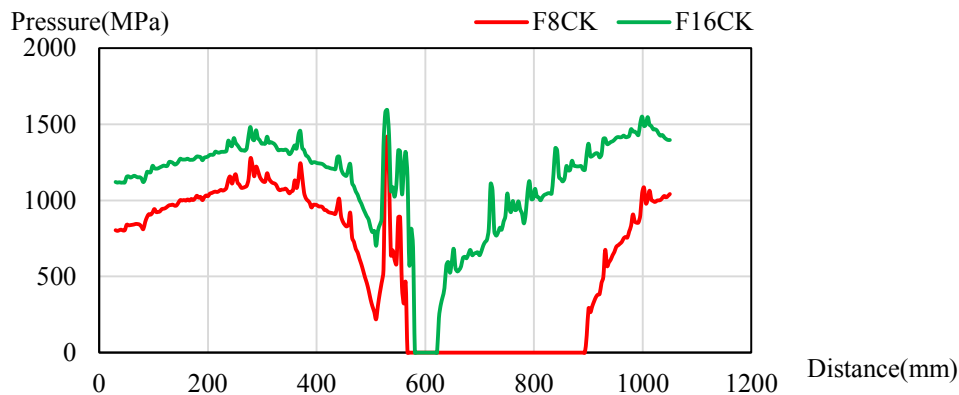


Figure 4.13 Distribution of maximum contact pressure P_{max} along the rail surface in the model with different axle loads

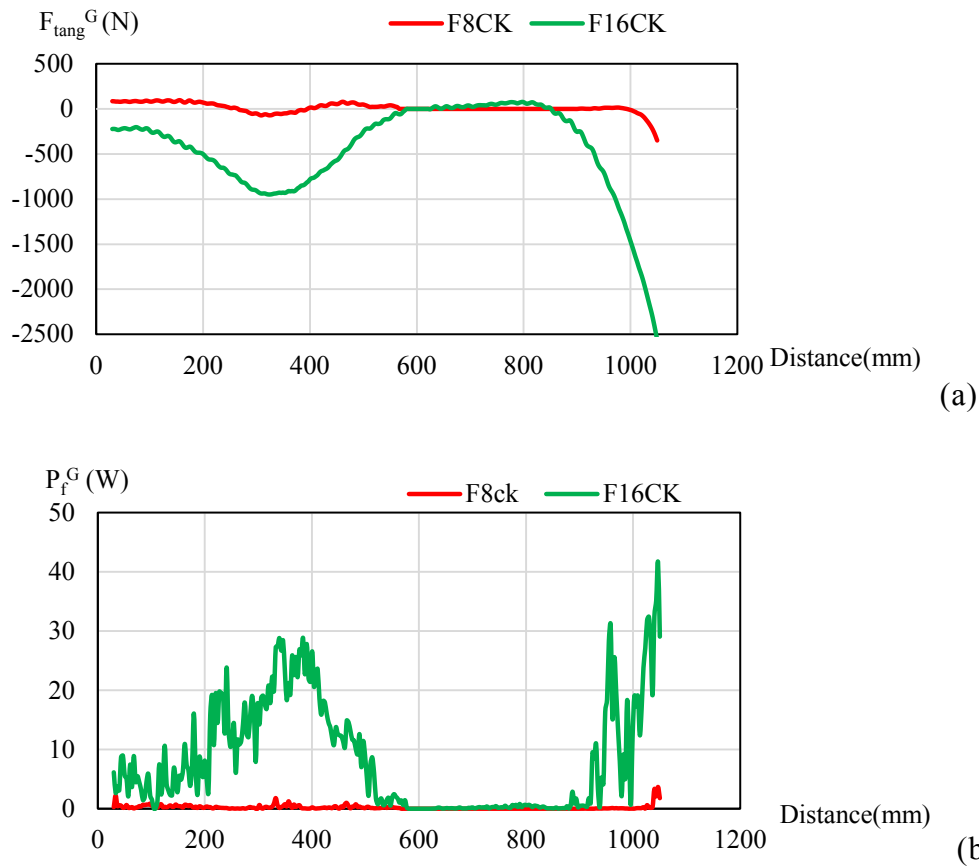


Figure 4.14 Evolution of (a) global tangential contact force F_{tang}^G and (b) global frictional power P_f^G

With different axle loads defined in the model, both global tangential contact force F_{tang}^G and global frictional power P_f^G (see Fig 4.14) increase with higher axle load. But after the wheel passed the rail joints area, the wheel lost in contact with rail, leading the global tangential contact force F_{tang}^G and the global frictional power P_f^G to return to zero. With a higher axle load, it is expected to have more influence on the wheel-rail contact dynamics.

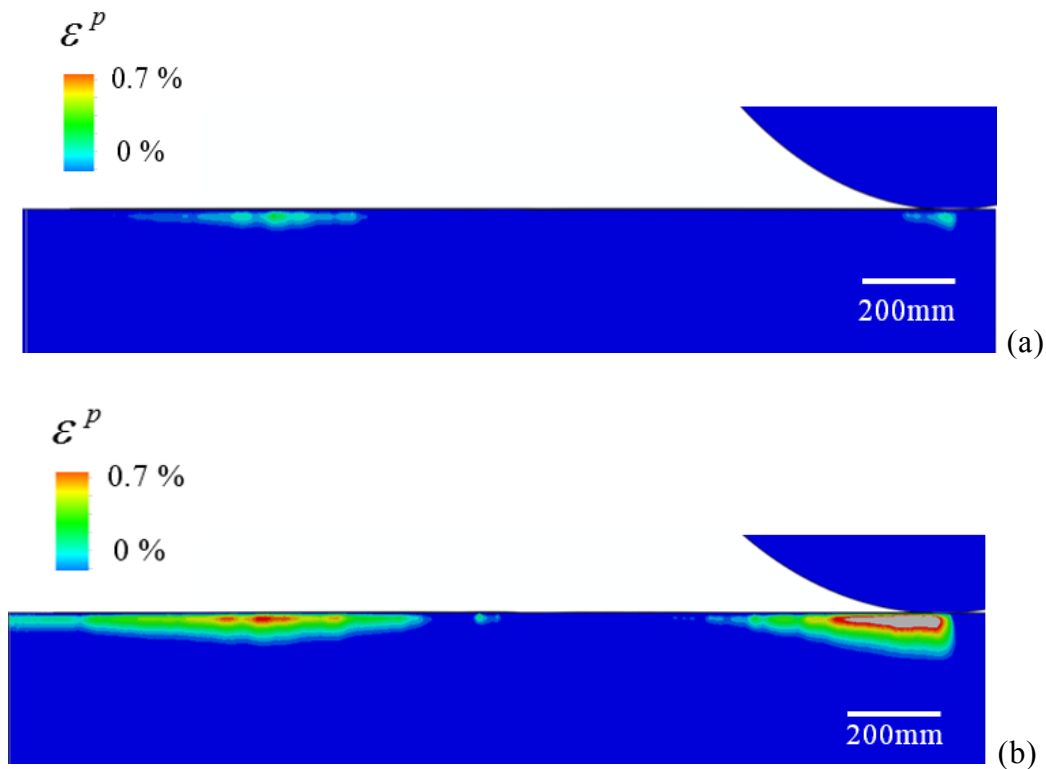


Figure 4.15 Equivalent plastic deformation in the rail joints with different axle loads of (a) 8kN and (b) 16kN

The equivalent plastic deformation is also influenced by a higher axle load (see Fig.4.15). As the axle load increases from 8kN to 16kN, the maximum plastic deformation raises from 0.3% to 1%. The deformed area extends from the interior rail to the rail surface. These results indicate that the axle load has a large effect on the contacting force and stresses. With a higher axle load, the corrugation defect is still not evident on the rail surface, but the plastic flow is getting severe, and extends to the rail surface. These results prove that the transient conditions are the main reason affecting corrugation birth, but the defect is also sensitive to the influence of the geometric irregularity and the axle load.

4.2.3 Evolution of corrugation defect under the rail joints between two sleepers

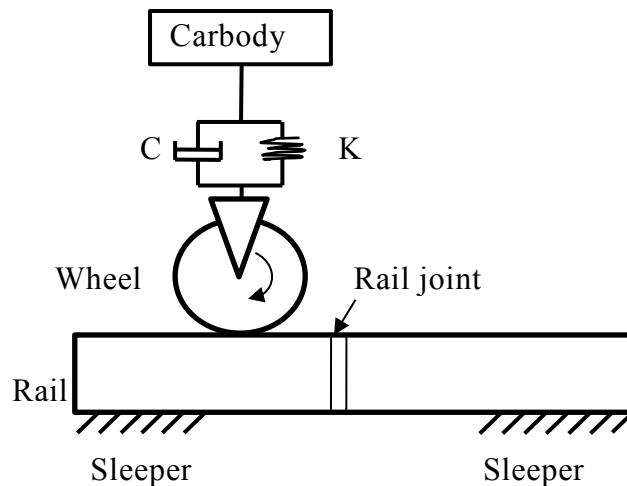


Figure 4.16 Mechanical model of wheel and rail joint

The analyses of the stresses in rail joint area, which take dynamic effects into account, were presented previously. The 2D elastic-plastic finite-element model is put forward to study dynamic stress when a wheel passes over a rail joint. The interactions between wheel and rail, between wheel and rail joint and the effects of train speed, axle load and mechanical factors have been investigated.

In the following part, new simulation attempts to represent the influence of rail joints between the sleepers will be undertaken. The rail is periodically constrained through the sleepers and the rail joint area is left out of restraints. The wheel passes as a constant velocity of 17m/s, and with the axle load 16kN. Meanwhile, the stiffness of equivalent springs K and equivalent dampers C in the vertical direction (see 4.2.1.2) between the wheel and rail contact are also taken in account.

The contact pressure P_{\max} (see Fig. 4.17) doesn't show much difference before the wheel passes over the rail joint between two sleepers; it seems that the sleeper localized before the rail joint doesn't affect the contact stresses. Then the pressure was increased by 500MPa when the wheel passes over the rail

joints area. When the wheel arrives over the latter sleeper, passes the rail area from a restraints-free condition to a fully-restrained condition. The contact area is becoming smaller, and contact force higher, which lead to an increased contact pressure. The tendency is the same in the wheel-rail contact dynamics (see Fig.4.18). Although in the wheel passing process, the whole rail surface is in contact. The global frictional power is still null when the wheel passes on the rail joints area because there is no sliding between the wheel-rail contacts.

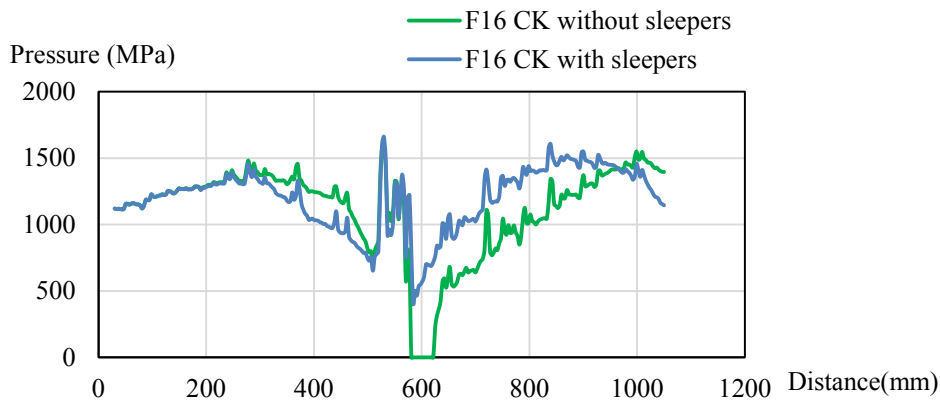
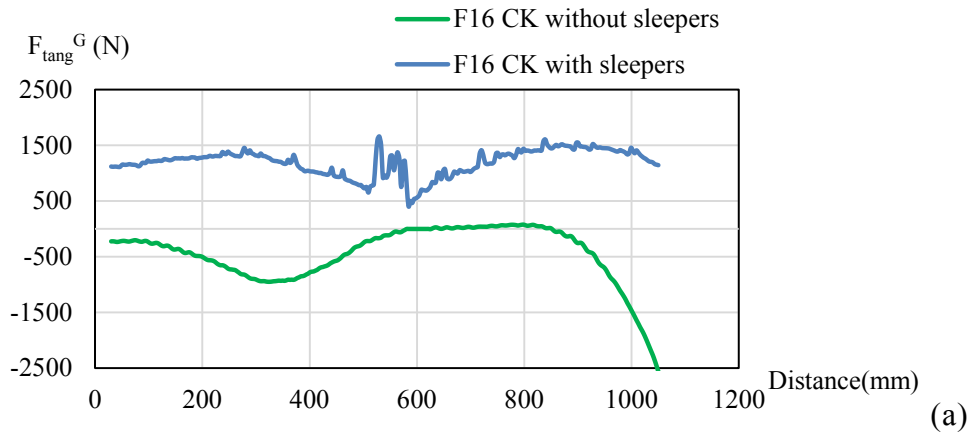


Figure 4.17 Distribution of maximum contact pressure P_{\max} along the rail surface in the model under different rail conditions



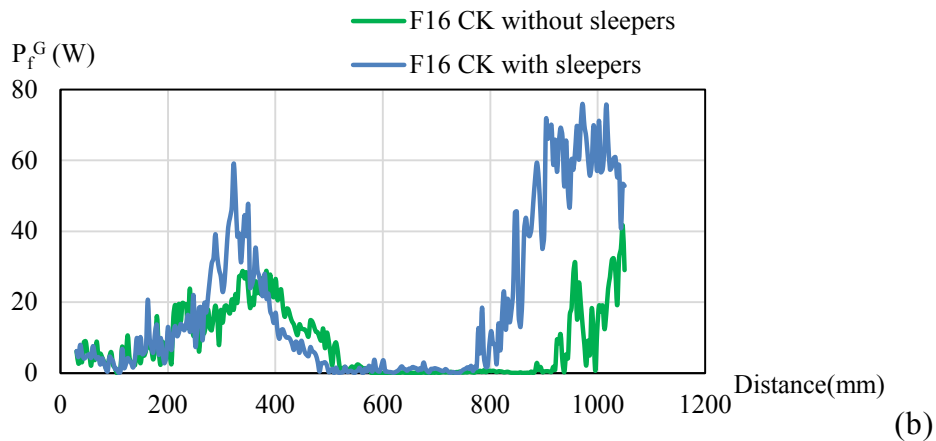


Figure 4.18 Evolution of (a) global tangential contact force F_{tang}^G and (b) global frictional power P_f^G

Thus, the change of contact stress influences the plastic deformation (see Fig.4.19). And over the two sleepers, the plastic deformation is really evident (see Fig.4.19 (b)). Nevertheless, the plastic deformation is very small in the rail joint area between the two sleepers where the contact pressure is not equal to zero. Once the wheel passes after the rail joint area, the plastic deformation increases from null to 1% and keeps in longer distance comparing the results without considering the sleepers.

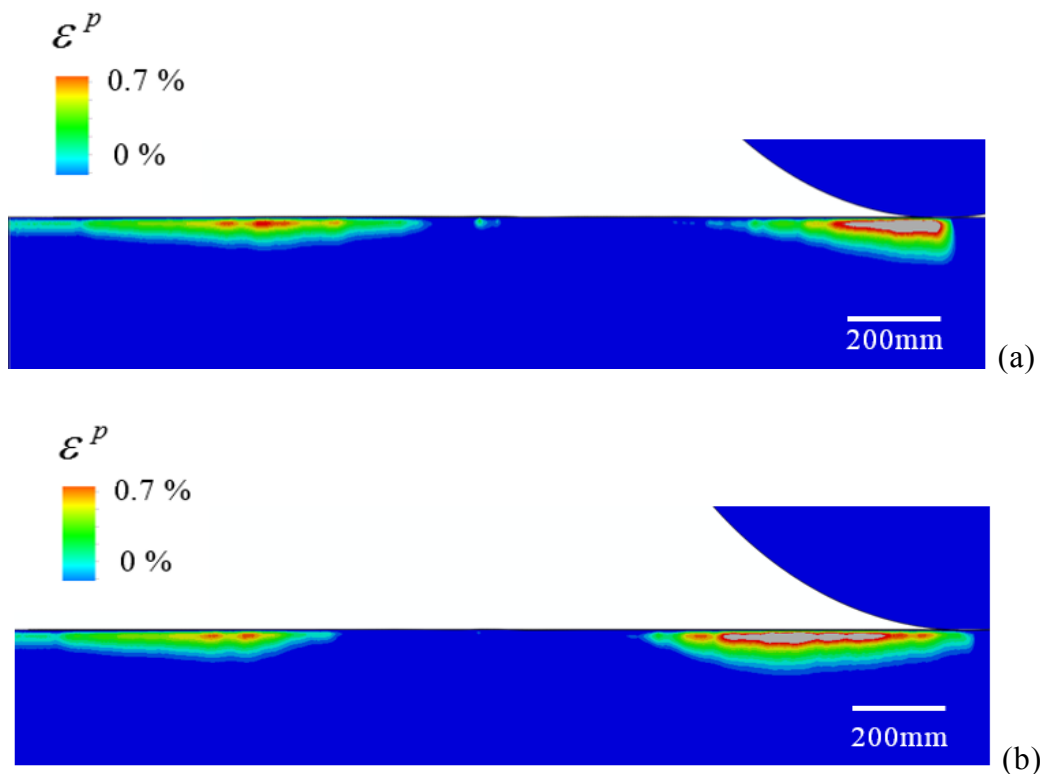


Figure 4.19 Equivalent plastic deformation in the rail (a) without sleepers (b) and with sleepers

4.3 Conclusion

This chapter dealt with the evolution of corrugation defect in multiple wheel passings and the influence of geometric irregularity in rail joints.

At first, the influence of the contact dynamics was highlighted under transient conditions within multiple wheel passings. The corrugation defect is developed under transient conditions, the plastic flow inside the rail plays an important part in the corrugation defect development; indeed, such defect grows with both the number of wheel passings and the repeatability of contact conditions.

Secondly, under the pure rolling state of the wheel-rail contact process, the irregularity of the rail joints has much influenced the deformation of rail subsurface. The 2D elastic-plastic finite-element model is put forward to study dynam-

ic effects when a wheel passes over a rail joint area. The interactions between wheel and rail, between wheel and rail joint and the effects of train speed, axle load and mechanical factors were investigated. And the axle load has a larger effect on the contacting force, stress and deformation than the other conditions.

Actual demands on train traffic are heavier axle loads, higher train speeds and increased traffic density. To prevent accidents due to fracture of weld, and to lower maintenance costs, more detailed numerical analyses of rail joints are of great interest for the railway industry. The limitation of the computational cost to study the long rail model should be optimized and an improvement of the model should be proposed.

Part 3 Improvement of the 2D dynamic FEM model to reproduce the corrugation defects realistically

Chapter 5. Problem of the 2D dynamic FEM model and a suggested solution

5.1 Numerical dissipation problem

The results obtained in the slip phase (see Fig 5.1) show a problem of quick energy dissipation, which doesn't coincide with the straight-track corrugation reality. According to the previous work (Chapter 3), the global frictional power, composed of tangential contact force and sliding velocity, plays an important part in the birth of corrugation defects under transient conditions. And the energy dissipation means the appearances of corrugation defects are progressively dissipative. According to Akira et al. [71], the corrugation defect would be quite constant in long term, and would lead to a change of geometry profile with hundreds or thousands of wheels passings (see Fig.5.2). Therefore, a method should be found to solve the unusual energy dissipation problem in the wheel-rail dynamic contact problems.

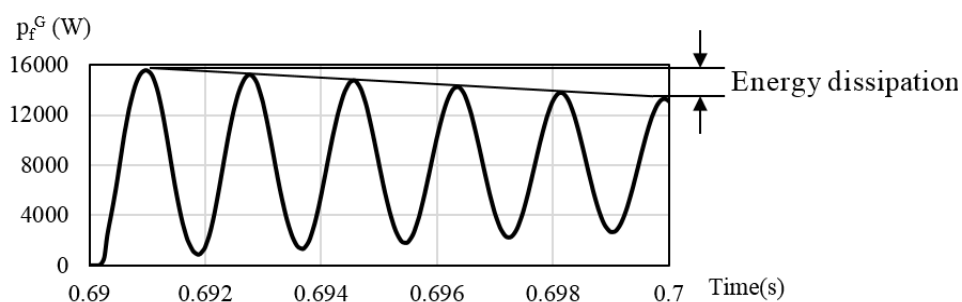


Figure 5.1 Evolution of global frictional power P_f^G in slip state (Chapter 3.1)

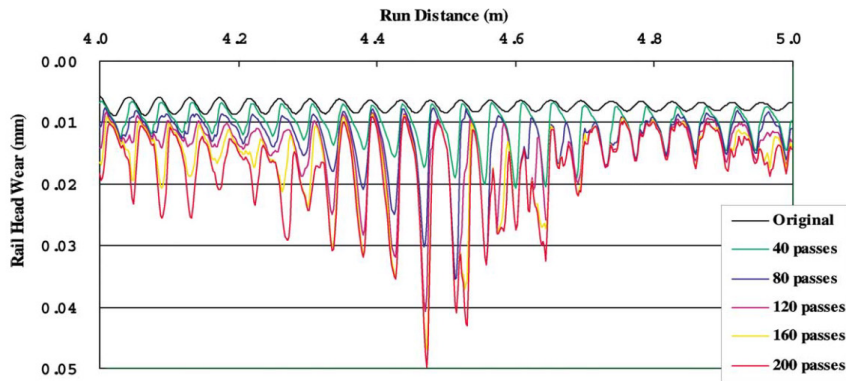


Figure 5.2 Wear growing process of rail head [71]

Usual space-time discretization for this rail-wheel contact problem combine finite element space approximation and time-stepping schemes. In this framework, most methods exhibit spurious oscillations and/or poor behaviour in long time. The common method used to avoid the instability problem is to apply the numerical damping in the FEM model, which usually refers to damping parameters introduced through a numerical algorithm. This numerical damping is also called as "artificial viscosity". In Abaqus/Standard, implicit FEM integrators in the wheel-rail dynamic model is used, and the Hilber-Hughes-Taylor operator is also used as an extension of Newmark-beta methods. Numerical parameters associated with the Hilber-Hughes-Taylor operator are tuned differently for moderate dissipation and transient fidelity applications[72], given as followed:

$$\beta = 1/4 * (1 - \alpha)^2;$$

$$\gamma = 1/2 - \alpha;$$

This relation provides control of the numerical damping associated with the time integrator while preserving desirable characteristics of the integrator. The numerical damping grows with the ratio of the time increment to the period of vibration of a mode. Negative values of α provide damping; whereas $\alpha=0$ results in no damping (energy preserving) and is exactly the trapezoidal rule

(sometimes called the Newmark beta-method, with $\beta=1/4$ and $\gamma=1/2$). Allowable values of α , β , and γ are: $-1/2 \leq \alpha \leq 0$, $\beta > 0$, $\gamma \geq 1/2$.

The modified mass method proposed in [73], [74] and [75] is a space semi-discrete formulation overcoming these two difficulties: the mass term is modified (the mass associated with the normal d.o.f. at the contact boundary is set to zero), then inertial forces can not trigger spurious oscillations, and guarantee the well-posedness of the semi-discrete elasto-dynamics contact problem with Coulomb friction. As a consequence, the previous dynamic finite element model of wheel-rail contact in 2D will be adapted to take into account modified mass method to increase its accuracy and solve the energy dissipation problem. The following work will present an improvement to reproduce more realistically both birth and evolution of straight-track corrugation under transient conditions by taking into account both an improved method to solve rail-wheel contact problem in finite element modelling, and multiple wheel passings.

5.2 Introduction of Mass Redistribution Method

According to the literature [55][58][66][67], there are many works which try to constitute a more stable, less spurious oscillating numerical schemes. However, these works are usually concerned about a solution in time discretization scheme, and many proposed strategies exhibit the drawbacks such as neglected kinetic energy at the contacting nodes, spurious oscillations introduced on the contact boundary or a small interpenetration. To overcome these drawbacks, the works according to Carpenter et al. [64], Ligursky and Renard [75], Renard [76] have studied the numerical instabilities caused by spatial semi-discretization for linear elasto-dynamics frictionless contact problems in the small deformations framework. It was shown that the main cause of ill-posedness is due to the inertia of the nodes on the contact boundary. Then a method which consists in the redistribution of the mass near the contact

boundary is proposed in order to recover the well-posedness of the semi-discrete problem and ensures the solution to be energy-conserving. Moreover, the semi-discrete problem in space reduces to a differential inclusion with a unique Lipschitz continuous solution (not to measure differential inclusion as in the standard semi-discretization), and this solution can be easily approximated by a numerical time scheme. Finally the redistributed mass matrix conserves the total mass, the centre of gravity and the inertia momenta is built so that there is no inertia for the contact nodes. Furthermore, the MRM eliminates spurious oscillations on the contact boundary and respects the non-penetration constraint.

The method proposed in the following part is to apply on the rail/wheel model the redistribution mass method introduced in [75]. The mass matrix terms are set to zero only on the node corresponding to the unilateral contact condition (normal component), but not on the friction one (tangential component). Indeed the well-posedness of the fully discrete problem fails when the mass redistribution method is applied both to unilateral contact and to friction conditions.

Now we describe the strategy to construct the new mass matrix. Let $N := \text{span}\{v_1, \dots, v_{nc}\}$ and N^\perp denote the space spanned by v_i (normal contact boundary on elements in wheel edge) and its orthogonal complement, respectively. We shall consider the redistributed mass matrix $M_r \in M_{np}(\mathbb{R})$ satisfying:

- (i) $M_r = M_r^T$;
- (ii) $\text{Ker}(M_r) = N$;
- (iii) $w^T M_r w > 0 \quad \forall w \in N^\perp, w \neq 0$;

i.e. being symmetric, positive semi-definite with the kernel equal to N . In [73] a simple algorithm is proposed to build the redistributed mass matrix preserving the main characteristics of the mass matrix (total mass, centre of gravity and moments of inertia).

In the following part we are going to apply the mass redistribution method in 2D wheel-rail contact model to solve the energy dissipation problem and reproduce a more realistic corrugation raising process.

5.3 Mass Redistribution Method (MRM) applied to 2D wheel-rail contact model

5.3.1 Convergence tendency of the model with MRM

At first, convergence tendency of the model with MRM is studied with different time increments and different mesh sizes. Table 5.1 shows that the model is convergent within very little time increments ($1e-7s$) in MRM compared with original model (OM), which means that the model using MRM costs more CPU time for the simulation to be completed. The case with Δt_{auto} ($\Delta t_{\text{min}}=1e-7s$, $\Delta t_{\text{max}}=1e-5s$) means that time incrementation is automatically adjusted by Abaqus Standard from an initial incremented time. The size of subsequent time increment adjusted is based on how quickly the solution converges.

	$\Delta t_1(1e-5 \text{ s})$		$\Delta t_2(1e-6 \text{ s})$		$\Delta t_3(1e-7 \text{ s})$		Δt_{auto}	
	OM	MRM	OM	MRM	OM	MRM	OM	MRM
Mesh0.1-0.1(mm)	×	×	√	×	√	√	√	√
Mesh0.2-0.2(mm)	√	×	√	×	√	√	√	√
Mesh0.4-0.4(mm)	√	×	√	×	√	√	√	√

× Calculation aborted

√ Calculation completed

Table 5.1 Different time increments influence on the model convergence tendency

According to the results computed with different mesh sizes (Table 5.2), values such as contact shear force (CSF), normal force (CNF), P_f^G , contact pressure (CPRESS), or plastic deformation (ε^P) have great differences between the three sizes of mesh in the original model. On the contrary, results obtained with MRM are not much influenced. Therefore, MRM helps the model to converge quickly according to mesh size. As a consequence, the results presented afterward will use a mesh size of 0.1 mm length and automatic time incrementation to optimize both computation time and accuracy of the obtained results.

		CSF	CNF	V_{slid}	P_f^G	CPRESS	ε^P
OM	Mesh0.2- mesh0.1	+	+	++	++	++	++
	Mesh0.4- Mesh0.1	+	+	++	++	+++	+++
MRM	Mesh0.2- mesh0.1	0	0	0	0	++	++
	Mesh0.4- Mesh0.1	0	0	+	+	+++	+++

0 Relative value inferior to 1%

+ Relative value inferior to 10%

++ Relative value inferior to 20%

+++ Relative value inferior to 50%


 Mesh size impact

Table 5.2 Comparison of the results in different mesh sizes

5.3.2 Local results obtained with both OM and MRM

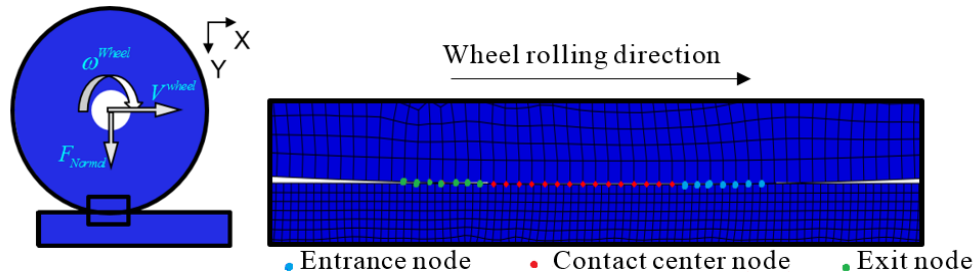


Figure 5.3 Nodes at the wheel-rail contact

First, with the original model, the local frictional power in the contact is calculated (Fig. 5.4). Results show that the nodes both at the entrance and at the exit of the contact have very small frictional power; values vary in a range of 400 – 600W with a fixed frequency of 527 Hz (Fig. 5.4(a), 5.4(c)). On the opposite, the node at the centre of the contact is affected by a higher value of frictional power which amplitude reaches about 1100 W (Fig. 5.4(b)) but with a tendency of decay within the 0.01 seconde of simulation. More precisely, the amplitude decreases from 1100 W to 900 W (Fig. 5.4(b)). These 3 sub-figures (Fig. 5.4) show the frictional power is mainly localized at the centre of the contact; the energy dissipated by the nodes at the centre of the contact is higher than elsewhere of the contact.

Secondly, with the mass redistribution method, the value of frictional power both at the entrance and at the exit of the contact does not much change (Fig. 5.4(a), 5.4(c)). Whereas there are not much influence on the entry node and exit node, frictional power at the centre node has been evidently influenced. The decay of the amplitude seems to be minimized, and the peak value of each period is kept at about 1100 W - 1050 W (1100W – 900W in original model) .

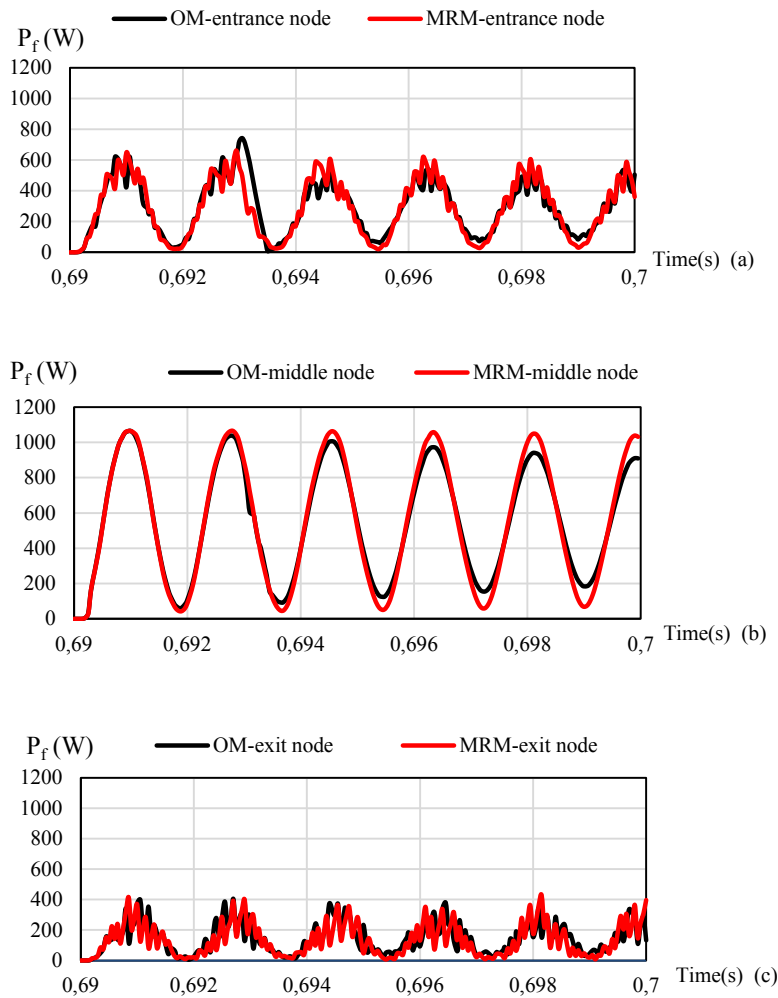


Figure 5.4 Comparison of the local frictional power between the original model (OM) and the mass redistribution model (MRM) at a) entrance node, b) centre node and c) exit node of the contact

5.3.3 Global results obtained with both OM and MRM

Global frictional power computed with both OM and MRM (Fig. 5.5) shows that MRM is less dissipative than the OM, which is what was expected. Abaqus doesn't need to use extra and artificial numerical damping to help the model to converge. The energy injected in the model through the transient conditions is thus better conserved with the MRM applied than with OM. The local contact conditions and consequences will be more realistic. Indeed, the

equivalent plastic deformation reproduced on the rail surface (Fig. 5.6) is much more constant along time with MRM. The plastic deformation goes from 0.15% to 0.13% over the 150mm length of simulated rail with the original model, whereas this value is much more constant with the MRM which better coincide with straight-track corrugation reality.

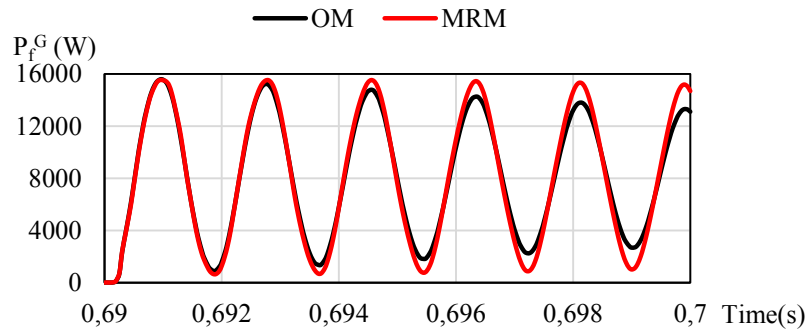


Figure 5.5 Comparison of the global frictional power between the original model (OM) and the mass redistribution model (MRM)

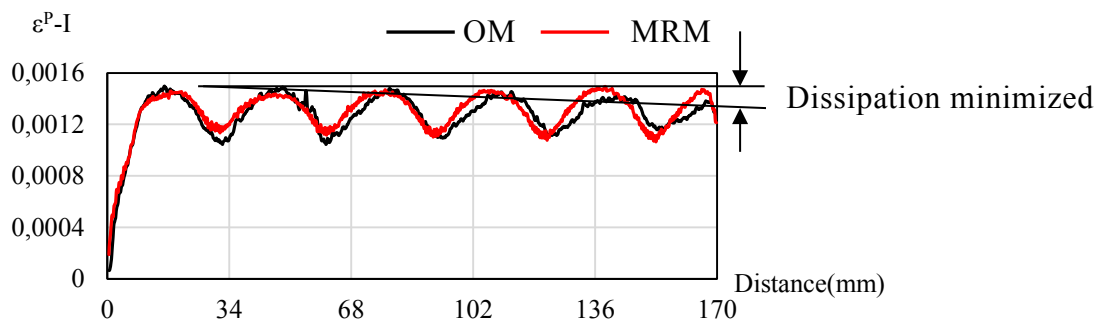


Figure 5.6 Comparison of the plastic deformation on the rail surface between the original model (OM) and the mass redistribution model (MRM)

As the MRM is successfully applied in the 2D wheel-rail dynamic model, the problem of energy dissipation is solved and the corrugation defect is represented in a wheel passing under slip. The defect reproduced in multiple wheel passings is expected with MRM.

5.4 Additional wheel passings with slip in Mass redistribution model

The results of the previous part (Chapter 5.3) show the birth of the periodical defect on the rail surface with OM for single wheel passing with MRM. The use of both MRM and multiple wheel passings will be really helpful to reproduce realistically both the birth and the evolution of corrugation defect. As a consequence, the previous 2D finite element model with MRM was extended to allow two additional wheel passings. Each additional passing uses the same simulation protocol (see Fig. 2.5) such as presented in Section 2.2. Before transient conditions are applied, the wheel-rail contact is in rolling state without sliding conditions and undergoes constant loading. Then, the transient conditions are applied to reach rolling state with sliding conditions in the contact with the same time for each wheel. Simulation parameters are described as in Tables 2.1 and 2.2. The same elasto-plastic law is used for the rail material: $\sigma_{ep}=455+250\varepsilon^P$.

With the same simulation protocol, the multiple wheel passings under slip instability state are reproduced with MRM. Both global tangential contact force and frictional power are investigated. The amplitude of the global tangential contact force F_{tang}^G (see Fig. 5.7(b)) in slip oscillatory state does not change much compared with the results obtained in original model (see Fig. 5.7(a)). On the contrary, unlike the decreased amplitude and dissipative energy in original model (see Fig. 5.7(c)), the peak value of P_f^G (see Fig. 5.7(d)) is kept constant in the value of 16000W in MRM and the energy is not lost in the first three wheel passings.

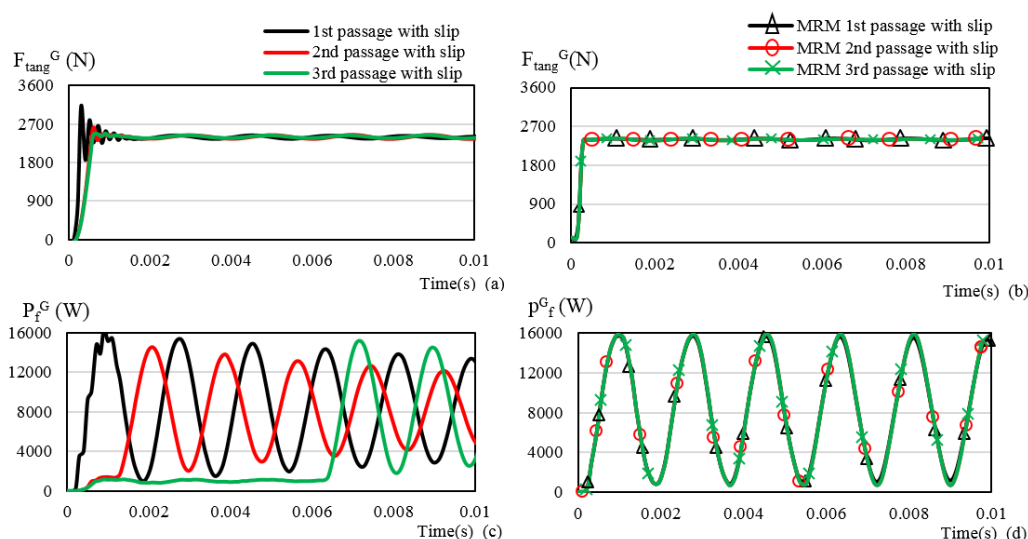


Figure 5.7 Evolution of global tangential contact force F_{tang}^G in (a) OM (b) MRM; and global frictional power P_f^G in (c) OM (d) MRM

The amplitude of the plastic deformation on the rail surface (see Fig. 5.8(b)) and inside the rail (see Fig. 5.8 (d)) shows no major change in the three wheel passings compared with the results obtained in original model. The value of the plastic deformation ε^P -I varies in the same range from 0.10% to 0.15% in the rail surface, and the peak value of plastic deformation on each wavelength is kept as 0.15% and does not decay after three passings. Inside the rail, the amplitude of ε^P -II (see Fig. 5.8(d)) is higher than in previous passings in slip oscillatory state. These curves coincide with the results obtained in original model. Therefore, the model with MRM reproduces more realistic corrugation defects.

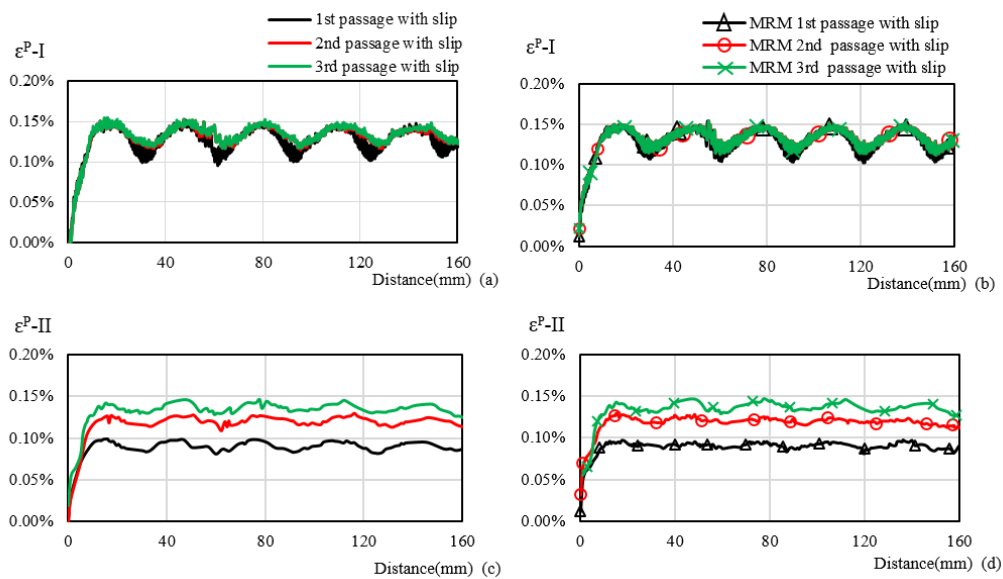


Figure 5.8 Equivalent plastic deformation on rail surface in (a) OM (b) MRM; and interior rail in (c) OM (d) MRM

5.5 Conclusion

Both the origin and the generation of the corrugation defect are represented in MRM in the 2D wheel-rail contact dynamic model. The numerical dissipation problem was solved by Mass Redistribution Method (MRM) and a more realistic corrugation defect is reproduced. The 2D dynamic wheel-rail contact model using MRM superposes each wheel passing in the same phase which explains a better development of corrugation defect than the one obtained with the previous model (OM). But the huge computational cost with application of MRM is really a drawback, we would like to find a proper model to apply MRM; otherwise, it would be difficult to develop the wheel-rail contact dynamic model in 3D.

Conclusion and future work

Since the rail corrugation problem is getting severe, grinding or planning merely alleviates the symptoms. To better understand the corrugation defect, the corrugation characteristics, the formation mechanism, the morphology and the consequence of these phenomena are studied according to the bibliographies. And the complex stick-slip phenomenon exciting tangential vibration may be the root of short-wave corrugations on straight track.

From an experimental point of view, it is difficult to identify the various factors affecting such rail defects, and to quantify the influence of each factor on the birth and development of straight-track corrugation. As a consequence, tribological investigations on real rails affected by such defects have to be completed with numerical modelling. So the numerical modelling research is necessary to better understand the corrugation defect.

At first, an appropriate tool was found to constitute the dynamic wheel-rail contact model. The implicit dynamic finite element code Abaqus Standard was chosen to investigate the dynamic local contact problem. The standard μ -Coulomb's friction law is applied at the contact, and the inequalities of dynamic contact problem are solved thanks to Lagrange multipliers. The rail model is described using a law of linear elasto-plastic with isotropic linear hardening properties, and the wheel is regarded as elastic behaviour. The influence of the elements size and of the different integration times were found out to get the model valid.

Afterwards, the influences of different physical parameters on the birth of corrugation defects are studied. Results obtained in the finite element model highlight the origin of instability states occurring linked to wheel-rail contact under transient conditions. And the wavelength is related to the wheel frequency behaviour. Physical parameters such as slip ratio, friction coefficient, transient conditions applying time, etc... do have an influence on both slip state and slip-stick state. Plastic deformation, which is linked to the corrugation defect, is mainly influenced by material property. And considering the function of the

stiffness of spring and damper between car body and wheel cannot be neglected in the birth of corrugation defect the parameters under transient conditions have a strong influence on the sensibilities of the corrugation defect.

Then, based on the valid 2D dynamic finite element model, the evolution of the corrugation defect is represented under multiple wheel passings. From a qualitative point of view, these results with multiple wheel passings coincide with on-site observation of real corrugation defect on rail surface. Indeed, such defect grows with both the number of wheel passings and the repeatability of contact conditions. Rails affected by straight-track corrugation are mostly urban networks, which are characterized by a great homogeneity of train types, traffic conditions (stops, crossings, etc.) that really imply reproducible global contact conditions for each train.

With the simulation of wheel-rail contact dynamics, the tribological consequence of the corrugation was evaluated. Both the origin and the generation of the corrugation defect are represented. Corrugation grows while the contact behaviour is in slipping. The results obtained in the slip phase show a very important problem of quick energy dissipation, which doesn't coincide with the straight-track corrugation reality. In this framework, most methods exhibit spurious oscillations and/or poor behaviour in long time. The numerical dissipation problem was solved by Mass Redistribution Method (MRM) and a more realistic corrugation defect is reproduced. The 2D dynamic wheel-rail contact model using MRM superposes each wheel passing in the same phase, which explains a better development of corrugation defect than the one obtained with the previous model (OM).

Furthermore, to continue to improve both birth, evolution and prediction of wheel-rail contact, the future work has to switch to the 3D model which will details the corrugation defect more realistically (see Fig.6.1), and wheel-rail contact dynamics in both lateral and longitudinal directions.

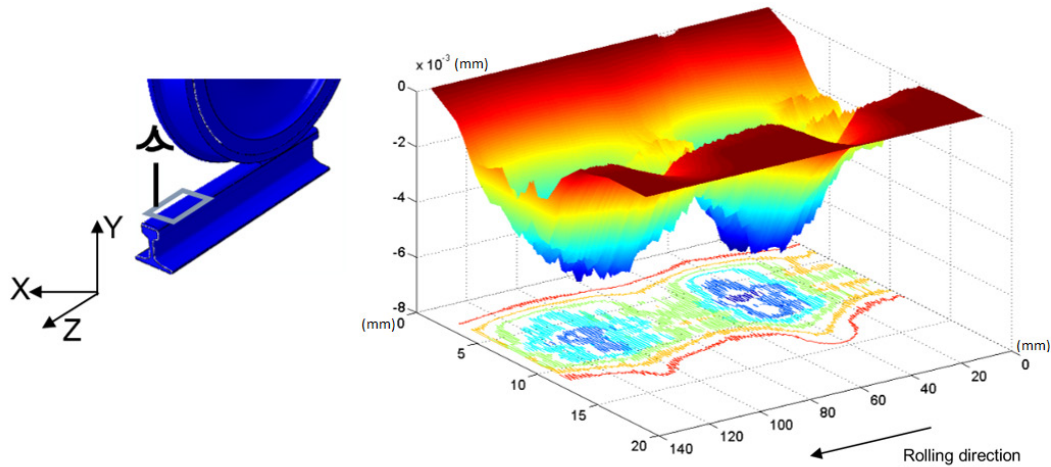


Figure 6.1 Corrugation geometry produced in 3D model

Mesh	Elements size at the contact area(mm)	Relative CPU time
2D	0.1*0.1	1.0
3D	0.1*0.1*0.1	4.5

Table 6.1 Comparison of CPU time in 2D and 3D models

Considering that the current model needs a large computational time to complete the simulation (Table 6.1), a Coupled Eulerian-Lagrangian (CEL) method would be employed in the wheel-rail contact model to make the calculation more efficient. In this case, the wheel is described as an Eulerian body and the rail is kept in Lagrangian behaviour to realize the optimization of both computational cost and accuracy results. Meanwhile, the discrete element model (DEM) is also considered to represent the corrugation wear.

References

-
- [1] K. H. Oostermeijer, “Review on short pitch rail corrugation studies,” *Wear*, vol. 265, no. 9–10, pp. 1231–1237, Oct. 2008.
- [2] K. L. Johnson and G. G. Gray, “Development of corrugations on surfaces in rolling contact,” *Arch. Proc. Inst. Mech. Eng. 1847-1982 (vols 1-196)*, vol. 189, no. 1975, pp. 567–580, Jun. 1975.
- [3] S. L. Grassie and J. Kalousek, “Rail corrugation: Characteristics, Causes and Treatments,” in *Proceedings of the Institution of Mechanical Engineers, Part F: Journal of Rail and Rapid Transit*, 1993, pp. 57–68.
- [4] E. Wild, L. Wang, B. Hasse, T. Wroblewski, G. Goerigk, and a Pyzalla, “Microstructure alterations at the surface of a heavily corrugated rail with strong ripple formation,” *Wear*, vol. 254, no. 9, pp. 876–883, May 2003.
- [5] A. Saulot, S. Descartes, and Y. Berthier, “Sharp curved track corrugation: From corrugation observed on-site, to corrugation reproduced on simulators,” *Tribol. Int.*, vol. 42, no. 11–12, pp. 1691–1705, Dec. 2009.
- [6] W. Cai, Z. Wen, X. Jin, and W. Zhai, “Dynamic stress analysis of rail joint with height difference defect using finite element method,” *Eng. Fail. Anal.*, vol. 14, no. 8, pp. 1488–1499, Dec. 2007.
- [7] Z. Li, R. Dollevoet, M. Molodova, and X. Zhao, “Squat growth—Some observations and the validation of numerical predictions,” *Wear*, vol. 271, no. 1–2, pp. 148–157, May 2011.
- [8] F. Armero and E. Petócz, “Formulation and analysis of conserving algorithms for frictionless dynamic contact/impact problems,” *Comput. Methods Appl. Mech. Eng.*, vol. 158, no. 3–4, pp. 269–300, Jun. 1998.

- [9] N. J. Carpenter, R. L. Taylor, and M. G. Katona, “Lagrange constraints for transient finite element surface contact,” *Int. J. Numer. Methods Eng.*, vol. 32, no. 1, pp. 103–128, Jul. 1991.
- [10] I. Gómez and E. G. Vadillo, “A linear model to explain short pitch corrugation on rails,” *Wear*, vol. 255, no. 7–12, pp. 1127–1142, Aug. 2003.
- [11] P. Hauret and P. Le Tallec, “Energy-controlling time integration methods for nonlinear elastodynamics and low-velocity impact,” *Comput. Methods Appl. Mech. Eng.*, vol. 195, no. 37–40, pp. 4890–4916, Jul. 2006.
- [12] A. Skyttebol, B. L. Josefson, and J. W. Ringsberg, “Fatigue crack growth in a welded rail under the influence of residual stresses,” *Eng. Fract. Mech.*, vol. 72, no. 2, pp. 271–285, Jan. 2005.
- [13] P. Clayton, “Tribological aspects of wheel-rail contact: a review of recent experimental research,” *Wear*, vol. 191, no. 1–2, pp. 170–183, Jan. 1996.
- [14] X. Jin, Z. Wen, K. Wang, and W. Zhang, “Effect of a scratch on curved rail on initiation and evolution of rail corrugation,” *Tribol. Int.*, vol. 37, no. 5, pp. 385–394, May 2004.
- [15] A. Saulot, “Analyse tribologique du contact roue-rail Modélisation et expérimentations,” *these*, 2005.
- [16] J. J. Kalker and F. Périard, “Wheel-rail noise: impact, random, corrugation and tonal noise,” *Wear*, vol. 191, no. 1–2, pp. 184–187, Jan. 1996.
- [17] T. Mazilu, “Green’s functions for analysis of dynamic response of wheel/rail to vertical excitation,” *J. Sound Vib.*, vol. 306, no. 1–2, pp. 31–58, Sep. 2007.

-
- [18] A. Ekberg and E. Kabo, “Fatigue of railway wheels and rails under rolling contact and thermal loading—an overview,” *Wear*, vol. 258, no. 7–8, pp. 1288–1300, Mar. 2005.
- [19] D. F. Cannon and H. Pradier, “Rail rolling contact fatigue Research by the European Rail Research Institute,” *Wear*, vol. 191, no. 1–2, pp. 1–13, Jan. 1996.
- [20] H. Zhang, W. Liu, W. Liu, and Z. Wu, “Study on the cause and treatment of rail corrugation for Beijing metro,” *Wear*, vol. 317, no. 1–2, pp. 120–128, Sep. 2014.
- [21] G. Sheppard, “History of the Broad Gauge,” *The Broad Gauge Society (BGS)*. .
- [22] Y. Sato, A. Matsumoto, and K. Knothe, “Review on rail corrugation studies,” vol. 253, pp. 130–139, 2002.
- [23] c. o. frederick and W.g.bugden, “Corrugation research on british rail.pdf,” *the symposium on rail corrugation problems 1983*, pp. P7–P34, 1983.
- [24] J. J. Kalker, *Three-Dimensional Elastic Bodies in Rolling Contact*. Springer, 1990, p. 314.
- [25] A. R. Valdivia, “A linear dynamic wear model to explain the initiating mechanism of corrugation,” *Veh. Syst. Dyn.*, vol. 17, no. sup1, pp. 493–496, Jan. 1988.
- [26] K. Hempelmann, F. Hiss, K. Knothe, and B. Ripke, “The formation of wear patterns on rail tread,” *Wear*, vol. 144, no. 1–2, pp. 179–195, Apr. 1991.

- [27] K. Hempelmann and K. Knothe, “An extended linear model for the prediction of short pitch corrugation,” *Wear*, vol. 191, no. 1–2, pp. 161–169, Jan. 1996.
- [28] K. KNOTHE and S. L. GRASSIE, “Workshop on rail corrugations and out-of-round wheels,” *J. Sound Vib.*, vol. 227, no. 5, pp. 895–897, Nov. 1999.
- [29] S. MULLER, “A linear wheel-track model to predict instability and short pitch corrugation,” *J. Sound Vib.*, vol. 227, no. 5, pp. 899–913, Nov. 1999.
- [30] M. Steenbergen and R. Dollevoet, “On the mechanism of squat formation on train rails – Part II: Growth,” *Int. J. Fatigue*, vol. 47, pp. 373–381, Feb. 2013.
- [31] X. Jin, X. Xiao, Z. Wen, J. Guo, and M. Zhu, “An investigation into the effect of train curving on wear and contact stresses of wheel and rail,” *Tribol. Int.*, vol. 42, no. 3, pp. 475–490, Mar. 2009.
- [32] S. L. Grassie, R. W. Gregory, D. Harrison, and K. L. Johnson, “The dynamic response of railway track to high frequency vertical excitation,” *Arch. J. Mech. Eng. Sci. 1959-1982 (vols 1-23)*, vol. 24, no. 2, pp. 77–90, Jun. 1982.
- [33] M. C. Luciano Afferrante, “Corrugation models and the roaring rails enigma: a simple analytical contact mechanics model based on a perturbation of Carter’s solution,” *Journal of Mechanics of Materials and Structures*, 2009. .
- [34] S. L. Grassie, “Rail corrugation: advances in measurement, understanding and treatment,” *Wear*, vol. 258, no. 7–8, pp. 1224–1234, Mar. 2005.
- [35] C. Collette, “Torsional vibration absorber for the mitigation of rail corrugation,” 2007. .

-
- [36] A. Saulot, S. Descartes, and Y. Berthier, “Sharp curved track corrugation: From corrugation observed on-site, to corrugation reproduced on simulators,” *Tribol. Int.*, vol. 42, no. 11–12, pp. 1691–1705, Dec. 2009.
- [37] S. L. Grassie, “Short wavelength rail corrugation: field trials and measuring technology,” *Wear*, vol. 191, no. 1–2, pp. 149–160, Jan. 1996.
- [38] A. Eleöd, Y. Berthier, E. Lach, T. Törköly, and G. Juhász, “Friction-induced structural modifications of Mg and Ti surfaces,” *Tribol. Int.*, vol. 42, no. 5, pp. 690–698, May 2009.
- [39] M. Ertz and K. Knothe, “A comparison of analytical and numerical methods for the calculation of temperatures in wheel / rail contact,” vol. 253, pp. 498–508, 2002.
- [40] S. Simon, A. Saulot, C. Dayot, X. Quost, and Y. Berthier, “Tribological characterization of rail squat defects,” *Wear*, vol. 297, no. 1–2, pp. 926–942, Jan. 2013.
- [41] S. Simon, “De la dynamic ferroviaire a l’accommodation microstructurale du rail-contribution des TTS à la réponse tribologique des aciers- Cas du défaut de squat-,” *These Insa.*, 2014.
- [42] K. L. Johnson, *Contact Mechanics*. 1987, p. 452.
- [43] B. J. Hamrock and D. Brewe, “Simplified Solution for Stresses and Deformations,” *J. Lubr. Technol.*, vol. 105, no. 2, p. 171, Apr. 1983.
- [44] D. E. Brewe and B. J. Hamrock, “Simplified Solution for Elliptical-Contact Deformation Between Two Elastic Solids,” *J. Lubr. Technol.*, vol. 99, no. 4, p. 485, Oct. 1977.

- [45] G. Green, *An Essay on the Application of Mathematical Analysis to the Theories of Electricity and Magnetism (Livre numérique Google)*. 1828, p. 72.
- [46] M. Godet, “The third-body approach: A mechanical view of wear,” *Wear*, vol. 100, no. 1–3, pp. 437–452, Dec. 1984.
- [47] Y. Berthier, “Experimental evidence for friction and wear modelling,” *Wear*, vol. 139, no. 1, pp. 77–92, Jul. 1990.
- [48] U. Olofsson, Y. Zhu, S. Abbasi, R. Lewis, and S. Lewis, “Tribology of the wheel–rail contact – aspects of wear, particle emission and adhesion,” *Veh. Syst. Dyn.*, vol. 51, no. 7, pp. 1091–1120, Jul. 2013.
- [49] D. I. Fletcher and S. Lewis, “Creep curve measurement to support wear and adhesion modelling, using a continuously variable creep twin disc machine,” *Wear*, vol. 298–299, pp. 57–65, Feb. 2013.
- [50] O. Polach, “Creep forces in simulations of traction vehicles running on adhesion limit,” *Wear*, vol. 258, no. 7–8, pp. 992–1000, Mar. 2005.
- [51] R. A. CLARK and P. FOSTER, “On the Mechanics of Rail Corrugation Formation,” Jul. 2007.
- [52] Y. SUDA and M. IGUCHI, “BASIC STUDY OF CORRUGATION MECHANISM ON ROLLING CONTACT IN ORDER TO CONTROL RAIL SURFACES,” in *IAVSD SYMPOSIUM (11TH : 1989 : KINGSTON, ONT) THE*, 1989.
- [53] E. Tassilly and N. Vincent, “A linear model for the corrugation of rails,” *J. Sound Vib.*, vol. 150, no. 1, pp. 25–45, Oct. 1991.

-
- [54] G. CERVONI and N. VINCENT, “ACTION AGAINST UNDULATORY RAIL WEAR -- PROPOSAL FOR AN OVERALL APPROACH INVOLVING BOTH TRACK AND ROLLING STOCK,” *Rev. Gen. DES CHEMINS FER*, vol. 105.
- [55] B. R. and B. C., “Dynamic Analysis of Rolling Contact Problem by the Space-Time Element Method,” *ZAMM - J. Appl. Math. Mech. / Zeitschrift für Angew. Math. und Mech.*, vol. 80, no. S1, pp. 29–32, Mar. 2000.
- [56] A. Böhmer and T. Klimpel, “Plastic deformation of corrugated rails—a numerical approach using material data of rail steel,” *Wear*, vol. 253, no. 1–2, pp. 150–161, Jul. 2002.
- [57] M. Hiensch, J. C. O. Nielsen, and E. Verheijen, “Rail corrugation in The Netherlands—measurements and simulations,” *Wear*, vol. 253, no. 1–2, pp. 140–149, Jul. 2002.
- [58] Z. Li, X. Zhao, C. Esveld, R. Dollevoet, and M. Molodova, “An investigation into the causes of squats—Correlation analysis and numerical modeling,” *Wear*, vol. 265, no. 9–10, pp. 1349–1355, Oct. 2008.
- [59] X. Jin, Z. Wen, W. Zhang, and Z. Shen, “Numerical simulation of rail corrugation on a curved track,” *Comput. Struct.*, vol. 83, no. 25–26, pp. 2052–2065, Sep. 2005.
- [60] C. Andersson and A. Johansson, “Prediction of rail corrugation generated by three-dimensional wheel–rail interaction,” *Wear*, vol. 257, no. 3–4, pp. 423–434, Aug. 2004.
- [61] A. Saulot and L. Baillet, “Dynamic Finite Element Simulations for Understanding Wheel-Rail Contact Oscillatory States Occurring Under Sliding Conditions,” *J. Tribol.*, vol. 128, no. 4, p. 761, 2006.

- [62] Y.-C. Chen and S.-Y. Lee, “Elastic-Plastic Wheel-Rail Thermal Contact on Corrugated Rails During Wheel Braking,” *J. Tribol.*, vol. 131, no. 1, p. 011401, 2009.
- [63] W. Li, G. Xiao, Z. Wen, X. Xiao, and X. Jin, “Plastic deformation of curved rail at rail weld caused by train–track dynamic interaction,” *Wear*, vol. 271, no. 1–2, pp. 311–318, May 2011.
- [64] V.-H. Nhu, “Dialogues numériques entre échelles tribologiques - these.pdf,” *These INSA-LYON*, 2013. .
- [65] “Île-de-France tramway Line 3 - Wikipedia, the free encyclopedia.” .
- [66] P. Papadopoulos and J. M. Solberg, “A Lagrange multiplier method for the finite element solution of frictionless contact problems,” *Math. Comput. Model.*, vol. 28, no. 4–8, pp. 373–384, Aug. 1998.
- [67] A. Curnier and P. Alart, “A generalized Newton method for contact problems with friction,” *J. Mécanique Théorique Appliquée, Spec. issue entitled "Numerical Methods Mech. Contact Involv. Frict.*, pp. 67–82, 1988.
- [68] K. Knothe, R. Wille, and B. W. Zastra, “Advanced Contact Mechanics–Road and Rail,” Aug. 2010.
- [69] “Continuous Welded Rail,” *Gd. Sez Gd. Railw. Eng. Sect.*
- [70] N.-H. Lim, N.-H. Park, and Y.-J. Kang, “Stability of continuous welded rail track,” *Comput. Struct.*, vol. 81, no. 22–23, pp. 2219–2236, Sep. 2003.
- [71] A. Matsumoto, Y. Sato, H. Ono, M. Tanimoto, Y. Oka, and E. Miyauchi, “Formation mechanism and countermeasures of rail corrugation on curved track,” *Wear*, vol. 253, no. 1–2, pp. 178–184, Jul. 2002.

-
- [72] H. M. Hilber, T. J. R. Hughes, and R. L. Taylor, “Improved numerical dissipation for time integration algorithms in structural dynamics,” *Earthq. Eng. Struct. Dyn.*, vol. 5, no. 3, pp. 283–292, Jul. 1977.
- [73] H. B. Khenous, P. Laborde, and Y. Renard, “Mass redistribution method for finite element contact problems in elastodynamics,” *Eur. J. Mech. - A/Solids*, vol. 27, no. 5, pp. 918–932, Sep. 2008.
- [74] D. Doyen and a. Ern, “Convergence of a space semi-discrete modified mass method for the dynamic Signorini problem,” *Commun. Math. Sci.*, vol. 7, no. 4, pp. 1063–1072, 2009.
- [75] T. Ligursky and Y. Renard, “A Well-Posed Semi-Discretization of Elastodynamic Contact Problems with Friction,” *Q. J. Mech. Appl. Math.*, vol. 64, no. 2, pp. 215–238, Apr. 2011.
- [76] Y. Renard, “The singular dynamic method for constrained second order hyperbolic equations: Application to dynamic contact problems,” *J. Comput. Appl. Math.*, vol. 234, no. 3, pp. 906–923, Jun. 2010.

Appendix

Elasto-plastic rolling frictionnal contact

1 Mechanical model

1.1 Rolling frictionnal contact

Let $\Omega \subset \mathbb{R}^2$ be a bounded open cylinder with smooth boundary $\Gamma := \partial\Omega$. Ω represents the reference configuration of an elastic wheel of mass density ρ . The coordinate system is chosen such that the center of gravity of the wheel has zero coordinates (i.e., $\int_{\Omega} \rho d\Omega = 0$). Moreover, we first consider the rail as a fixed obstacle occupying the domain Ω_2 with piecewise smooth boundary $\Gamma_2 := \partial\Omega_2$. The boundary of the wheel Ω is divided into two disjoint open sets, as $\Gamma = \Gamma_N \cup \Gamma_C$. Neumann conditions are prescribed on Γ_N . The set Γ_C is the boundary region of the body where contact with the obstacle can occur. Let $\phi : \Omega \times [0, T] \rightarrow \mathbb{R}^2$ be the deformation mapping and $\mathbf{d} := \phi - x$ be the corresponding field of displacements. The deformation gradient is denoted by $\mathbf{F} = \nabla\phi$, and the Green-Saint Venant. To express contact conditions, we define the normal pressure σ_ν and the tangential force σ_τ by

$$\sigma_\nu = (\boldsymbol{\sigma}\boldsymbol{\nu}) \cdot \boldsymbol{\nu}, \quad \sigma_\tau = (\boldsymbol{\sigma}\boldsymbol{\nu}) - \sigma_\nu \boldsymbol{\nu} \quad (1)$$

respectively, and the normal and tangential displacements by

$$\mathbf{d}_\nu = \mathbf{d} \cdot \boldsymbol{\nu}, \quad \mathbf{d}_\tau = \mathbf{d} - \mathbf{d}_\nu \boldsymbol{\nu} \quad (2)$$

Above, $\boldsymbol{\nu}$ stands for the outer normal vector of the deformed domain $\phi(\Omega)$. In order to formulate the non-penetration condition between the two bodies, we introduce a gap function

$$\gamma_C : \Gamma_C \rightarrow \mathbb{R}, \quad \gamma_C := (\pi_\nu(\phi) - \phi) \cdot \boldsymbol{\nu}, \quad (3)$$

that models the distance between the deformed location of a point belonging to Γ_C and its projection onto Γ_r along the normal $\boldsymbol{\nu}$, where π_ν is the projection onto Γ_r along the normal vector to Ω . Thus contact is formulated by inequalities constraint (complementarity or Karush-Kuhn-Tucker conditions)

$$\gamma_C \geq 0, \quad \sigma_\nu \leq 0, \quad \gamma_C \cdot \sigma_\nu = 0 \quad (4)$$

To model the presence of Coulomb's friction with friction coefficient \mathcal{F} , we impose inequalities constraint on the tangent force

$$|\sigma_\tau| \leq \mathcal{F}|\sigma_\nu|, \quad \dot{\mathbf{d}}_\tau - \beta^2 \sigma_\tau, \quad \dot{\mathbf{d}}_\tau (|\sigma_\tau| - \mathcal{F}|\sigma_\nu|) = 0. \quad (5)$$

Let us now formulate the evolution equations of the rolling contact problem. The body is subjected to volume forces and to boundary tractions g on Γ_N . We denote by $\boldsymbol{\lambda}$ the Lagrange multiplier representing the contact forces $-\sigma_\nu$. \mathcal{V} stands for the space of displacements, and the space \mathcal{M} of Lagrange multipliers (dual space of the trace space \mathcal{V} restricted to Γ_C). The mixed formulation of the problem reads:

$$\left\{ \begin{array}{l} \text{Find } (d, \lambda) \text{ such that for almost every time } t \in [0, T], d(t) \in V, \lambda(t) \in \mathcal{M} \text{ such that} \\ m(\ddot{d}, v) + a(d, v) + b(v, \lambda) = l(v), v \in \mathcal{V}, \\ b_\tau(\dot{d}, \mu - \lambda) \leq \langle \gamma_C, \mu_\nu - \lambda_\nu \rangle, \mu(t) \in \mathcal{M}. \end{array} \right. \quad (6)$$

We have used the following notation for the mass and stress operators

$$m(\ddot{d}, v) := \int_{\Omega} \rho \ddot{d} \cdot v d\Omega, \quad a(d, v) := \int_{\Omega} \left(\frac{\partial W}{\partial E} (E(\mathbf{d})) : (Id + \nabla \mathbf{d})^t \nabla v \right) d\Omega, \quad (7)$$

We have denoted the frictionnal contact operator by

$$b(\mu, v) := b_\nu(\mu, v) + b_\tau(\mu, v) = \int_{\Gamma_C} \mu_\nu \cdot v_\nu d\Gamma + \int_{\Gamma_C} \mu_\tau \cdot v_\tau d\Gamma. \quad (8)$$

And finally the load operator is

$$l(v) := \int_{\Omega} f \cdot v d\Omega + \int_{\Gamma_N} g \cdot v d\Gamma \quad (9)$$

1.2 Corotational formulation

In the case of large rotations with respect to a single axis of a fixed direction δ , the deformation reads

$$\phi(x, t) = T(u) + R_\theta(t)(x + \tilde{u}(x, t)) = +R_\theta(t)(x + u(x, t)) \quad (10)$$

where R_θ is a global rotation of axis δ and angle θ , T is the global translation, and u (resp. \tilde{u}) the field of (resp. small) displacements with respect to the rotated configuration. In order to guarantee the uniqueness of u free from elementary rotation,

Since the large rotation part has been filtered out of \mathbf{d} , the rotated field of displacements \mathbf{u} has small amplitude, up to the addition of a uniform translation. It follows the following approximation:

$$\mathbf{E}(\mathbf{d}) \doteq \varepsilon(\mathbf{u}) \quad (11)$$

It becomes possible rewrite the weak mixed formulation (6) with the new variables large rotation θ , and small local displacement \mathbf{u} . In particular the assumption of small local displacement (i.e. $\mathbf{u} \ll x$) leads to linearisations and simplifications. The velocity is approximate by

$$s(x, t) = \dot{\mathbf{u}}(x, t) + \dot{\theta}(t)\Pi(x + T(\mathbf{u}(x, t))). \quad (12)$$

Then the elastic operator is now express with the linear Saint Venant-Kirchhoff elastic tensor, denotes by \mathbf{C} , and becomes

$$a(u, v) := \int_{\Omega} \boldsymbol{\sigma}(u) : \varepsilon(v) d\Omega = \int_{\Omega} \mathbf{C}\varepsilon(u) : \varepsilon(v) d\Omega \quad (13)$$

$$\left\{ \begin{array}{l} \text{Find } (\mathbf{u}, \boldsymbol{\lambda}, \theta) \text{ such that for almost every time } t \in [0, T], \mathbf{u}(t) \in V, \boldsymbol{\lambda}(t) \in \mathcal{M}, \theta(t) \in \mathbb{R} \text{ such that} \\ m(\mathbf{u}, \Pi x) = 0 \\ m(\dot{s} + \dot{\theta}\Pi s, v) + a(\mathbf{u}, v) + b(v, \boldsymbol{\lambda}) = l_\theta(v), v \in \mathcal{V}, \\ b_{\tau_0}(s, \mu - \boldsymbol{\lambda}) + b_{\nu_0}(\mathbf{u}, \mu - \boldsymbol{\lambda}) \leq \langle \gamma_{C, \theta}, \mu_{\nu_0} - \boldsymbol{\lambda}_{\nu_0} \rangle, \mu(t) \in \mathcal{M}. \end{array} \right. \quad (14)$$

where $l_\theta(v) := l_\theta(R_\theta v)$, and $\gamma_{C, \theta} = (\pi_{\nu_0}^\theta(x) - x) \cdot \nu_0$ with $\pi_{\nu_0}^\theta$ the projection onto $R_\theta(\Omega)$ in direction ν_0 .

1.3 Plastic constitutive law of the rail

We now, consider the rail as an elasto-plastic material, occupying, in its initial state, a domain Ω_r with piecewise smooth boundary $\Gamma_2 := \partial\Omega_2$. The characteristic feature of elastoplastic materials is that they behave as elastic media within a certain stress range, termed the elastic region; if the stress reaches the boundary of this region, plastification takes place. As long as the stress is below a given yield stress $\sigma_y > 0$, the relationship between

strain and stress is linear. But if the strain is increased further, the stress value is bounded from above by σ_y for the case of perfect plasticity or by the value of a so-called yield function if hardening is present. The irreversibility of this process can be seen from the fact that there is some remaining plastic strain after unloading to the stress-free state. From thermodynamic considerations, one can deduce that the total strain ϵ_r as well as the internal energy W_r of the rail can additively be decomposed into an elastic part and a plastic part by

$$\epsilon_2 = \epsilon_2^{el} + \epsilon_2^{pl}, W_2 = W_2^{el} + W_2^{pl}. \quad (15)$$

Using the quadratic function for the elastic energy $W_2^{el} = W_2^{el}(\epsilon_2^{el})$, one obtains that the Cauchy stress depends only on the elastic part of the strain.

The plastic part W_2^{pl} of the energy describes the hardening behaviour of the material. In the following we consider the case of linear kinematic and isotropic hardening, where the inner variables are given by the plastic strain tensor ϵ^{pl} and the equivalent plastic strain α :

$$W_2^{pl} = (\alpha, \epsilon^{pl}) = \frac{1}{8}K\|\epsilon^{pl}\|^2 + \frac{1}{2}H\alpha^2 \quad (16)$$

The two constants K, H for the kinematic and isotropic hardening are assumed to be nonnegative. One can define the inner variable χ conjugate to α by

$$\chi := -\frac{\partial W}{\partial \alpha} = -H\alpha. \quad (17)$$

This quantity is used to describe the plastification process by means of the yield function p which defines the elastic region consisting of those sets of generalized stresses. From the principle of maximum plastic dissipation it follows that the set \mathcal{E}^{pl} is convex as well as that the evolution of the plastic inner variables satisfies an associative flow rule, i.e.,

$$\mathcal{E}^{pl} := \{(\chi, \sigma) \in \mathcal{M}^{pl} / p(\chi, \sigma) \leq 0\} \quad (18)$$

Their derivatives with respect to time are determined by the yield function:

$$\dot{\epsilon}_r^{pl} = \lambda^{pl} \frac{\partial p(\chi, \sigma)}{\partial \sigma} \quad (19)$$

$$\dot{\alpha}_r^{pl} = \lambda^{pl} \frac{\partial p(\chi, \sigma)}{\partial \chi} \quad (20)$$

Above, λ^{pl} is a nonnegative variable called the plastic multiplier which can only be nonzero if the generalized stresses are on the boundary $\partial\mathcal{E}^{pl}$ of the elastic region. This fact leads to the complementarity or Karush-Kuhn-Tucker (KKT) conditions

$$p(\chi, \sigma) \leq 0, \lambda^{pl} \geq 0, \lambda^{pl} \cdot p(\chi, \sigma) = 0. \quad (21)$$

For cases like metal plasticity, one observes that the plastic deformation barely inflicts a change in the volume. In this case, it is assumed that the plastic strain ϵ^{pl} has no volumetric part, i.e.

$$\epsilon^{pl} = Dev(\epsilon^{pl}) := \epsilon^{pl} - \frac{1}{2}(Tr(\epsilon^{pl})Id), \text{ with } Tr(\epsilon^{pl}) = 0. \quad (22)$$

Introducing the relative deviatoric stress

$$\boldsymbol{\sigma}^D = Dev(\boldsymbol{\sigma}) - \frac{1}{4}K(\boldsymbol{\varepsilon}^{pl}), \quad (23)$$

we define the yield function by

$$p(\chi, \sigma) := \|\boldsymbol{\sigma}^D\| - \frac{1}{2}(\sigma_y - \chi) - \frac{1}{2}(\sigma_y + \chi) = \|\boldsymbol{\sigma}^D\| - \frac{1}{2}(\sigma_y + H\alpha) \quad (24)$$

1.4 Complete formulation: frictional rolling wheel on an elasto-plastic rail

The most common approach to treat the contact between two deformable bodies is known as the master/slave formulation. Let us briefly recall what it consists in. Consider two deformable bodies whose reference configurations are two bounded open $\Omega_\ell \subset \mathbb{R}^2$ with smooth boundary, such that $\Omega_1 = \Omega$ and $\Omega_2 = \Omega_r$ and of mass density $\rho_1 = \rho$ and $\rho_2 = \rho_r$. $\Gamma_2 = \partial\Omega_2$ is decomposed into disjoint open sets, as $\Gamma_2 = \Gamma_D \cup \Gamma_F \cup \Gamma_C$. The boundary Γ_D is fixed set of positive measure. On Γ_D , the value of the displacement is fixed to zero, whereas a free loading surface is denoted by Γ_F . The boundary conditions on Γ_C are determined by the possibility of frictional contact with the wheel Ω_1 . We assume that deformations of the rail are small, then we can still use the non-penetration conditions (3) and (4), and the Coulomb's friction inequalities (5). Here, the Green-Saint Venant strain tensor of the rail is replaced by its linearized version

$$\boldsymbol{\varepsilon}_2 = \boldsymbol{\varepsilon}_2(u_2) = \frac{1}{2}(\nabla u_2 + \nabla u_2^t) \quad (25)$$

and the corresponding stress tensor is denoted by the Cauchy stress $\boldsymbol{\sigma}_2 = \mathbf{C}_2 \boldsymbol{\varepsilon}_2^{el}$.

We denote the mass and stress operators associated to the rail by

$$m_2(u, v) := \int_{\Omega_2} \rho_2 \ddot{u} \cdot v d\Omega, \quad a_2(u, v) := \int_{\Omega_2} \boldsymbol{\sigma}_2(u) : \boldsymbol{\varepsilon}^{el}(v) d\Omega, \quad (26)$$

We set the plastic operator

$$b^{pl}(\boldsymbol{\varepsilon}, \boldsymbol{\zeta}) := - \int_{\Omega_2} \mathbf{C}_2 \boldsymbol{\varepsilon} : \boldsymbol{\zeta} d\Omega. \quad (27)$$

$\mathcal{V}_2 := \{\mathbf{v} \in \mathcal{V} / \mathbf{v} = \mathbf{v}_D \text{ on } \Gamma_D\}$ stands for the space of displacements of the rail. For $\mathcal{F} > 0$, the weak formulation has the structure of a quasi-variational inequality:

$$\left\{ \begin{array}{l} \text{Find } (d_1, d_2, \lambda) \text{ such that for almost every time } t \in [0, T], d_\ell \in \mathcal{V}_\ell, \lambda(t) \in \mathcal{M} \text{ such that} \\ \sum_{\ell=1,2} m_\ell(\ddot{d}_\ell, v_\ell) + a_\ell(d_\ell, v_\ell) + b(v, \lambda) + b^{pl}(\dot{d}_2, \boldsymbol{\zeta}) = l(v_2), v_\ell \in \mathcal{V}_\ell, \\ b(\dot{d}, \mu - \lambda) \leq \langle \gamma_C, \mu_\nu - \lambda_\nu \rangle, \mu(t) \in \mathcal{M}, \\ b^{pl}(\mathbf{C}_2^{-1}(\boldsymbol{\zeta} - \boldsymbol{\eta}), \boldsymbol{\varepsilon}^{pl}) \leq \int_{\Omega_2} H \dot{\boldsymbol{\alpha}}(\beta - \boldsymbol{\alpha}), \boldsymbol{\zeta} \in \mathcal{E}^{pl}, \end{array} \right. \quad (28)$$

Remark 1 *The existence of solution of (28) is still considered as an important open problem.*

1.5 Numerical model and discretisation

Referring to the contact problem of wheel-rail, the implicit dynamic finite element code Abaqus Standard is used to reproduce the frictional contact between two bodies: a deformable rotating disc (a wheel) and a deformable body (a rail) with elastic-plastic behavior. The instability states are characterized as the consequence

of the sliding velocity imposed and shear stress at the contact. The contact problem is solved thanks to Lagrange Multiplier method with standard Coulombs friction without regularization of the tangential stress with respect to the tangential velocity component. Sliding conditions are imposed through an increase of the angular velocity ω wheel of the center of the disc while the translating velocity $\dot{T}_1(G)$ of the gravity center remains constant. In order to study the instability in transient conditions, the global stiffness and the train-track system are not considered in this study. And before the sliding step applied, the wheel is rolling in a constant velocity while a constant value of normal load applied in the wheel center, the model is assured that the wheel is in pure rolling state, and the whole system:

$$\gamma_s = \frac{|R\theta\omega - \dot{T}_1(G)|}{\dot{T}_1(G)} \quad (29)$$

Discretizations of solids (wheel and rail) are based on linear quadrilateral elements (of type CPE4R) and on linear triangular elements (of type CPE3 in the need of mesh). Within such a finite element model the master segment is given by a four-node isoparametric surface element which comes into contact with one slave node. We denote h_j the thickness of the j -element, and $h = \max_j h_j$.

In order to highlight oscillatory states occurring in the contact patch, the temporal evolution of the global tangential contact force λ_τ , which is the sum of all the local tangential contact force at each node i in the contact surface S_C approximated by the discret contact surface S_C^h :

$$\lambda_\tau^h = \sum_{i \in S_C^h} \lambda_{\tau,i}^h \quad (30)$$

By definition the global frictional dissipation power is

$$P_f = \int_{S_C} \lambda_\tau \cdot \dot{T}_s dS \quad (31)$$

With $|\dot{T}_s| = \gamma_s |\dot{T}_1|$ being the global relative sliding velocity between the rail and wheel. The local frictional power $P_{f,i}^h$ at each node i of the contact patch is used to approximate P_f . This can also help to determine whether or not the oscillatory state leads to surface degradation :

$$P_{f,i}^h = \lambda_{\tau,i}^h \dot{T}_{s,i}^h = \sigma_{s,i}^h S_{C,i} \dot{T}_{s,i}^h \quad (32)$$

where $\sigma_{s,i}$ is the local shear contact sliding at each node i , $S_{C,i}$ being the elementary surface around each i , and \dot{T}_s is the local relative sliding velocity between the wheel and the rail at each node i in the contact patch. The sum of all $P_{f,i}^h$ at each node i of the contact is equalvalent to the classical global frictional power sliding:

$$P_f^h = \sum_{i \in S_C^h} \lambda_{\tau,i}^h \dot{T}_{s,i}^h = \sum_{i \in S_C^h} P_{f,i}^h \quad (33)$$

Remark 2 *The question of the convergence (when h tends to zero) of the discretization of (28), (30), (32) and (33) is still open.*

2 Approximation and resolution of the frictional elasto-plastic contact problem

In the previous section the equation of motion has been formulated as weak variational inequalities. In order to obtain a numerical solution, (28) is discretized thanks to FEM for the space variable, and an HHT time-integration scheme. In the Abaqus/implicit, equations (28) are solved iteratively under appropriate initial conditions, where the discretized contact model serves as a boundary condition. The nonlinear equations with lagrangian multipliers are solved using a generalised Newton's method.

In the following, we briefly recall some basic facts about HHT time-integration schemes in linear elastodynamics. The Hilber-Hughes-Taylor (HHT) method is widely used in the structural dynamics community for the numerical integration of a linear set of second Ordinary Differential Equations (ODE). This problem is obtained at the end of a finite element discretization. Provided the finite element approach is linear, the equations of motion assume the form

$$M\ddot{u}(t) + C\dot{u}(t) + Ku(t) = F(t).$$

The mass, damping, and stiffness matrices, M , C and K , respectively, are constant, the force F depends on time t , and u is the set of generalized coordinates used to represent the configuration of the system. The HHT method reads :

$$\left\{ \begin{array}{l} \text{Find } u^{n+1}, \dot{u}^{n+1}, \ddot{u}^{n+1} \in \mathbb{R}^N, \text{ such that} \\ M\ddot{u}^{n+1} + (1 - \alpha)(C\dot{u}^{n+1} + Ku^{n+1}) + \alpha(C\dot{u}^n + Ku^n) = (1 - \alpha)F^{n+1} + \alpha F^n, \\ u^{n+1} = u^n + \Delta t \dot{u}^n + \frac{\Delta t^2}{2} [(1 - 2\beta)\ddot{u}^n + 2\beta\ddot{u}^{n+1}], \\ \dot{u}^{n+1} = \dot{u}^n + \Delta t [(1 - \gamma)\ddot{u}^n + \gamma\ddot{u}^{n+1}], \end{array} \right. \quad (34)$$

where α, β, γ are parameters linked by the relation $\gamma = (1 - 2\alpha)/2$ and $\beta = (1 - \alpha)^2/4$. This method is implicit and stable provided $\gamma \geq 1/2$ and $\beta \geq (\gamma + 1/2)^2/4$. We remark that \dot{u}^{n+1} and u^{n+1} are functions of the acceleration term \ddot{u}^{n+1} , which remains the sole unknown quantity that is obtained as the solution of a linear system.

Note that in the limit, the choice $\alpha = 0$ leads to the Newmark method with no numerical damping. The particular choice $\beta = 1/4$, $\gamma = 1/2$ yields an implicit, unconditionally stable, and second-order scheme. It is energy-conserving in the sense that

$$E^{n+1} - E^n = {}^T F^{n+1} (u^{n+1} - u^n).$$

FOLIO ADMINISTRATIFTHÈSE SOUTENUE DEVANT L'INSTITUT NATIONAL
DES SCIENCES APPLIQUÉES DE LYON

NOM : DUAN

DATE de SOUTENANCE : 09 Mars 2015

Prénoms : FANGFANG

TITRE :

NUMERICAL TRIBOLOGY OF THE WHEEL-RAIL CONTACT: APPLICATION TO CORRUGATION DEFECT

NATURE : Doctorat

Numéro d'ordre: 2015ISAL0019

Ecole doctorale : MECANIQUE – ENERGETIQUE – GENIE CIVIL – ACOUSTIQUE(MEGA)

Spécialité: MECANIQUE

RESUME:

For more than a century, rail corrugation has been exposed as one of the most serious problems experienced in railway networks. It also comes with a series of problems for maintenance, such as rolling noises and structural vibrations that can reduce lifetime of both train and track. This periodical phenomenon on rail surface is closely linked to wheel-rail contact dynamic, which depends on friction, train dynamics... To better understand corrugation birth conditions, a numerical model is suggested to complement the experimental limitations and to instrument a wheel-rail contact both locally and dynamically.

At first, an appropriate tool was chosen to create the dynamic wheel-rail contact model to reproduce straight-track corrugation, also called "short-pitch" corrugation. The implicit dynamic finite element code Abaqus was chosen to investigate the dynamic local contact conditions. Both the origin and the evolution of straight-track corrugation under transient conditions (acceleration / deceleration) are studied. The parametrical sensibility of corrugation is thus investigated both with single/multiple wheel passing(s) and with geometric defect. A stick-slip phenomenon, linked to both wheel and rail dynamics coupled through the contact, is identified as the root of straight-track corrugation under transient conditions.

Secondly, results obtained with the previous model have highlighted a quick decrease of corrugation amplitude with the increase of wheel passings over the rail. This last result seems to be in contradiction with reality. This problem comes from the difficulty to reliably manage contact dynamics, and particularly with local impacts, with the use of classical finite element models such as the one implemented in Abaqus. To compensate for this lack, a mass redistribution method is implemented in Abaqus and used with the previous case. The results show a more realistic corrugation growth according to the number of wheel passings.

Keywords: corrugation, wheel-rail contact dynamics, FEM, mass redistribution method.

Laboratoire (s) de recherche : Laboratoire de Mécanique des Contacts et des Structures(LaMCoS), CNRS, UMR5259

Directeurs de thèse: BERTHIER Yves
SAULOT AurélienDirecteur de Recherche CNRS, LaMCoS, INSA, Lyon
Maitre de Conférences HDR, LaMCoS, INSA, Lyon

Président de jury :

Composition du jury: BERTHIER Yves
SAULOT Aurélien
POZZOLINI Cédric
DENAPE Jean
ELEOD Andras
DUFRENOY Philippe
QUOST XavierDirecteur de Recherche CNRS, LaMCoS, INSA, Lyon
Maitre de Conférences HDR, LaMCoS, INSA, Lyon
Dr, Institut Notre Dame des Minimes, Lyon
Professeur, Ecole Nationale d'Ingénieurs, Tarbes
Professeur, Université Technique Budapest, Hongrie
Professeur, Laboratoire de Mécanique de Lille, Lille
Dr, RATP, Paris